The Application of a Piezoelectric MEMS Cantilever Array as a Completely Implantable Cochlear Implant

by

Katherine E. Knisely

A dissertation submitted in partial fulfillment
of the requirements for the degree of
Doctor of Philosophy
(Mechanical Engineering)
in The University of Michigan
2014

Doctoral Committee:

> Professor Karl Grosh, Chair
> Professor David R. Dowling
> Professor R. Keith Duncan
> Professor Mina Rais-Zadeh
> Professor Yehoash Raphael

ACKNOWLEDGEMENTS

has kept me strong, focused, and happy through my years at Michigan. I hope to continue our friendships as we move on to the next phases of our lives. Finally, thank you to Mom, Dad, Emily, and especially Forrest for all your love and support through the years. I am blessed to have such a supportive family and wonderful husband!

TABLE OF CONTENTS

LIST OF FIGURES

LIST OF TABLES

ABSTRACT

The Application of a Piezoelectric MEMS Cantilever Array as a Completely
Implantable Cochlear Implant

by

Katherine E. Knisely

Chair: Karl Grosh

Aluminum nitride (AlN) has emerged as an excellent material for a variety of MEMS
applications because of its high electrical resistance, low dielectric loss, and high sound
velocity. Recently, MEMS sensors using AlN in a bimorph cantilever configuration
have demonstrated low noise floors and good sensitivity. The cantilever configuration
has many benefits, including a more linear response, control of the frequency response
using simple changes to the beam geometry, and simple adaptation from microphone
to hydrophone.

We present an array of AlN bimorph cantilevers that are designed to function as a
completely implantable cochlear implant (CI). The array was fabricated using MEMS
batch fabrication techniques. A silicon backbone supports five 400μm wide, 3μm
thick bimorph (Platinum/aluminum nitride (AlN) stack) cantilevers, each of which is
designed to have a resonance, in water, that corresponds to its tonotopic location in
the guinea pig cochlea (20-40kHz). Parylene and gold cabling extends from the probe
for external monitoring during *in vitro* and *in vivo* studies. The frequency responses
of the cantilevers in a viscous fluid are predicted using a modified Euler-Bernoulli

equation that includes viscous damping, and is measured using a laser vibrometer and a calibrated underwater transducer pair.

Achieving reliable, high quality, stress passivated AlN films for this implant design can be a challenge. A number of factors affect the growth characteristics of AlN, including target power, gas pressure, target life, film thickness, and the substrate material and patterning. We present characterization of the effect of deposition power on the growth of 1.5μm thick AlN films, grown on 565nm of thermal oxide on a silicon substrate. X-ray diffraction analysis of these films show well-ordered, c-axis oriented films with rocking curve full width half maximum values under $1.4\pm0.05°$. High resolution transmission electron microscope (HRTEM) imaging identifies atomic-level characteristics of process induced faults and dislocations that occur at the start of the deposition process and when vacuum is broken between two consecutive AlN depositions.

Unlike traditional CIs, this probe is designed to transduce mechanical vibrations of the cochlear fluid into electrical signals that stimulate the auditory nerves. Vibrations in the cochlear fluid deflect the cantilevers, resulting in a potential forming on the outer electrode layers of the cantilever. The outer electrodes are in electrical contact with the ionic fluid of the cochlea, producing a current in the cochlear fluid that is passed to the auditory nerves. In this design the energy is locally sensed and converted into stimulation within the cochlea, therefore our design does not require the traditional signal processing unit, microphone, and transceiver that current CIs employ. Initial acute *in vivo* testing of an implanted fabricated device produced a $2?\mu$V device response when a 110dB_{SPL} sound source was played at the entrance to the ear canal, demonstrating that this device has the potential to restore hearing when sufficient amplification is used. Benefits of this design include lower power, smaller size, and lower latency when compared with current commercial CIs.

CHAPTER I

Introduction

"I am just as deaf as I am blind. The problems of deafness are deeper and more complex, if not more important than those of blindness. Deafness is a much worse misfortune. For it means the loss of the most vital stimulus - the sound of the voice that brings language, sets thoughts astir, and keeps us in the intellectual company of man." - Helen Keller

In 1961, Georg von Békésy was awarded the Nobel Prize in Physiology or Medicine for his studies of the cochlea. One of his great achievements was the development of a method to observe the *in vivo* envelope response of the basilar membrane (BM) to sinusoid inputs using a drill, a water bath, and silver dust [8, 9]. Remarkably, using this technique he observed one of the most fundamental properties of the cochlea: that incoming sound waves are separated tonotopically along the length of the BM, effectively performing a real-time Fourier transform of the incoming signal. Furthermore, von Békésy postulated that the tonotopic response of the BM correlated with the tonotopic mapping of the auditory neurons in the brain. In his Nobel prize speech, he speaks of this realization: "I well remember the crucial night when I finally became convinced that...the ordinary bending of the basilar membrane furnished an adequate description of the vibrations that stimulate the nerve endings. To appreciate that

night, you have to remember that the whole inner ear of a guinea pig is about as large as a drop of water at the end of an eye dropper" [9].

Thankfully, the field of cochlear studies has advanced significantly since von Békésy's drill and silver dust technique. More sophisticated methods of measuring BM response were developed, such as the Mossbauer technique and laser velocimitry. Using these techniques, precise measurements of BM response were obtained at basal locations of the cochlea, revealing nonlinearities in the *in vivo* BM response that did not arise in dead cochleae. Through a combination of the extremely well tuned cochlea and nonlinear feedback, human beings are able to distinguish an impressive 3000 frequencies of sound, ranging from 20-20kHz, over a pressure range of 120dB_{SPL} [10, 11, 12].

Cochlear implants are a direct result of this knowledge of the inner ear. The cochlear implant consists of an electrode array inserted into the cochlea. Electrical signals, usually frequency filtered, are sent to the electrodes, producing a current in the ionic fluid of the cochlea. This stimulation current mimics the electrical signal that is produced by the sensory cells in the cochlea; the current stimulates the auditory nerve, restoring hearing. Rudimentary single-channeled cochlear implants that were developed in the 1970s [13, 14] have developed into 16+ channel electrode arrays that are backed by powerful signal processing units, allowing for deaf people to regain high level of speech recognition [15]. Cochlear implants were, and continue to be, a remarkable biomedical implant success story.

However, for all the successes that CIs have had, the market penetration of CIs is startlingly low: of the estimated 360 million people who have profound hearing loss or are deaf in the world, only approximately 200,000 people have CIs. This is due in part to the extremely high cost of implantation, which is estimated at 50-100 thousand dollars in the US (of which Medicare only pays 20 thousand dollars) [16]; this is a cost that people in developing countries simply cannot afford. Despite this high cost CIs do not fully restore hearing, and CI usefulness is limited in more complex acoustic

situations like noisy rooms and listening to music [15]. Additionally, full utilization of the device requires implantation at a young age; adults who are implanted without previously being able to hear have difficulties processing the sound from the device [17].

It is clear that in order to achieve higher market penetration future CIs need to have reduced cost, lower power consumption, and easier means of surgical implantation. While research progresses with traditional CIs that use signal processing, there is an inherent limit to the processor power consumption and the efficiency of the transmission of the inductive link separating the processor and the internal receiving unit. For these reasons alternative designs for CIs that bypass these limitations are attractive. In this thesis we present one such CI design that requires neither a sound processing unit nor a transceiver unit. In this design the sound sensing mechanism is located in the cochlea, from which it derives its frequency filtering and power. This design is completely implantable and has low power consumption. By manufacturing this device using MEMS batch processing techniques, we gain precision control of the device's mechanical and electrical properties at a relatively low cost of device fabrication. This thesis aims to demonstrate a device that has the possibility of expanding the existing CI market to those who cannot currently afford the initial costs of a CI, nor the cost of its upkeep.

1.1 Physiology of the Cochlea

1.1.1 Structure of the Ear

The ear is commonly divided into three parts: the outer, middle, and inner ear, as shown in Figure refEarAnata. The outer ear is composed of the pinna (the part of the ear that is outside of the head), the external audiotry meatus (ear canal), and
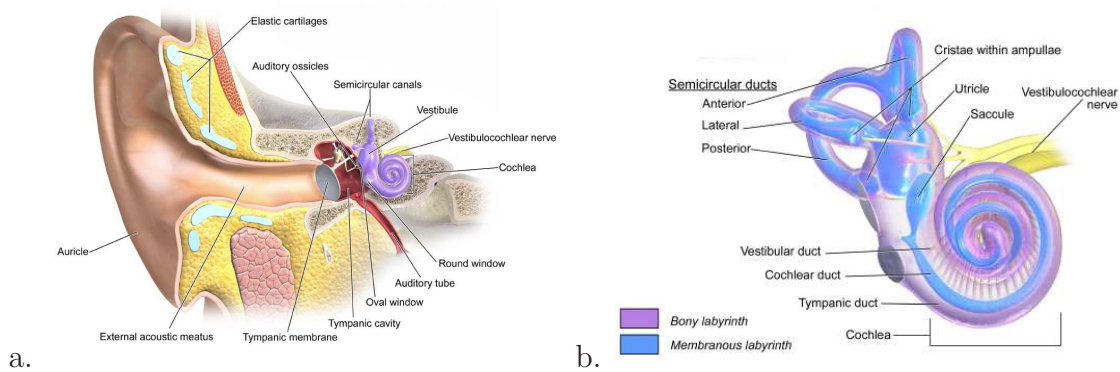
Figure 1.1: (a) The outer, middle (colored red), and inner ear (colored purple) regions of the ear. (b) A cross-sectional view of the bony labyrinth, which houses the vestibular system and the cochlea. [1, 2]

the tympanic membrane (ear drum). These three bones, which are the smallest in the human body, reside in the tympanic cavity of the middle ear, which connects via the eustachian tube to the nasal cavity. In order, they are the malleus (named after a hammer, attached to the ear drum), the incus (meaning "anvil"), and the stapes ("stirrup"). The stapes terminates in a large flat plate, which is attached to the oval window, where it drives the fluid of the labyrinth of the inner ear.

The inner ear is comprised of two parts: the vestibular system, which provides the sense of acceleration and head position in space, and the cochlea, which transduces sound vibrations into neural signals; a diagram of the bony labyrinth that houses the vestibule, semicircular canals, and the cochlea is shown in Figure 1.1b. A brief description of the cochleas function is given in the subsequent section; more detailed descriptions of its function are detailed in References[11, 18, 19].

1.1.2 The Cochlea

The cochlea is named after the latin word for spiral shell *cochlos* for its spiral-helix shape (like that of a snail shell). When unwound, the cochlea consists of three parallel ducts: the scala vestibuli (SV), the scala tympani (ST), and the scala media (SM), which in between the SV and the ST. The ST and SM are separated by the basilar

4
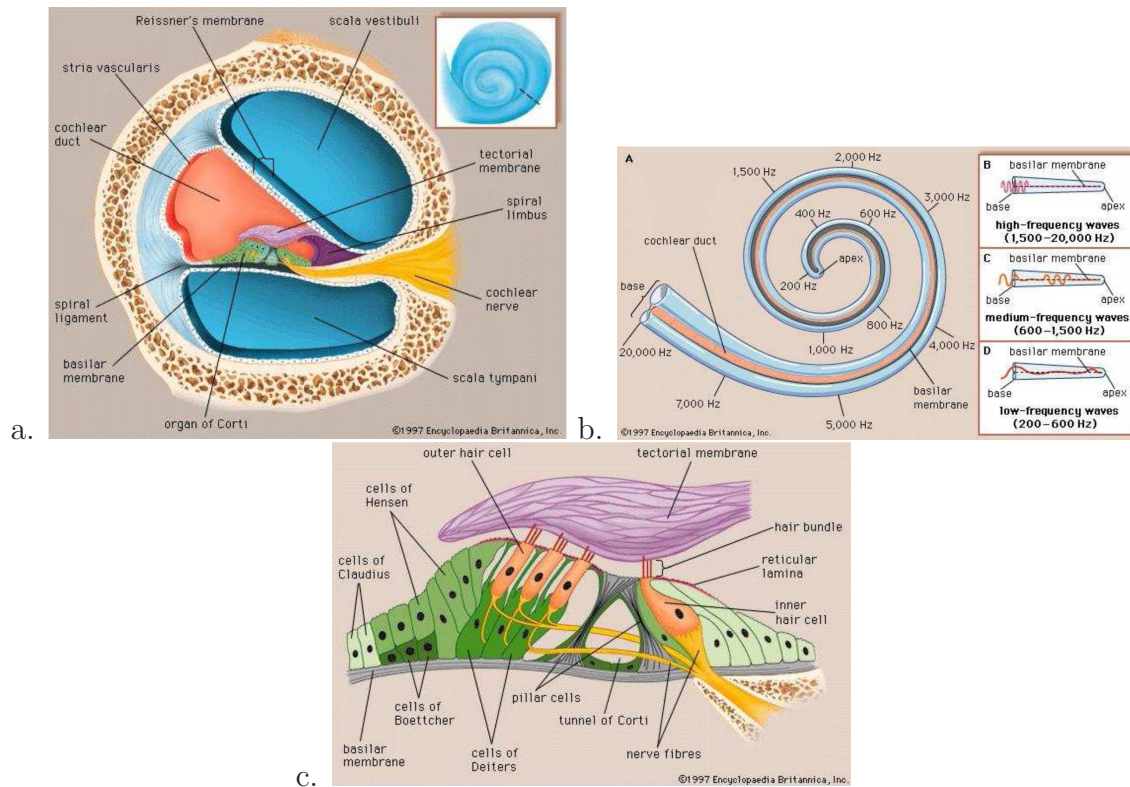
Figure 1.2: (a) Cross-section of one turn of the cochlea, showing the scala tympani, scala vestibuli, scala media (also called the cochlear duct), and the organ of Corti. (b) Tonotopic mapping of the cochlea. (c) Close-up cross-section of the organ of Corti. [3, 4, 5]

membrane (BM), while the SM and ST are separated by the Reissner's membrane. A cross-sectional view of the three ducts is shown in Figure 1.2a. Sound pressure waves enter the base of the cochlea via the stapes, which drives the oval window membrane and the fluid of the SV. The stapes drives a fast pressure wave in the cochlear fluid, as well as a slow wave that travels along the BM.

Mechanical representation of the cochlea can be simplified to two ducts (the SV and ST) separated by the BM, as shown in Figure 1.2b. The BM has non-uniform mechanical impedance along its length: at the base of the cochlea the BM is narrow, thin, and tensioned, while at the apex of the cochlea the BM is wide, thick, and compliant. The effect of this impedance variation is that incident sound waves have different locations of resonance on the BM, depending on frequency (a tonotopic mapping),

also shown in Figure 1.2b. As a result, incoming pressure waves encounter a change in impedance along its length, such that high frequency waves encounter a location of resonance near the base of the BM, while low frequency waves travel further into the cochlea and have a location of resonance near the apex of the cochlea [20, 9]. Sound signals entering the cochlea effectively undergo a Fourier transform. Purported active processes contribute to additional fine tuning of this tonotopic filtering through feedback. Three rows of outer hair cells (OHC) and one row of inner hair cells (IHC) run length-wise along the BM, seen in the cross-section view of the cochlea shown in Figure 1.2c. These hair cells are responsible for the conversion of the mechanical vibrations to neural impulses (IHCs) and for nonlinear feedback for the purpose of amplification and increasing the Q of the frequency filter of each frequency channel (OHCs). These hair cells, as well as the BM below them and the tectorial membrane (TM) above them, make up the organ of Corti. Hair cells are so named because of the bundles of stereocilia that extend from the top of the cells, which are the mechanism by which the hair cells perform the mechano-electric transduction. Deflections of the BM at the base of the hair cells are resisted by the tectorial membrane that is attached to the tips of stereocilia bundles, creating a sheer stress across the hair cells. In response to this stress the stereocilia deflect, elongating the distance between individual stereocilia. Tip link connections between each stereocilia stochastically open small ion channel trap doors on the stereocilia, allowing calcium and potassium to enter the cell body. The IHC are the sensing elements: depolarization of the IHC is converted to neural impulses, which are sent to the brain. The BM is organized tonotopically, so each IHC transduces a different frequency band of the incoming pressure wave. In this way, signals sent to the brain have already been decomposed into individual frequency channels. In the case of OHCs, the charge gradient across the cell body also induces a somatic deformation, which is thought to be the mechanism for the purported cochlear amplifier (this remains a subject of debate) [11, 12, 21].

6

1.1.3 Physical Models of the Cochlea

A number of physical models of the cochlea have been built, attempting to mimic the tonotopic frequency separation of the cochlea. In general these models can be categorized into the two broad categories of tapered membranes and cantilever arrays. A few notable models will be discussed, and a more thorough list of models is provided in Table 1.1.

Authors	Description
Chadwick and Adler, 1975	Two ducts, 6.3m long, separated by a stiff beam. No tonotopic mapping shown.
Cancelli, 1985 [22]	50:1 scale model that includes three silicone- filled fluid ducts separated by Reissners membrane and tapered, cross-wired BM. Organ of Corti and TM elements included. Authors measured BM amplitude and phase for 20-400Hz, as well as SM fluid motion.
Lechner, 1992 [23]	4.6cm long rubber tapered membrane with PVDF feedback actuators. Tonotopic mapping 40-400Hz, with filter sharpening as nonlinear feedback is increased.
Zhou, 1993 [24]	Tapered polymer membrane (defined by EDM machined steel plate), two ducts, 3.5cm long. Tonotopic mapping 300Hz-15kHz.
Haronian and Mac-Donald, 1996 [25]	An 3mm long array of acoustically coupled microfabricated thin beams tapering in length. Shows tonotopic response 3-10kHz.

Ando, 1998 [26]	An arary of microfabricated cantilevers in a fishbone shape. Authors demonstrate tonotopic mapping of cantilever resonances, as well as a preferred direction of energy flow from high to low frequencies.
Hemmert, 2002	3.5cm long microfabricated SU-8 polymer membrane with SU-8 orthotropic ribs, surrounded by two fluid-filled ducts. Vibrometer measurements of membrane recorded at one location.
White and Grosh, 2005 [27]	3cm long polyimide membrane with nitride ribs for orthotropy. Single fluid chamber. Tonotopic mapping demonstrated, mapping changes when fluid viscosity changed.
Chen, 2006 [28]	2cm long PVDF membrane with orthotropic metal ribs along the length. Single fluid channel.
Wittbrodt, Steele, and Puria, 2006 [29]	Polyimide tapered membrane 3.6cm long with orthotropic ribs. Membrane surrounded by fluid channels. Vibrometer measurement shows rough tonotopic mapping.
Bachman, Xu, Zeng, 2006 [30]	Optical cantilever array. Four cantilevers, 286-6948Hz resonances. Intended to replace front end processor.
Hur, Lee, and Choi,2010 [31]	PMN-Pt cantilever array. Four cantilevers, 1.46-4.05kHz resonant frequency span.

Inaoka, 2011 [32]	Two designs tested. One design was 3cm long PVDF membrane, 24 output electrodes. Outputs were amplified 60dB and sent to an electrode array implanted textitin vivo in a GP cochlea. An ABR threshold was evoked when 102dB_{SPL} of sound was played. The second design was a smaller curved PVDF membrane with two electrodes. Implanted in an excised cochlea, the stapes was driven. $30\mu\text{V}$ responses obtained for sound pressures of 109dB_{SPL}.
Kim, 2013 [33]	AlN membrane with an array of 16 electrodes. 2.5-19.3kHz resonances measured with vibrometer. No electrical response given. 6cm long membrane, intended as a front end of a CI.
Jung, 2014	2.8cm long PVDF membrane, 12 electrodes. Vibrometer membrane response measured. Single electrode response given.

Table 1.1: Brief descriptions of various artificial basilar membrane models (ABMs).

Early artificial basilar membrane (ABM) physical models were built as scaled up models of the cochlea that operated at low frequencies (20-400Hz). Cancelli built an impressive 3D scale model of the cochlea, complete with all three ducts, a tapered and orthotropic basilar membrane, and elements representing the tectorial membrane and organ of Corti [22]. This model displays tonotopic mapping across the basilar membrane and within the fluid of the scala media. Lechner also created a scaled up ABM that showed tonotopic mapping, but also included piezoelectric feedback actuators [23]. When nonlinear negative feedback was applied along the membrane, the Q of the mechanical filtering of the membrane increased.

The availability of microelectromechanical systems (MEMS) fabrication techniques enabled the machining of life-size ABMs that operate in the frequency range of human hearing, 20-20kHz. The earliest microfabricated ABM was made by Zhou in 1993 [24]. A steel plate had a tapered hole defined using electrical discharge machining (EDM), and a polymer covering was applied, to form a tapered membrane. Two fluid-filled ducts surrounded the membrane. The model is driven with a piezoelectric actuator, and the response is measured using a laser vibration measurement system. White developed two types of ABMs using MEMS batch fabrication techniques: one ABM design used a tapered nitride membrane, and a second design used a polyimide membrane with nitride orthotropic beams [27]. The membranes were mounted to a fluid-filled chamber and responses were measured using a laser vibrometer. Both designs exhibited tonotopic frequency mapping, and higher viscosity fluid in the chamber was shown to result in a lower frequency mapping.

More recently, Inaoka fabricated two designs of a MEMS-based piezoelectric (PVDF) membrane. The first design was a straight, 3cm long tapered membrane with 24 output electrodes, which showed tonotopic mapping [32]. The output from this array was amplified by 60dB and sent to an electrode array that was implanted in a guinea pig ST. The authors showed that an ABR could be evoked when a 102dB_{SPL} input sound was played at the membrane at an unspecified frequency. The authors then fabricated a smaller, curved tapered membrane, and inserted it into the ST of an excised cochlea. This membrane had two output electrodes, corresponding roughly to 5kHz and 20kHz frequency bands. A needle was used to drive the stapes, and an electrical outlet of approximately 20-30μV showed a response to 5kHz and 20kHz tones when driven with a 109dB_{SPL} tone, but no response from the structure.

An alternate ABM design that has been shown to have tonotopic response is an array of cantilevers with varied lengths, in a xylophone or fishbone shape arrangement. Haronian and MacDonald fabricated a 3mm long, 400μm-7mm wide array of

10

tapered thin beams that were $1\mu m$ wide and $10\mu m$ tall, and affixed at both ends [25]. Vibrometer measurements of the cantilever responses showed tonotopic frequency response, to be integrated later with an electronic readout system. Ando developed a fishbone-shaped array of cantilevers, with input and output membranes using microfabrication techniques [26]. The cantilevers were shown to have sharp tonotopic tuning when sound was played at the high frequency end of the array, but very little responsiveness when sounds were played at the low frequency end of the array, demonstrating a preferred direction of energy flow.

1.2   Deafness

Worldwide, 360 million people have a disabling hearing loss, which is defined as 40dB increased thresholds in adults and 30dB in children. According to the World Health Organization, half of these cases of hearing loss can be prevented [34]. Sources of deafness vary: at birth about 50% of the causes are genetic, however trauma and aging significantly increase the likelihood of deafness as a person ages.

Causes of hearing loss are divided into two categories: conductive loss and sensorineural hearing loss. Conductive hearing loss is defined as any hearing loss that occurs in the outer or middle ear, damaging the ability of sound to be conducted through to the inner ear. Sources of conductive loss include cerumen (ear wax), otitis media (middle ear infection), ear drum perforation, auditory canal blockage, damage to the ossicles, and tumors. Sensorineural hearing loss encompasses any hearing loss that occurs in the cochlea, auditory processing centers of the brain, or the vestibulocochlear nerve (the VIII cranial nerve). Sensorineural loss can occur from congenital defects such as aplasia of the cochlea, flattened epithelium, and loss from cytomegalovirus (pathogenisis not well understood), or genetic mutations. Diseases such as meningitis, mumps, measles, and rubella also lead to sensorineural loss. More commonly, sensorineural loss occurs from damage to IHCs and OHCs from sources such as oto-

toxic drugs, physical and noise-induced trauma, and age-related presbycusis (high frequency loss in the elderly).

1.2.1   Congenital and Prelingual Deafness

A survey of 4 year old children revealed that profound hearing loss occurs at an approximate rate of 270 incidents per 100,000 children [35], and that 54% of the cases were genetically caused. In comparison, the rate of congenital hearing loss (hearing loss present at birth) is 186 per 100,000, with genetic causes accounting for 68% of the instances. Therefore, while genetic cases account for the majority of instances of congenital hearing loss, other environmental sources and infections represent a significant portion of the sources of prelingual deafness.

There are many genetic causes of profound hearing loss,; a few of the most common are described in Table 1.2 [36, 35]. Approximately 30% of all cases of genetic hearing loss are syndromic, meaning they are accompanied by other non-hearing related symptoms; the rest are nonsyndromic [37].

While many sources of deafness are genetically caused, approximately half of all cases of birth-related deafness result from other environmental causes, such as diseases, birth trauma, and premature birth. Cytomegalovirus (CMV) infections account for approximately half of all non-genetic hearing loss causes at birth, making it the most prevalent cause of prelingual hearing loss in the U.S. [35]. CMV is particularly difficult to prevent because it can be clinically unapparent or late onset.

1.2.2   Traumatically Induced Hearing Loss

Hearing loss at birth accounts for only 4.4% of all reported causes of hearing loss. As the population ages, presbycusis accounted for 28% of hearing loss, excessive noise exposure another 33.7%, and ear infections accounted for another 12.2%. As a result of these factors, plus the effects of diseases such as meningitis, mumps, and measles,

Disorder	Prevalence*	Description
GJB2 Mutation	40	Also known as Connexin 26, this is the most common genetic cause of deafness. GJB2 is a gap junciton protein that is present in supporting cells of the Organ of Corti, as well as in the spiral ligament, stria vascularis, and spiral limbus, and is responsible for potassium transport. Some mutations to GJB2 are found in various syndromes, but the mutation is also associated with non-syndromic deafness.
Neurofibromatosis type 2	4	Caused by mutations in the NF2 gene that produces merlin, which is a protein that acts as a tumor supressor. Hearing disorders result from tumors in the hearing and balance nerve.
Pendred Syndrome	6	Thought to be caused by mutations in the LSC26A4 gene that codes the pendrin protein, though the mutation is present in only about half of all cases of the syndrome. Hearing loss is severe, and accompanied with temporal bone abnormalities such as enlarged vestibular aqueduct and possible thyroid enlargement.
Usher Syndrome	4	A syndrome that affects hearing and vision. Hearing and vision problems can either occur at birth or progresses during childhood. Particularly common amongst the Ashkenazi Jewish population.

*prevalence is per 100,000

Table 1.2: Common genetic causes of deafness and profound hearing loss.

approximately 0.5% of the population is deaf or hard of hearing [38] (about 1.5 million people in the U.S.).

1.3   Cochlear Implants

First developed from single electrode probes in the 1970s [15, 39, 13], CIs were first commercialized in 1984, when the FDA approved a 3M/House single electrode implant. This was followed soon after by the approval of the first multi-channel device, the Nucleus 22. This CI was moderately functional; it had a 30dB dynamic range and achieved sentence recognition scores of approximately 40%. Over the next 30 years CI technology dramatically improved. RF links now operate as high as 50MHz, allowing for high stimulation rates of up to 83kHz. Back telemetry was added to monitor cochlear health. Operating dynamic range is now as high as 70dB, and newer processing strategies have improved fine structure performance. As a result, modern devices are capable of producing as high as 87% to 98% sentence recognition at 70dB_{SPL}, though this varies greatly depending on hearing loss background and age of implantation [15, 40].

1.3.1   Commercially Available CIs

The US Food and Drug Administration estimates that approximately 219,000 people have received cochlear implants to date [41], making cochlear implants a multi-billion dollar industry. To date, three major cochlear implant companies share the market: Cochlear (Australia), MedEl (Austria), and Advanced Bionics (US). Of these, the Cochlear Nucleus implant series is the most widely used, representing 70- 80% of the worldwide sales in 2008 [15]. French-based Neurelec also has a commercially available cochlear implant. Two newer companies, China-based Nurotron and Korea based iEnjoy Music, are developing competing implants as well. Nurotrons Venus CI has been approved for use in China and costs half of the price of Cochlear implants

as such, it is poised to enter the international market soon. While several variants of the fully implantable cochlear implant have been tested (see Section 1.4.1, none are currently on the market.
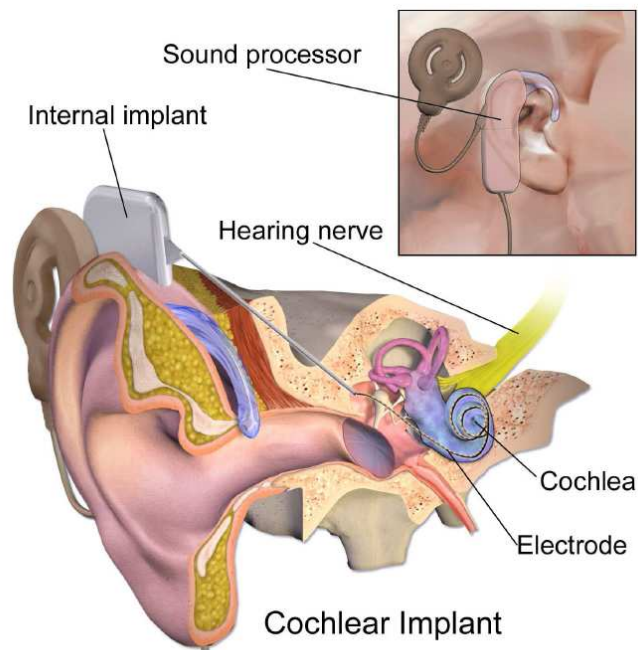
Figure 1.3: Schematic of a cochlear implant. [6]

All commercially available implants have a similar design, which is illustrated in Figure citeCIDesign:

1. An external microphone/processing unit that is housed behind the ear. The processor filters signals from the microphone into a set of discrete frequency band bins. For each time step, the processor then encodes one or more of the frequency bins that has the highest amplitude signal. This reduced signal is then amplified and sent to a transceiver unit for transmission to the internal portion of the CI.

2. An inductive link that transmits the information received from the processor to a subcutaneous receiving unit, which extracts the coded information and power and sends it through cabling to an electrode array that is implanted in the cochlea. Back-

ward telemetry is also sent from the internal CI about the health of the cochlea.

3. A probe that is inserted into the cochlea, that consists of a flexible silicone shank that has an array of 15-24 (depending on the company and design) Pt or PtIr electrodes and 2 grounding electrodes. Usually these electrodes are banded around the silicone, though some models have directional electrodes. The probe array is surgically inserted into the ST, and is wound through the cochlea for approximately one full turn.

1.3.2   Future Trends in Cochlear Implants

Because the design, characterization, and FDA approval process for new CI designs requires substantial amounts of time and resources, the major improvements in marketed CIs have focused on better processing algorithms and small changes to the implanted electrode array geometry that help the implant better curve around the modiolus. Manufacturers are also focusing on increased comfort and portability of the device by developing smaller battery packs and making the external processing units smaller, lighter, and water resistant. Hybrid CIs are also being developed that aim to preserve low frequency hearing through a combination CI-hearing aid device; the first hybrid CI just received FDA approval in 2014 [42].

Cochlear implant companies are also focusing on improved compatibility of CIs with electronics. All three major company product lines have bluetooth and RF connectivity to media player and cell phones. Advanced Bionics in particular has excellent compatibility of electronics, due to its shared technology with Phonak (a hearing aid company) [40].

16

1.3.3 Speech Processing in Commercial CIs

Cochlear implants can be stimulated either digitally (through the use of biphasic pulses) or with sinusoidal, analog stimulation that has been filtered through band pass filters. While analog stimulation provides better fine structure, it is generally outweighed by the benefits that digital biphasic stimulation, in particular the ability to digitally stimulate one electrode at a time, reducing inter-electrode phasing [43]. Digital signal processing has two common processing approaches: continuously interleaved sampling (CIS), and the more recent approach using fine structure processing (FSP). CIS is the most common processing approach used by commercial CIs. This processing approach begins with a selective filter of the audio signal to attenuate low frequency signals, to prevent low frequency noises from masking speech-range frequencies. The signal is then filtered through a set of bandpass filters. A biphasic pulse is then used, at constant sampling interval, to represent temporal envelope of that frequency band.

Fine structure processing is similar to CIS, except that the frequency of pulses used to encode each bands envelope is determined by the occurrence of zero crossings of the signal, rather than a predetermined frequency. While a CIS and FSP high frequency signal representation look similar, FSP uses far fewer pulses for low frequency bands than CIS does [44]. For CIS and FSP each biphasic pulse can be used to stimulate one electrode (monopolar), two electrodes (bipolar), three electrodes (tripolar), or a group of electrodes (phased array). In bipolar stimulation one electrode is stimulated with the biphasic pulse and the electrode next to it phase inversed. For tripolar the electrode is stimulated, and the two electrodes next to it are stimulated with lower amplitude, phase inversed pulses, in order to create a current density that has less spread. Tripolar stimulation allows for slightly improved place-mapping of frequencies, though it requires significantly higher amounts of power [45].

1.3.4 Power Consumption

While power consumption information is not easily available, Zeng estimates that commercially available CIs provide 20-40mW of power to the internal units, with 40% transmission efficiency [15]. These numbers match well with other estimations of 20-40mW (Saba thesis [46]) and 20-100mW (Cochlear CP810 User Guide). These numbers vary largely depending on the type of stimulation - tripolar and multipolar stimulation use substantially more battery life than monopolar or bipolar stimulation, as more electrodes are operated at any given time.

It is possible to estimate the power usage of a CI from the current used by the internal unit, which is between 1.2 and 1.9mA, depending on the device [15]. If one assumes a healthy implantation with little fibrotic tissue, the impedance of the surrounding cochlea will be approximately 5k. This corresponds to a internal power unit usage of 7 to 18mW. The transmission loss across the transceiver is approximately 15mW [46], proving an estimated power usage of 22 to 33mW, which is in line with the published estimations. However, any tissue growth or otosclerosis in the cochlea would necessitate a higher amount of power.

At present, the best battery lifetime is 183 hours (Advanced Bionics AAA PowerPak), when the user carries a relatively large battery pack. Battery life for a standard CI battery pack ranges from 17 to 36 hours for rechargeable batteries, and 50-90 hours with disposable batteries [40]. These battery limitations (and costs!) in particular make CI market penetration into non-first world countries a challenge.

1.3.5 Limitations

Cochlear implants have a number of limitations that have thus far reduced their effectiveness and global market penetration. The primary limitation of commercially available CIs to date is the cost of the device and implantation, which combined cost between 50 and 100 thousand dollars [16]. The high cost is due to a number

of factors, including the cost to manufacture the grossly sized, hand-made electrode probes, the lack of overall market competition (Cochlear dominates 70-80% of the global market), and the high cost of the difficult surgical implantation. It is certainly true that a smaller, less intrusive, batch fabricated implant would have a large effect market competition for CIs.

For those who opt for a CI implantation; CIs restore most of their speech function; however, CIs perform badly in noisy environments, have poor music representation, and operate over a limited frequency bandwidth. Current DSP units represent the envelope of sound signals well, but the fine structure of the signal is represented with limited success. Additionally, CIs can have high latency (5-20ms [30, 47]), which makes sound localization difficult in the case of unilaterally implanted patients that retain some hearing in the other ear. High power consumption, as mentioned in section 1.3.4, is also a major limitation.

In addition to the limitations from processing, CIs are also limited by how well they are implanted. The BM can be punctured during implantation, resulting in lower word recognition [48]. Sound localization can also be compromised if the implanted CIs frequency-electrode place map is not matched up to correspond with the actual CI probe insertion depth. Finally, infections, tissue formation, and ossification of the ST all limit the performance of the electrode array.

Overall, a patient who chooses to get a CI will restore some of their capability to hear, but at the loss of certain degrees of freedom. Daily activities like sleeping, bathing, and swimming require the removal of the external component of the CI, though newer CI models are becoming more water resistant. Other sports require extra safety precautions like helmets, and certain sports like boxing and deep sea scuba diving can no longer be done with a CI if head contact is likely. More critically, patients with CIs need an outpatient procedure to remove the CI receiver magnet if a MRI is needed, which can complicate a medical emergency. While these daily tradeoffs are certainly

made up for by the function of being able to hear, the current CI limitations provide a strong motivation to find new, innovative CI designs with reduced downsides.

1.3.6 CI Efficacy in Patients

Cochlear implants require relatively intact auditory nerves to be present, though regeneration of nerves is an active subject of research [49, 50]. Nerves can also selectively populate certain frequency regions of the cochlea but be missing or less densely populated for other frequency locations; in this case audiological tuning of CI electrode amplitudes can compensate to a limited degree.

The age of deafness and age of implantation also play a large role in determining how well a person will be able to use a cochlear implant to understand complex sounds. For the prelingual deaf implantation must occur before the age of 5-6 in order for the child to develop normal speech and language capabilities. When a patient is implanted past grade school age a CI becomes less useful; the patient will be able to hear, but they will not be able to process complex sounds due to reduced cortical plasticity [51].

1.4 Novel Cochlear Implant Designs

1.4.1 Fully Implantable Conventional CIs

Fully implantable cochlear implants are attractive alternative to the traditional cochlear implant, because they reduce the power needed to operate the implant by up to 60% by eliminating the transmission losses from the transceiver transcutaneously. A few of the relative merits of fully implantable CIs, as compared with traditional CIs, are detailed in 1.4. While the processing units for CIs can be made small enough to be implanted subcutaneously, the main limitation for making conventional CIs

Parameter	Commercial CI	Fully Implantable CI
Amount of power (est.)	20-100mW	1-10mW
MRI compatible?	No	Yes
External unit?	Yes	No
Shower compilable?	No	Yes
High impact sports	Not advised	Likely ok
Amount of signal processing	Heavy	Light
Latency	High	Low
Device on while sleeping?	No	Yes
Control of electrode frequency tuning	High	Low

Table 1.3: The relative merits of commercial and completely implantable CIs.

completely implantable is the microphone. In order for a CI to bypass a transceiver unit all of the CI must be implanted subcutaneously, including the microphone. However, microphones that are buried in this way lose sensitivity. Cochlear developed a fully implantable cochlear implant (TIKI) that was implanted in three patients, who reported that the internal microphones decreased sensitivity resulted in significantly lower speech perception than for a conventional CI, and that body noise interference was also an issue [52].

An alternate way to sense sound for a completely implantable CI is to have a microphone that senses sound in the middle ear, either from ambient sound or from coupled sensors to the middle ear ossicles. Young and Ko have developed a capacitive acclerometer-based microphone that senses ambient noise that was able to sense input sound levels as low as 35dB_{SPL} at 2-4kHz frequencies, but significant attenuation occurred for lower and higher frequencies [53]. However, middle ear microphones have great promise, particularly when combined with ultra low power processing units, such as the recent work done by [54].

1.4.2 ABMs as Passive Front Ends for CIs

An alternative strategy to building a fully implantable CI is to replace the front end microphone and processor with a passive ABM that sends individual frequency channels of information to corresponding electrodes on an implanted electrode array. Zeng developed a device with an array of cantilevers that acted as optical waveguides; larger vibrations of the cantilevers produced larger attenuation of the light received at the light receptacles mounted near the cantilever tips [30]. However, this design is unwieldy and requires an optical input. More recently, Choi develped a tapered AlN membrane with an array of 16 output electrodes and measured tonotopic response transfer functions with a vibrometer [55]. However, at present this device is far too large to implant (its measured dimensions are 5.8 cm by 6.3 cm), and the authors have not provided the sensitivity information for the device.

As described in Section 1.1.3, the most significant attempt at developing an ABM as a front end filter was Inaoka and Shintaku [32, 56], who fabricated a PVDF tapered membrane ABM with 24 electrical outputs. An input sound was played into the membrane, and the electrical responses were amplified by 60dB and sent to an implanted electrode array, evoking an ABR response for 102dB_{SPL} input sound pressure (unspecified input frequency). This in vivo application of the ABM as a cochlear implant front end was a successful demonstration of the ability of ABMs to act as passive front end filters, provided they can be miniaturized sufficiently to fit in the middle ear, and that a viable mechanism for packaging the membrane can be found that would retain the membranes sensitivity without having the device be subject to problems with fluid buildup and biocompatibility.

1.4.3 Cochlear Implants Using Sensors in the Cochlea

The strategy of using ABMs as passive front end filters that are implanted in the middle ear have several disadvantages, including the attenuation of sound in the middle ear cavity, reduced functionality when fluid is present in the middle ear cavity, and increased influence of body noises. An alternate approach to creating a fully implantable CI is to implant the sensing mechanism directly into the ST of the cochlea. If a sensor can be fabricated that is sufficiently small and sensitive, it can take advantage of the natural tonotopic mapping of the fluid and BM in the cochlea. Additionally, the device would house both the sensing units and the electrical output within the same unit, reducing the implant to the smallest possible size.

Two attempts to make a fully implantable CI, prior to the work presented in this thesis, have been documented in literature. The first was a PhD thesis by Mukherjee that aimed to create an array of cantilevers, over a range of resonant frequencies, that would be inserted into the cochlea however, the authors do not test the device *in vivo*, nor do they address how to make their device flexible for insertion into the first turn of the cochlea [57]. The other notable work was performed by Inaoka in 2011, and is described further in Section 1.1.3. The device consisted of a curved, piezoelectric membrane with two readout electrodes that was inserted into a portion of an excised cochlea [32]. The stapes of the excised cochlea was driven at an equivalent sound pressure level of 109dB_{SPL}, producing 20-30 μV of signal output that showed rudimentary tonotopic organization. While these results are very promising, there are problems with applying this design as a completely implantable cochlear implant. The design has limited sensitivity, requiring future significant amplification. Achieving an implantable membrane that can be implanted in a live animal will also require significant engineering to achieve the necessary flexibility, as the device will need to be able to be straightened for insertion and then to curve sharply once it is in the cochlea.

Three notable patents also propose vibration sensing in the inner ear, as opposed to at the ear drum or in the middle ear. Kim at KIMM in Korea describes a ZnO-based nanowire sensing mechanism that consists of sections of ZnO nanowires embedded in a flexible stylus [58]. Lupin proposes a piezoelectric material that curls through the cochlea to transduce sound [59]. Finally, J. Jacobs filed a Patent Cooperation Treaty (PCT) in 1990 that claims a series of transducers that are located along the length of a prosthesis and are amplified [60]. None of these three designs, however, have been fabricated or tested for viability to date.

1.4.4 MEMS-Based Cochlear Implant Electrode Arrays

Bell and Wise developed the first MEMS silicon thin-film electrode array at the University of Michigan [61]. The probe consisted of a silicon probe with 22 iridium oxide (IrO) electrodes and polySi leads. Active controls for site selection and position sensing were also included [62]. Bhatti improved upon this design by creating a 128 site (4 channels with 32 sites) array with an ASIC at the back end of the device capable of providing biphasic stimulation in monopolar, bipolar, and tripolar configurations [63, 64]. This array was integrated with a polyethylene therephthalate (PET) tube for pneumatic insertion. This design transitioned from curled to straightened well, but issues with the mismatch between the stiffnesses of the Si array and the tube had problems during implantation [65].

In order to reduce probe stiffness, Wang changed the probe backbone from Si to a parylene probe with a Si framework, complete with the active capabilities of previous designs [66]. The transition to parylene-based cochlear electrode arrays was developed further by Johnson, who developed a 32 site array with a parylene backbone and IrO electrodes. This array contained a layer thickness mismatch that caused intrinsic curvature to the probe [67, 68].

Another notable cochlear electrode array was developed by Bulcke, and consisted of
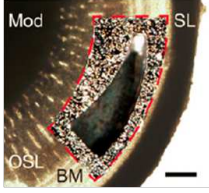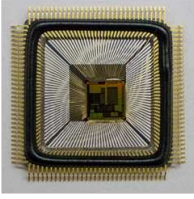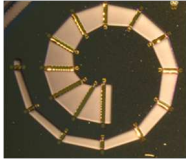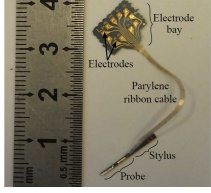
	Inaoka (Kyoto, Japan)	Yip (MIT)	Choi (Daegu, Korea)	CIAO (U of M)
Transduction Mechanism	PVDF piezoelectric membrane	Piezoelectric sensor attached to malleus	AlN piezoelectric membrane	AlN bimorph cantilever array
Processing Strategy	Passive filtering from membrane	Wirelessly charged small processor housed in middle ear	Passive filtering from membrane	Passive filtering from cantilever length tuning
Electrical Stimulation	Two large electrodes at 5kHz, 20kHz	Traditional CI electrode array (any)	Integrated electrode array	Outer electrodes of cantilevers
Biological Testing So Far	Implanted in an excised guinea pig cochlea	Sensor tested on human cadaveric temporal bone	None reported	Acute *in vivo* test in guinea pig
Designed for *In Vivo* Testing?	No	Yes	No	Yes

Table 1.4: A comparison of current completely implantable CI designs.

22 distributed electrical sites along a flexible parylene-silicone probe /citeBulcke2006. This creative approach did allow for integrated electronics with only five bus lines, but the fabrication process for this device is very challenging, and no *in vivo* results for this design have been published.

1.5   Thesis Contributions

This thesis presents the design, fabrication, and *in vivo* and *in vitro* testing of a novel cochlear implant design. This cochlear implant consists of an array of piezo-

electric cantilevers that locally transduce the pressure waves in the scala tympani into electrical signals. We propose that this design is capable of replacing the frequency filtering and transduction functions of the organ of Corti by this transduction mechanism, and therefore we title this implant the Compeletely Implantable Artificial Organ of Corti (CIAO). Unlike previous efforts to build a completely implantable CI, this thesis presents a completely implantable CI prototype that has been designed to facilitate acute and chronic *in vivo* testing without requiring that the cochlea be excised. Only two electrical lines extend from the CIAO device to the top of the guinea pig head for electrical monitoring; the rest of the CIAO implant is completely sealed for *in vivo* testing.

A description of the CIAO implant description is presented in Chapter 2. We also present considerations in designing the implant to be compatible with long term *in vivo* testing. The a brief overview of the fabrication process to build the CIAO implant is given, followed by a discussion of the merits of two different device designs. Chapter 3 discusses the modeling that is used to design the device geometry such that each cantilever of the CIAO device has the correct resonant frequency response. A model of a multimorph cantilever in a viscous fluid is used. *In vitro* measurements are presented that demonstrate that the model predicts the resonant frequency of a wide cantilever to within 50% of the measured resonance, but that the model overestimates the mass loading and underestimates the damping of the fluid when the cantilever is wide and has a short length. Finally, we discuss the predicted *in vivo* device response when a pressure source is introduced at the ear canal.

The CIAO device depends on high quality piezoelectric material to achieve low noise and high sensitivity performance. In Chpater 4 we present characterization of the aluminum nitride (AlN) deposition process, with the goal of optimizing film properties such as crystal quality and piezoelectric coefficeints. High resolution transmission electron microscopy imaging of AlN film growth is presented, revealing that the AlN

film generally has good growth properties, but that initial seeding of the AlN results in 5-6nm of disordered stacking every time a deposition process is started or terminated. Chapter 4 also presents characterization of wet etching of AlN at various temperatures, with the goal of achieving two-step AlN via etch process consisting of a dry AlN etch followed by a wet etch; this combination results in a via etching process that has minimized undercut and good etch selectivity to metal.

Chapter 5 presents the *in vivo* response of the fabricated CIAO devices. Two CIAO devices were implanted in guinea pigs for acute measurement of device response. *Post mortem* analysis of the implantations revealed that all five cantilevers were broken during the first implantation, but that four of the five cantilevers remained intact during the second implantation. Device performance for the second implantation reveals promising initial confirmation of the CIAO device. When a 110dB_{SPL} sound was played at the ear canal of a deafened animal, a $2\mu\text{V}$ device response was measured, which was confirmed to be a larger response than either measured crosstalk or device noise.

CHAPTER II

CIAO Design and Fabrication

An overview of the Completely Implantable Artificial Organ of Corti (CIAO for short) implant is provided in this chapter, followed by details of the CIAO implant design and fabrication considerations. Two CIAO implant generations have been fabricated, and a comparison of the relative merits of both designs is provided.

2.1 CIAO Implant Overview

The CIAO implant concept consists of an array of piezoelectric bimorph cantilevers that are spaced on a probe that extends into the scala tympani. The pressure of the sound vibrations in the ST fluid deflects the cantilevers, producing a potential on the outer electrodes of each cantilever (when the middle electrode is connected to animal ground). The outer electrodes are open to the surrounding perilymph in the ST, producing an ionic current that stimulates the spiral ganglion, shown in Figure 2.1b.

Unlike traditional CIs, the CIAO device derives its frequency filtering from the resonant behavior of the cantilevers, coupled with the tonotopic frequency organization of the basilar membrane, to filter incident sound signals. Each cantilever is designed to have an operating resonance, in fluid, that matches the corresponding BM resonant frequency at that cantilevers insertion depth using the Greenwood frequency place-

ment map [69]. Cantilevers of this design have been shown to function as low noise, highly linear microphones [70, 71]. The resonant frequency response of this cantilever design is easily tuned by changing the thickness and length of the cantilevers.

By using geometry to control each cantilever's operating frequency as opposed to DSP, the CIAO device is engineered not to need any external sound processor. The functional portion of the CIAO device resides entirely within the cochleas ST, though some small external connection is necessary to provide the amplification of the signals from the cantilevers. Additionally, the CIAO implant can be alternately wired to function as an array of implanted microphones that measure fluid pressure in chronic measurement environments.

One potential advantage to the use of a device like the CIAO design, which uses passive analog filtering, is that details of the fine structure of the input signal should be better represented [43]. This is because commercial CI processing algorithms emphasize correct representation of the sound envelope, but often throw out all but the highest amplitude band of information for each time step. While this does not significantly affect CI speech performance, this processing technique is certainly not correct for representing complex sound signals such as music.

For this thesis, a CIAO implant prototype was constructed that consisted of five cantilevers of varied length, forming a "xylophone" configuration, shown in Figure 2.1a. This prototype is not flexible; as a result, the probe can only be inserted into the straight basal portion of the guinea pig cochlea. Future CIAO generations will address flexability, however, the CIAO probe detailed in this thesis was designed to be straight to simplify the fabrication process for the initial tests of the design proof of concept. The cantilevers span 20-40kHz, which corresponds with the prototype's insertion depth in the guinea pig.

We present the design, fabrication, and implantation of a CIAO implant that is capable of measuring ST fluid vibrations when a sound is played at a deafened animals ear.

29
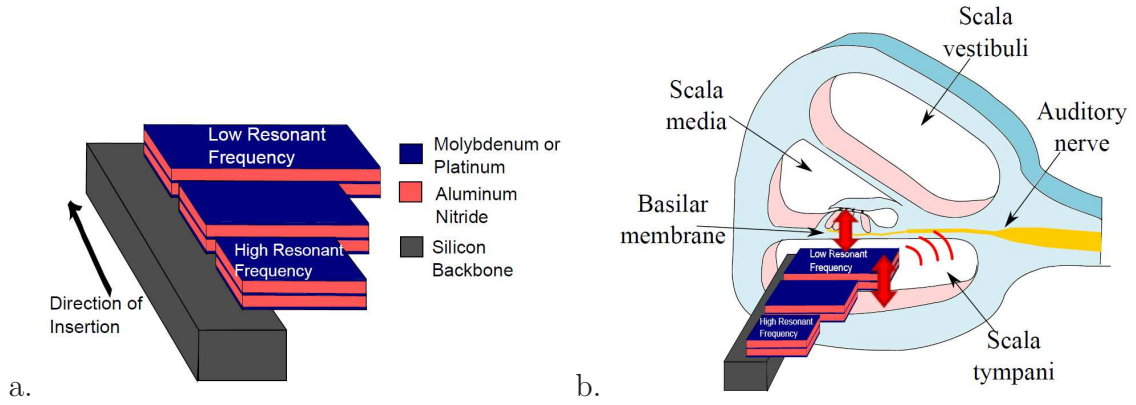
Figure 2.1: (a) The xylophone arrangement of the CIAO cantilevers of the fabricated prototype described in this thesis (a), and a schematic of the CIAO implant prototype when implanted in the ST (b). When implanted, fluid pressure in the ST deflects the cantilevers, producing a potential on the outer cantilever electrodes, which in turn produce an ionic current that stimulates the spiral ganglion.

With sufficient amplification, the CIAO device is designed to be capable of evoking an ABR response in a deafened animal. Unlike previous efforts to produce fully implantable CIs, the CIAO implant is designed for chronic in *in vivo* experimentation. We demonstrate implant functionality with acute *in vivo* testing with the implant fully sealed off; this testing method is fully compatible with future chronic studies.

2.2 CIAO Physiological Considerations

2.2.1 Material Choices

Materials that can be used in biomedical implants are limited to those that do not provoke an inflammatory response [72, 73]. Criteria for stimulating electrodes are even more strict, as stimulation electrodes will produce oxidation-reduction (redox) reactions if stimulation levels are too high [74]. Metals used in the CIAO implant were therefore limited to biocompatible materials, with the exception of AlN, which has only been demonstrated to be biocompatible in chronic in vivo cortical measurements in rats [75]. Materials used for the CIAO implant are therefore limited to Si, silicon

30
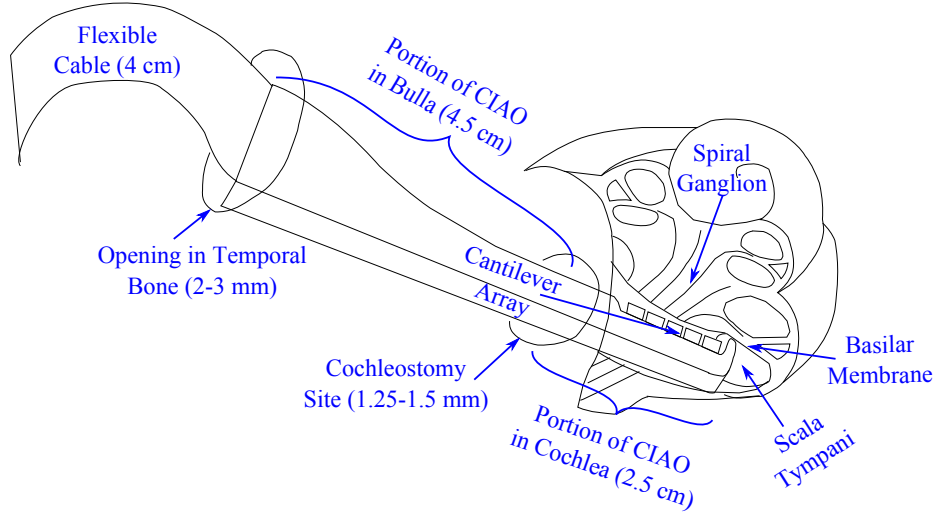
Figure 2.2: The placement of the straight CIAO implant in the cochlea.

oxide, Ti, Pt, AlN, Cr, Au, and parylene C.

There are four primary options for stimulating electrode materials: Pt, Au, Pt/Ir, and iridium oxide (IrO) [76, 72]. Of these Au is the least optimal because of its low current injection [77]. IrO has the highest current injection capability, but it requires a separate oxidation process to grow the IrO from Ir, and IrO electrodes degrade over time [67]. PtIr electrodes are used in commercial CIs and have good charge injection capabilities [15, 67], but are difficult to sputter, costly, and are untested as substrates for AlN growth. For the CIAO project, Pt was chosen as the preferred electrode metal because it has three times the charge injection capability of Au [77], is easy to sputter, and is well characterized as a substrate for AlN growth [78]. However, transition to a top electrode layer composed of PtIr might be beneficial in the long run to produce higher current injection.

2.2.2 Geometrical Constraints

A schematic of how the CIAO prototype fits into the cochlea is shown in Figure 2.2. Initial *post mortem* tests of probe prototypes revealed that approximately 2.5mm of a probe tip (the distal portion of the probe) could be inserted into the straight

31

basal portion of the guinea pig ST for a probe measuring $500\mu m$ width and $525\mu m$ thickness. Given this insertion depth, the CIAO device was designed to have an array of five $400\mu m$ wide cantilevers, spaced $100\mu m$ apart. An additional length of 4.5mm of probe length was required to extend from the cochleostomy site to the opening of the temporal bulla. Implantation was facilitated when one edge of the CIAO probe had a straight line for visualizing implantation. For implantation, the cochleostomy site was approximately 1mm basal from the round window, and was 1.2-1.5mm wide. The CIAO cantilevers were protected by a $200\mu m$ thick, rounded tip section of the Si backbone. Initial CIAO designs also included a $50\mu m$ thick bumper that ran along the line of the cantilever ends but this removed because it was too fragile and often broke off, knocking off cantilevers in the process.

Cabling for the CIAO implant is 4cm long, and it was found that prescribing a wide angle curvature to the shape of the cable was not necessary. The cable should not exceed 2mm in width. The cabling connects to an electrode bay head piece for external electrical measurement; this head piece is connected to a set of pins that relay the electrical information to external recording equipment. The head piece is secured to the top of the skull using dental cement so that the animal cannot dislodge it during chronic *in vivo* studies. This head piece can be as large as 0.8mm by 1mm, but is optimal when it is 0.8mm by 0.8mm square.

Prior to *in vivo* implantation, *post mortem* testing was conducted to verify that the CIAO implant cabling was robust enough for implantation. Imaging of this test is shown in Figure 2.3a, and shows that the probe was successfully positioned in the ST with the cabling intact. Additionally, the opening to the bulla was opened as wide as possible to determine the maximum probe widths possible for future probe designs (Figure 2.3b). Implants with a 2.8mm wide block could be tightly accommodated (though the hole was still possibly too wide to reseal during chronic testing), but a
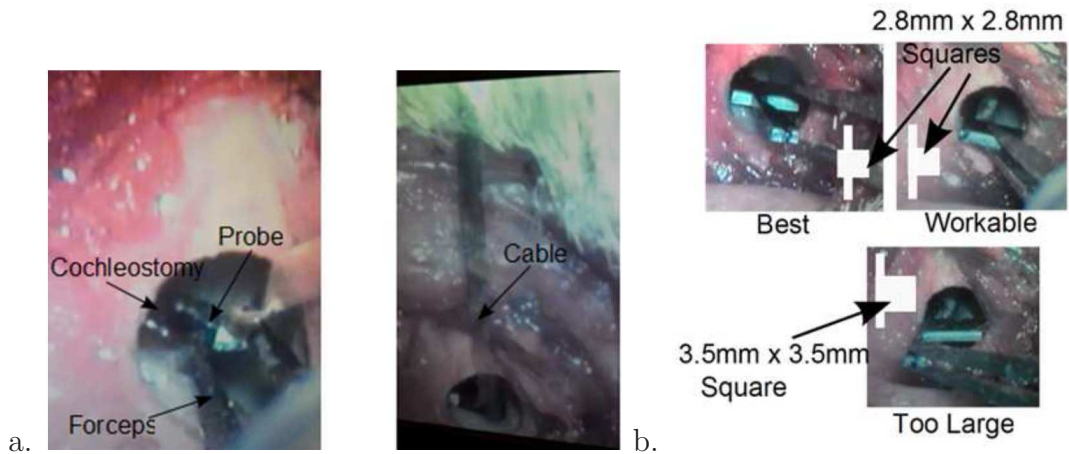
Figure 2.3: *Post mortem* testing of a fabricated CIAO implant was conducted, prior to *in vivo* implantation, to test the integrity of the probe and cabling (a). Additional dummy prototypes were tested to determine the available space in the bulla for accommodating a larger probe (b).

width of 3.5mm was too large. From these tests it was determined that the back end of the second generation probe could be widened from 500μm to 1.3mm wide, and that there was enough space to accommodate an amplifier on the probe that had a footprint smaller than 2.5mm by 2.5mm.

2.2.3   Week Long Dummy Implantation

The inflammatory response evoked by the probe implantation was tested using a one week in *in vivo* implantation of a probe prototype in a guinea pig. The non-functional prototype was fabricated from silicon, with silicon dioxide (oxide) cantilevers, shown in Figure 2.4a. All of the oxide cantilevers were located in the basal portion of the guinea pig ST during this test, and the cochleostomy site was closed using a muscle plug. The temporal bulla was closed using dental cement. During the week of implantation, the guinea pig showed no signs of discomfort, vestibular problems, or infection.

Post mortem evaluation revealed that the ossicular chain and upper turns of the cochlea were in tact, as was the bony modiolus, which contains the spiral ganglion

cells. Granulation tissue around the basal cochleostomy was observed, and shearing damage to the basilar membrane occurred. Figure 2.4 shows the dissected guinea pig cochlea, before and after the outer cochlea is removed (2.4b and c, respectively). In 2.4c the implanted device is visible, and is surrounded by some granulation tissue.

2.3   Fabrication Process

The process for fabricating the CIAO device is shown in Figure 2.5. In general, this process can be categorized into three process steps: the fabrication of the probes with AlN cantilevers, the patterning of the accompanying electrical cabling, and the release of the structures.

Substrates used for this fabrication process are double side polished p-type Si wafers coated with 2μm of thermal oxide, which serves as the electrical insulation between the device bottom and the Si wafer. The top oxide layer is thinned using reactive ion etching (RIE) to a 1μm thick, while the backside oxide is kept 2μm thick (to be used later as a mask for the backside patterning). A bottom Ti/Pt (15/80nm thick) layer is sputter deposited and patterned (using the Lab 18-02 sputter deposition tool and the STS Glass Etcher RIE tool, respectively) to form the bottom electrode layer. A blanket AlN layer (1.5μm or 2.5μm, depending on the design generation) is then deposited in an AMS 2004 AlN sputter tool, with a focus on achieving a stress passivated AlN layer. A second Ti/Pt (15/80nm) electrode layer is deposited and patterned in the same way as the first, followed by a second blanket (stress passivated) AlN layer matching the first. These steps are shown in Figure 2.5a. Vias are then patterned to access the buried electrode layers. A blanket 2μm PECVD oxide layer is deposited, followed by a SPR 220 patterned photoresist layer defining the via locations. An oxide etch is used to pattern the via shape into the oxide, followed by a Cl-based RIE etch to etch the via into the AlN [LAM 9400], but the
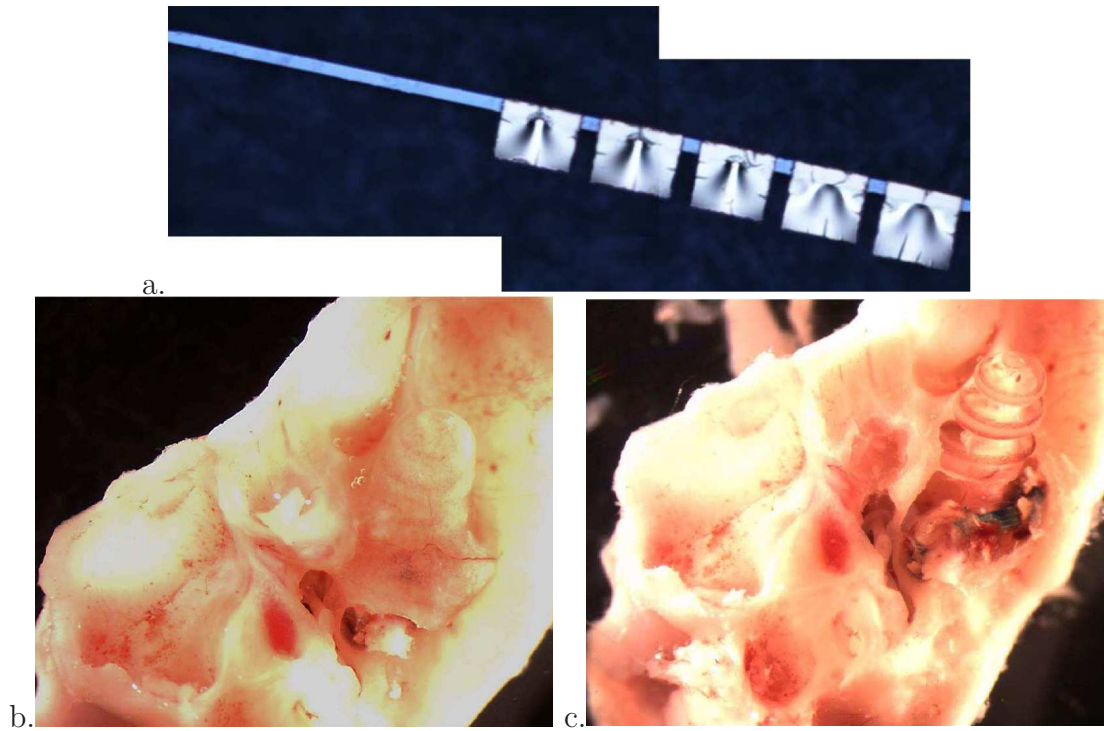
Figure 2.4: The implanted non-functional prototype (a), and the *post mortem* image-safter a week long implantation. The cochlea is in tact with the muscle plug removed (b), and with the temporal bulla bone and outer cochlea bones removed (c) to show the inner cochlea. The probe is shown fully inserted into the basal turn, surrounded by some granulation tissue.
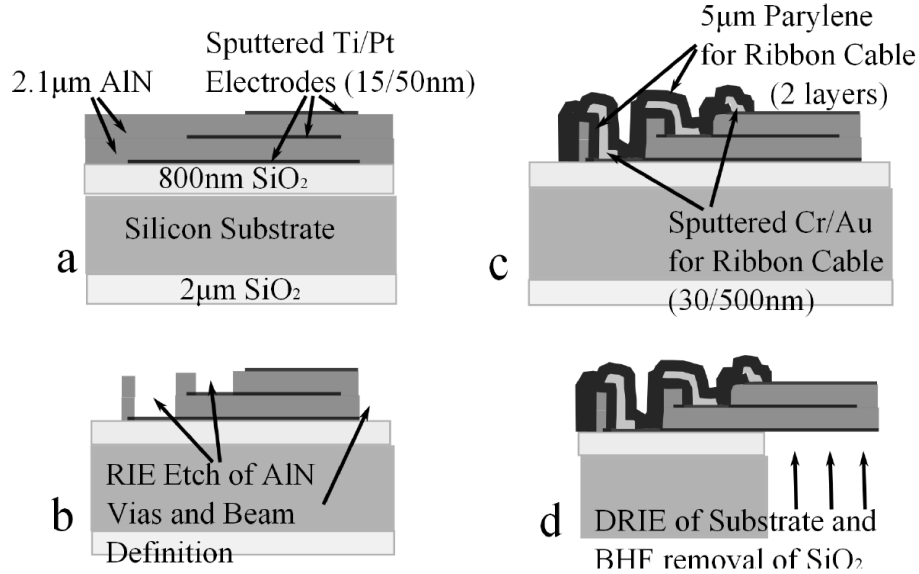
Figure 2.5: The fabrication process. AlN layers are deposited separated by patterned Ti/Pt layers (a), subsequently the AlN is patterned to allow access to the bottom and middle traces (b). A parylene, Cr/Au, parylene ribbon cable is then deposited (c), and the device is released using DRIE and a BHF etch (d).

etch is terminated within 0.5μm of the electrode depth for each electrode layer, as the RIE etch does not have the selectivity to stop directly on the electrode. The photoresist is removed, and the patterned oxide serves as the masking layer for a heated AZ400K etch (50C, KOH-based) etch that removes the remaining 1μm of AlN, stopping on the underlying Pt (Figure 2.5b). Wet etching is not used to define the entire via location, because the length of time required to pattern through thicker AlN is sufficient to produce significant etch undercut and pinhole etching; more detail on this behavior is presented in Chapter IV. The oxide film is then removed (with photoresist protecting the opened vias on the topside and the backside oxide) using an HF bath.

Following the via etching, a third Ti/Pt layer is deposited and patterned to form the top electrode layer. For this etch the vias are also protected, to prevent overetching of the via metal layers. Alternately, this step can be done using sputter liftoff with

SPR 220 photoresist, as all of the features for this layer are large. Metrology of the films is performed at or before this step, including measurements of the device capacitances, film dissipation factor, and X-ray diffraction (XRD) analysis of the AlN film quality. The blanket AlN is then patterned to define the shapes of the cantilevers. Because AlN acts as an insulator, the blanket AlN is left along the full length of the probe and traces are run in the bottom Pt layer, for electrical insulation. A Cr/Au (20nm/400nm) layer is the final step; this layer is used for any additional necessary electrical connections, including bond pads and shorting between the top and bottom electrodes.

The parylene ribbon cables are fabricated in conjunction with their electrode bays; together these comprise the electrical cabling that is added to the CIAO device to allow for electrical monitoring, but is not required for the CIAO device to function. An initial 5μm thick parylene layer is deposited and patterned using an oxygen plasma etch [LAM 9400]. On top of this a Cr/Au (or Cr/Au/Cr) layer (Cr layers are 20nm, Au is 400nm) is sputter deposited [Lab 18-02] and patterned either with wet etching or liftoff. In the case of cables that require ball bonding, this step is followed by a selective electroplating of the Au to a thickness of 2.5μm at the bond pad locations. A second 5m thick parylene layer is then deposited and patterned, such that the electrodes at the electrode bay are exposed (and bonding pads, if applicable). This process is shown in Figure 2.5c, and can be performed either in conjunction with the probe fabrication or on a separate substrate (if separate, bonding to the probe is required).

Deep reactive ion etching (DRIE) is used to define the shape of the Si probe and the electrode bay. The DRIE etch is masked by the backside 2μm of thermal oxide, which is patterned using an RIE oxide etch [LAM 9400]. The wafer is mounted, backside up, to a carrier wafer using a combination of 3μm photoresist - PFPE lubricant - 3μm photoresist. A slow DRIE etch [STS Pegasus 4" tool, Recipe 1] is used to etch

through the wafer, stopping on the 1μm thick layer of thermal oxide on the topside of the wafer (Figure 2.5d). At this point the underside of the cantilevers are visible, but are protected by the carrier wafer and the oxide etch stop layer.

The etch stop layer, as well as the Ti on the underside of the cantilevers, is removed using a BHF etch. An acetone bath is then used to remove the photoresist that holds the process wafer to the carrier wafer. This bath can be repeated as necessary to ensure proper PFPE removal. Break-off Si and parylene tabs are used to hold the probes and cabling to a surrounding Si structure aids this release process - the carrier wafer can be removed but the support structure will hold the probes in place, allowing for safe transport.

2.4 Fabrication Considerations

A primary requirement for the CIAO device to function well is the repeatable deposition of high quality, stress controlled AlN. The AMS 2004 sputter tool that is used to deposit AlN at the University of Michigan generally produces high quality AlN films (this is quantified in the Chapter IV), but a number of factors affect the film stress, including substrate, target life, gas flow, RF substrate bias, AC target power, chamber pressure, chamber preparation, and pre-deposition vacuum; in essence, every parameter that can be changed during deposition will affect stress. Control and characterization of these parameters are discussed in detail in Chapter IV. Care is also required when devices with AlN are processed, because AlN reacts with traditional KOH and TMAH-based developers. In response to this, only CD-30 developer and the corresponding compatible photoresists are used. Processing using liftoff techniques (where a layer of sacrificial photoresist is patterned to cover areas where metal is not desired, blanket metal is deposited over the entire wafer, and the photoresist is removed, in turn removing the metal that was deposited on top of the areas with photoresist but not the areas clear of photoresist) is limited, because the
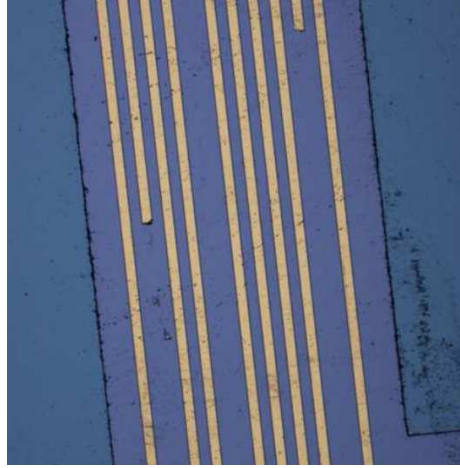
Figure 2.6: Cr-Au traces on parylene. The poor adhesion of the traces to the underlying parylene was exacerbated by Cr undercut and the stress imbalance between the Au and Cr layers.

standard photoresist for liftoff, LOR, is not compatible with CD-30. In lieu of liftoff metal patterning, Pt and Au layers are etched using RIE (Pt) or wet etching (Au) techniques. In the case of wet etching, trace thickness is not easily controlled, and any undercut of the adhesion layer for the Au will produce trace delamination, shown in Figure 2.6.

Attention must also be paid to protecting the thin Pt electrode layers, particularly in the via locations. Hydrofluoric acid (HF) etching can undercut the Pt electrodes if they are too thin, and etch the underlying Ti adhesion layer, so when possible the vias should be protected using photoresist during HF etching. Additionally, the oxygen plasma etch used for parylene etching was observed to etch through the Pt layers. To prevent this, it is effective to pattern a protective thin PR layer to cover the electrodes prior to the blanket parylene deposition - this PR layer serves as an etch stop for the parylene layer and protects the underlying Pt.

Considerations must be made during the deep reactive ion etching (DRIE) process because AlN cantilever lengths are effectively defined by the location of the edge of

the Si backbone. Therefore, the amount of undercut that occurs during the DRIE process must be carefully controlled to achieve desired resonant frequency responses. In practice, this amounts to compensating for approximately 20μm of undercut for devices that are near the edges of the wafer; no compensation to the patterning is needed for devices near the center of the wafer.

Finally, a special method of mounting the process wafer to the carrier wafer for DRIE is also used. Both wafers have 3μm of photoresist spun on their top faces, and then they are joined using a thin layer of PFPE lubricant in a vacuum chamber. This technique has been determined to be optimal for mounting, as it has acceptable thermal transmission properties, is easily and completely removed from the surface of the fragile released cantilevers, and minimizes the stress the cantilevers experience when the Si is fully removed but the thermal oxide etch stop layer has not yet been removed.

2.4.1 First and Second Generation Design Comparison

The initial design of the CIAO device, called the Generation 1/Gen 1/Monolithic device, used a monolithic fabrication process, wherein the probes, cable, and the head piece were all fabricated in a single process. This design, shown in Figure 2.7a, included the capability for separately addressing each cantilevers top and bottom electrode, and had a curved, integrated 3 cm long cable. Due to the long fabrication process to build this device, a second device generation (called Generation 2/Gen 2, shown in Figure 2.7b) was developed that separated the probe fabrication process from the cabling process. This design allows for an increase to 60 probes per wafer, as opposed to 11 in the Gen 1 design), and separating the two processes allowed for parallel processing that greatly reduced overall probe fabrication processing time. However, establishing reliable connection of the probe to the cabling remains a challenge. A discussion of the differences between the Gen 1 and Gen 2 designs is
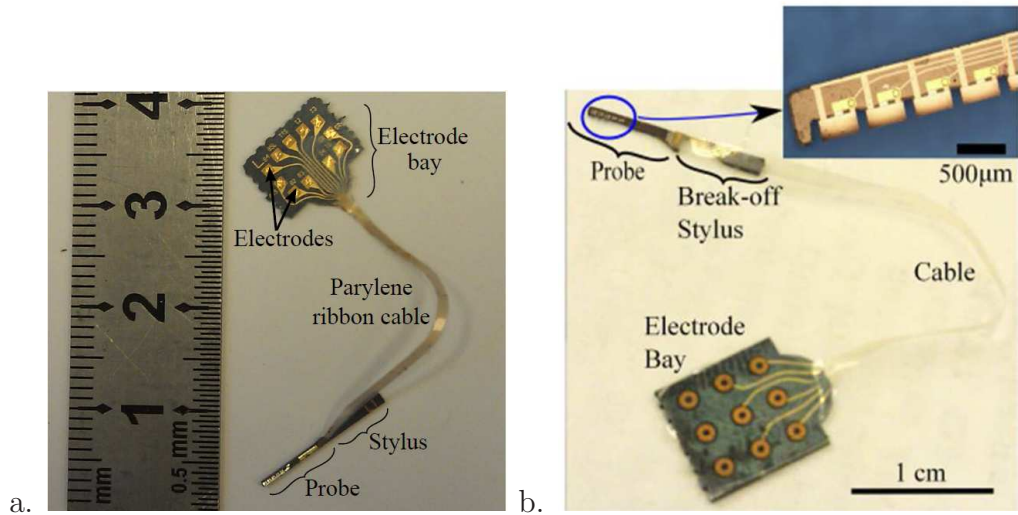
Figure 2.7: Fabricated first generation prototype (a) and second generation prototype (b). A discussion of the differences between these two generation designs is given in Table 2.1.

presented in this section, and is summarized in Table 2.1.

2.4.2   Probe Design

Initial guinea pigs *post mortem* tests using non-functional prototypes prescribed the geometrical constraints of the Gen 1 design, limiting the probe size to a footprint of 500μm width, 7mm of length, and a standard Si wafer thickness of 525μm. Due to these size limitations, it was determined that the requisite area needed for bonding (100μm square pads) was not available, and that a monolithic process that integrated cabling with the probe was required. However, later *post mortem* testing revealed that a probe width of 600μm was acceptable (though not preferable, as it requires a large cochleostomy site) for the section of the probe that enters the ST. Additional testing also revealed that the hole in the temporal bone, exposing the bulla, could be as large as 2-3mm, and that the base of the probe (the part that is not in the ST) could be widened from 500μm to 1.3mm - this increase in size was enough to allow for cable
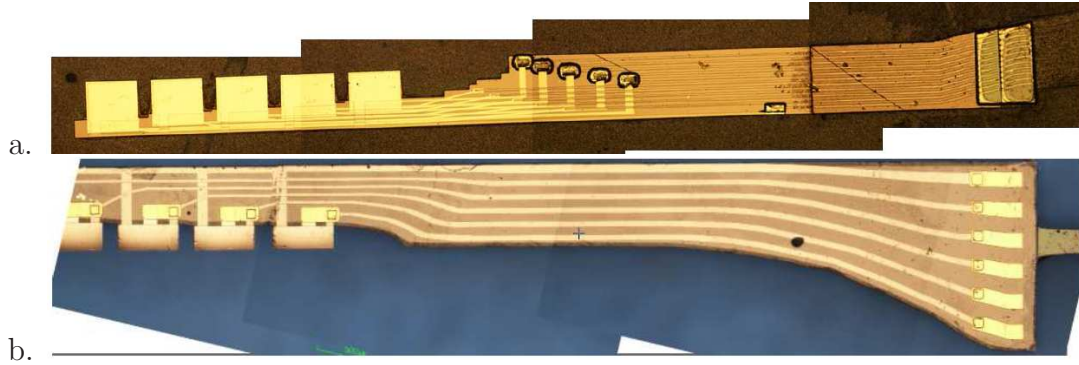
Figure 2.8: The patterning on the monolithic prototype. Initial fabrication had 11 traces extending from the probe (a), but was modified to six buried traces in the second generation design (b).

bonding.

The added probe tip width allowance for the Gen 2 design was further improved by a decision to remove the Si bumper meant to protect the cantilevers (but which was deemed not effective). The AlN layer thickness was reduced from 2.5μm to 1.5μm as well; because the cantilevers were thinner, they also needed to be shortened to maintain the requisite resonant frequencies. In combination, these changes allowed for enough space along the probe tip in the Gen 2 design to allow for vias and patterning that locally shorted the top and bottom electrodes of each cantilever, as can be seen in Figure 2.8. Only 6 traces were then run from the cantilevers (the outer electrodes of each cantilever, plus a common middle ground electrode). These traces were drawn using the bottom Pt layer, and were run, embedded, to the base of the probe, where large pads were exposed for bonding. Images of the trace design differences between the Gen 1 and Gen 2 designs are shown in Figure 2.8.
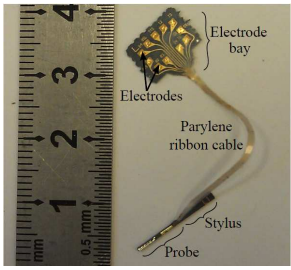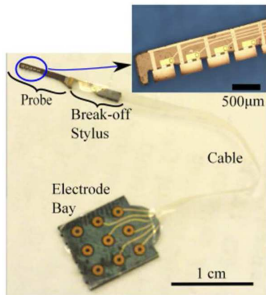
2.4.3 Cabling and Head Piece

The Gen 1 device used an integrated 3cm long, 1mm wide parylene cable, which was fabricated as part of the same process as the AlN probes. Integrating the cabling is crucial when the space footprint is too small. In the case of the Gen 1 device,

11 electrical lines were required to fit within a 500μm wide space - given that bond pads require approximately 100μm width with 100μm spacing, bonding was not easily achievable, and instead the cable fabrication was integrated in with the probe. While monolithic processing of the probe and cable allows for probes with smaller back end footprints and a higher trace density, it does have a number of disadvantages. Most importantly, when the probes and cabling are fabricated on the same wafer, the time for device fabrication is extended because the cabling and probes cannot be fabricated in parallel. Additionally, the cabling takes up a significant amount of space; the monolithic process produced 11 probes per wafer, while the Gen 2 separated design produced 60 AlN probes per probe wafer, and 15 cables per cable wafer. Bonding between the cabling and probes is achieved by gold bump ball bonding, described in Meyer, 2001 [79] by designing the cable termination sites as Au toroids with holes in the middle. Alternately, square termination pads can be used in conjunction with either anisotropic conductive adhesive (ACA) [80] or wedge or wire bonding.

The head piece design (also called the electrode bay) for the Gen 1 device consists of a 0.8cm by 1cm rectangular section of Si, with jagged edges to help improve glue adhesion when the head piece is mounted to the guinea pig skull in *in vivo* testing. Eleven 1mm square Au electrodes are spaced in a circular pattern around the mount. This design was altered for the Gen 2 device, in order to integrate with existing electrical readout equipment available at the Pfingst lab at the Kresge Hearing Research Institute (KHRI). The six electrical paths that are in the Gen 2 design instead terminate at a 3x2 array of 1.2mm diameter circular electrodes. Additionally, the head piece was reduced in size to 0.8cm by 0.8cm, and the roughened edges were removed. For chronic *in vivo* studies, female receptacles for pins are silver epoxied to each electrode, and the head piece is to be mounted using durelon epoxy or biocompatible cement to the skull. A separate electrical board pins into the receptacles, and routes them to a single multi-pin cable termination. Testing can then be performed by simply

plugging in a cable to that termination, providing simultaneous and separate access to each of the six electrical paths.

	Monolithic (Gen 1)	Second Generation
Description	Whole CIAO device is fabricated in one 14-mask process	CIAO device fabrication separates probe from cable fabrication
Probe Dimensions	500μm wide (whole length), 7mm long, 50μm wide bumper running along tip edge of beams.	600μm wide at tip, widens to 1.3mm wide at base, 7mm long, no bumper.
AlN Thickness	2.5μm layers	1.5μm layers
Cabling Metal	30nm Cr/500nm Au	20nm Cr/ 400nm Au / 20nm Cr
Trace Layout	11 individually accessed traces, common middle layer ground.	Top and bottom electrodes of each beam shorted together near cantilever base. Traces are bottom embedded Pt layer. Common ground and 5 beam outputs.

Cabling	50μm wide traces, 1mm wide cable, 50μm wide trace separation. 3cm long, curved cable	10μm wide trades, 100μm separation. 1.2mm wide and 4.5cm long straight cable.
Bonding	Not needed	Bump bonding or conductive epoxies.
Head Mount	0.8 by 1cm, roughened edges for glue adhesion.	0.8 by 0.8cm, smooth edges. Electrodes ordered to match Pfingst lab output configuration.
Advantages	Bonding challenges avoided. Individual electrode access. Thicker AlN has higher d_{31} and lower $\tan(\delta)$ values. Larger beam surface area means better current injection.	Easier processing. Higher probe yield per wafer. Lower trace capacitance because of embedded probe traces and thinner cable traces.

Table 2.1: A comparison between the monolithic first generation CIAO device design and the second generation design that separated the fabrication of the probes and cabling into two separate processes.

CHAPTER III

Modeling

In this chapter we present the effects of fluid loading and viscosity on the resonance response of one of the cantilevers developed by Littrell [70]. While Littrell focused on the response of the sensors in air, his cantilever design is well suited for applications in denser fluids, such as water because it contains no back cavity, can easily be coated to be made water resistant, and is more linear than capacitive sensor designs.

In order to describe the frequency response behavior of a cantilever in viscous fluid, a modified hydrodynamic forcing function is added to the Euler-Bernoulli beam equation. The modified equation is used to determine sensing and actuation responses of the cantilevers in water and other viscous fluids. A discussion is presented on the differences in the plane strain and plane stress conditions; the plane strain condition is a better fit for the wide cantilevers used in the CIAO device. *In vitro* measurements of the CIAO device in air and water are presented, demonstrating the CIAO device functionality as a transducer.

3.1 Theory of Cantilever Beams

The piezoelectric coupling equations are given by

$$[\varepsilon] = \mathbf{s}^E[\sigma] + \mathbf{d}^t[E] \tag{3.1}$$

$$[D] = \mathbf{d}[\sigma] + \boldsymbol{\epsilon}_\sigma[E]. \tag{3.2}$$

In the above equations, ε, $\mathbf{s}^E$, and σ denote strain, compliance, and stress, respectively [81]. The stress tensor, in these equations, is represented as a vector. D, d, E, and ϵ_σ are the electric charge density, piezoelectric constant, electric field, and permittivity under a constant stress, respectively. Square brackets denote a column vector and bold font denotes a matrix. In the case of a long, narrow, thin cantilever, σ_{yy} and σ_{zz} are set equal to 0, which is the plane stress case. For these conditions, the beam is considered to have a sufficiently narrow width that the stress free conditions along the sides of the cantilever apply through the width of the cantilever: that σ_{yy} is 0. However, this assumption fails for beams that are wide, as in the case of the CIAO device cantilevers. Therefore, a plane strain assumption should be used instead: $\epsilon_{yy} = \epsilon_{zz} = 0$, but $\sigma_{yy} \neq 0$.

3.1.1 Plane Stress Modeling

The equations for plane stress piezoelectric cantilevers are fully developed in Littrell, 2012 [71]. For convenience, the notable equations are recreated in this section. For a cantilever which is fixed at x=0 and vibrating in the x-z plane is considered, with plane stress assumptions, Equations 3.1 and 3.2 reduce to

$$\varepsilon_{11} = s_{11}\sigma_{11} + d_{31}E_3 \tag{3.3}$$

$$D_3 = d_{31}\frac{\varepsilon_{11}}{s_{11}} + \epsilon_{33}E_3. \tag{3.4}$$

For this notation, the subscripts 1,2, and 3 were used to denote x, y, and z, respectively. For more information, the application of these equations to piezoelectric beams discussed in detail in Reference [82].

Combining Equations 3.3 and 3.4 produces

$$\sigma_{11} = \overline{Y}(\varepsilon_{11} - \bar{\varepsilon}_{11}) \tag{3.5}$$

In Equation 3.5 $\bar{\varepsilon}_{11}$ denotes the eigenstrain formed in a piezoelectric layer subject to an electric field in the z-direction. The modified elastic modulus $\bar{Y}$ is given by

$$\overline{Y} = \left(\frac{1}{s_{11}}\right)\left(1 + \frac{d_{31}^2}{\eta_{33}s_{11} - d_{31}^2}\right). \tag{3.6}$$

For a more detailed consideration of Equations (3.3-3.6), see Krommer and Irschik [82].

The bending stiffness of a multimorph piezoelectric beam without the assumption of SPC is given by [70]:

$$\overline{YI} = b(x) \sum_{n=1}^{N} \frac{1}{s_{11n}} \left[\frac{1}{3}Z_{Cn} + \frac{1}{12}\frac{d_{31n}^2}{\eta_n s_{11n} - d_{31n}^2}h_n^3\right], \tag{3.7}$$

where $Z_{Cn} = (z_n - \zeta)^3 - (z_{n-1} - \zeta)^3$, $Z_{Qn} = (z_n - \zeta)^2 - (z_{n-1} - \zeta)^2$, and $h_n = z_n - z_{n-1}$. The summation extends over the N layers of the multimorph beam. The symbol ζ denotes the neutral axis in the absence of piezoelectricity, and is given by:

$$\zeta = \frac{\displaystyle\sum_{n=1}^{N} \frac{1}{s_{11n}}(z_n^2 - z_{n-1}^2)}{2\displaystyle\sum_{n=1}^{N} \frac{h_n}{s_{11n}}} \tag{3.8}$$

The bending moment of a piezoelectric multimorph beam is given by

$$M = -w_{,xx} \overline{YI} - \overline{MV} \tag{3.9}$$

where $\overline{MV}$ is given by

$$\overline{MV} = \frac{1}{2} \sum_{n=1}^{N} \frac{1}{s_{11n}} \frac{d_{31n}V_n}{h_n} Z_{Qn}. \tag{3.10}$$

In Equation 3.10, V_n can be prescribed, as for the case of actuation. For sensing applications, V_n is given by

$$V_n = -\frac{1}{L} \frac{\partial w}{\partial x}\bigg|_{x=L} \Lambda_n \tag{3.11}$$

where w is the deflection, L is the length, and Λ_n for the is given by:

$$\Lambda_n = \frac{E_n}{2} \left[\frac{Z_{Qn} \left(\sum_{i=1}^{N} \frac{h_i}{s_i} - \sum_{i \neq n} \frac{d_{31i}}{s_i} E_i h_i \right) - h_n \sum_{i=n} \frac{d_{31i}}{s_i} E_i Z_{Qi}}{\sum_{i=1}^{N} \left(\frac{h_i}{s_i} - \frac{d_{31i}}{s_i} E_i h_i \right)} \right]. \tag{3.12}$$

All cantilevers modeled in this chapter are fixed at the base with a piezoelectrically induced moment at the cantilever tip (unless small piezoelectric coupling applies, as described below), described by the following boundary conditions:

$$w(x)|_{x=0} = \frac{\partial w}{\partial x}\bigg|_{x=0} = 0 \tag{3.13}$$

$$\frac{\partial^2 w}{\partial x^2}\bigg|_{x=L} = \frac{\partial^3 w}{\partial x^3}\bigg|_{x=L} = \overline{MV}. \tag{3.14}$$

3.1.2 Plane Strain Model

Unlike the case of plane stress, the plane strain constitutive relations are formed using the conditions that $\sigma_{zz} = 0$, that $\sigma_{yy} \neq 0$, and that $\epsilon_{yy} = \epsilon_{zz} = 0$. The

49

implications of this change in relations is that the piezoelectric constitutive equations change to

$$\epsilon_{11} = s_{11}\sigma_{11} + s_{12}\sigma_{22} + d_{31}E_3, \tag{3.15}$$

$$D_3 = d_{31}\sigma_{11} + d_{32=31}\sigma_{22} + \eta_{33}E_3, \tag{3.16}$$

and

$$0 = \epsilon_{22} = s_{21}\sigma_{11} + s_{22}\sigma_{22} + d_{32=31}E_3. \tag{3.17}$$

The notation $d_{32=31}$ denotes that $d_{31} = d_{32}$, and that henceforth d_{31} will be used. As in the previous section, $d_{31}, \eta_{33}, \sigma, \epsilon, D_3$, and E_3 refer to the film piezoelectric coefficient, permittivity, stress, strain, electric displacement, and electric field tensor components. For an isotropic material $s_{21} = s_{12} = -\nu s_{11}$, and $s_{11} = s_{22} = \frac{1}{Y}$, where Y is the Young's Modulus. Substituting Equations 3.16 and 3.17 into Equation 3.15 yields

$$\epsilon_{11} = (1 - \nu^2)s_{11}\sigma_{11} + (1 + \nu)d_{31}E_3, \tag{3.18}$$

and

$$D_3 = d_{31}(1 + \nu)\sigma_{11} - d_{31}^2 E_3\frac{1}{s_{11}} + \eta_{33}E_3. \tag{3.19}$$

When Equations 3.18 and 3.19 are solved for E_3 by eliminating σ_{11}, an equation for the electric field is generated:

$$E_3 = \left(\frac{1}{(1-\nu)\eta_{33} - 2\frac{d_{31}^2}{s_{11}}}\right)\left[(1-\nu)D_3 - \epsilon_{11}\frac{d_{31}}{s_{11}}\right] \tag{3.20}$$

Plugging Equation 3.20 into Equation 3.18 and solving for the stress yields

$$\sigma_{11} = \frac{\epsilon_{11}}{(1-\nu^2)s_{11}} - \frac{d_{31}E_3}{(1-\nu)s_{11}}. \tag{3.21}$$

For vibrations in plane flexural beams, the moment is given by

$$M = b \int z\sigma_{11}dz \tag{3.22}$$

and the strain relation is

$$\epsilon_{11} = u_{,x} - zw_{,zz}. \tag{3.23}$$

Substituting Equations 3.21 and 3.22 into Equation 3.23 results in:

$$M = b \int \left(\frac{1}{(1-\nu^2)s_{11}} \right) \left[1 + (1+\nu) \left(\frac{1}{(1-\nu)\eta_{33} - 2\left(\frac{d_{31}^2}{s_{11}}\right)} \right) \left(\frac{d_{31}^2}{s_{11}} \right) \right] [u_{,x} - zw_{,zz}]z$$

$$- \left(\frac{1}{(1-\nu)\eta_{33} - 2\left(\frac{d_{31}^2}{s_{11}}\right)} \frac{d_{31}D_3}{s_{11}} \right) zdz. \tag{3.24}$$

Separating Equation 3.24 into the form of

$$M = -w_{,xx}\overline{YI} - \overline{MV}. \tag{3.25}$$

results in a bending modulus for the plane strain condition of

$$\overline{YI} = b \int \left(\frac{z^2}{s_{11}} \frac{1}{1-\nu^2} \right) + \left[(1+\nu) \left(\frac{d_{31}^2}{(1-\nu)\eta_{33}s_{11} - 2d_{31}^2} \right) \left(\frac{z^2}{s_{11}} \right) \right] dz. \tag{3.26}$$

Rewriting this into the form for multimorph beams produces the equation

$$\overline{YI} = b \sum_{n=1}^{N} \left(\frac{1}{s_{11n}} \frac{1}{(1-\nu_n^2)} \right) \left[\frac{1}{3}Z_{Cn} + \frac{1}{12} \frac{(1+\nu_n)d_{31}^2}{(1-\nu_n)\eta_n s_{11n} - 2d_{31n}^2} h_n^3 \right]. \tag{3.27}$$

3.1.3   Small Piezoelectric Coupling

Under the conditions of small piezoelectric coupling (SPC), several assumptions are made:

1. The $\frac{1}{12}\frac{d_{31n}^2}{\eta_n s_{11n} - d_{31n}^2}h_n^3$ term of $\overline{YI}$, given in Equation 3.7, is small compared to Z_{Cn}. The modified bending stiffness $\overline{YI}$ becomes that of a multimorph non-piezoelectric beam. This is given by:

$$\overline{YI} \to YI = b(x)\sum_{n=1}^{N}\frac{1}{s_{11n}}\left(\frac{1}{3}Z_{Cn}\right). \tag{3.28}$$

2. The case of SPC also assumes that the internal moment $\overline{MV}$ produced by the piezoelectric material in response to a material strain for the case of an applied pressure or mechanical load is negligible. The $\overline{MV}$ term is dropped, and

$$M \to M = -w_{,xx}\,YI \tag{3.29}$$

In the case of AlN films, SPC conditions are always met [70].

The resulting bending modulus for plane stress is given by

$$\overline{YI} = \frac{b}{3}\sum_{n=1}^{N}\frac{Z_{Cn}}{s_{11n}}. \tag{3.30}$$

and for plane strain is given by

$$\overline{YI} = \frac{b}{3}\sum_{n=1}^{N}\frac{Z_{Cn}}{s_{11n}(1 - \nu_n^2)}. \tag{3.31}$$

3.2 Beams Vibrating in Viscous Fluids

The frequency response of cantilevers vibrating in a viscous fluid is well studied for cantilevers that have circular or ellipsoidal cross-sections [83, 84, 85]. However, these models are limited to beams that have thicknesses and widths that are comparable, such that the cantilever can be approximated by a cylinder. This assumption breaks down when the width of the beam is significantly greater than the thickness of the

beams. In order to predict the frequency response of wide, thin beams, authors have employed various techniques [86, 87, 88]. The most complete work is by Sader [86], who derived an analytical technique for solving the responses of vibrating beams in viscous fluids using an elliptical cross-section equation with a frequency dependent modifier (Γ) to modify the effective cross-section of the beam in the hydrodynamic forcing term. Here we expand on the work done by Sader to include an elastic modulus term that describes a multimorph cantilever under plane strain response.

When characterizing a vibrating beam in a viscous fluid, the Euler-Bernoulli equation must be modified to include a hydrodynamic forcing term. This term, in the frequency domain, is defined as

$$F_{hydro} = \frac{\pi}{4}\rho\omega^2 b^2 \Gamma(\omega) W(x|\omega).$$
(3.32)

$\Gamma(\omega)$, used in Equation 3.32, is defined in [86], and modifies the hydrodynamic forcing term to describe rectangular cross-sectional beam profiles. D represents the effective cross-sectional area of the beam; in Sader this is given by $\frac{b^2}{4}$. However, experimental testing presented later in this chapter shows that using this area significantly overestimates the amount of fluid mass. $\Gamma(\omega)$ is a function of the fluid density and Reynold's number, defined as $\frac{\rho\omega D}{\eta}$, where ρ and η are the density and dynamic viscosity of the fluid, respectively, and b is the beam width.

With the addition of the hydrodynamic forcing function, the non-dimensionalized Euler-Bernoulli equation is rewritten to be

$$\frac{d^4 W(x|\omega)}{dx^4} - \frac{\mu\omega^2 L^4}{YI}\left(1 + \frac{\pi\rho D}{\mu}\Gamma(\omega)\right)W(x|\omega) = F_{mech}(x|\omega)\frac{L^4}{YI}$$
(3.33)

in the frequency domain. In this equation ω is the frequency of the driving force, ρ is the fluid density, and μ is the mass per unit length of the cantilever. Equation 3.33 has been normalized, as are all subsequent equations in this section. $\Gamma = 1$ represents the inviscid solution [86].

Equation 3.33 can be modified to include empirically-defined structural damping, as is included in Longmire's work [87]. Longmire defines and measures a structural damping term with the form in the time domain:

$$f_{sd}(x,t) = -c_{sd}\frac{L^4}{YI}\frac{\partial w}{\partial t}. \tag{3.34}$$

Adding this back into Equation 3.33 yields:

$$\frac{d^4 W(x|\omega)}{dx^4} - \frac{L^4}{YI}\left(\mu\omega^2 - jc_{sd}\omega + \frac{\pi\rho b^2}{4\mu}\Gamma(\omega)\right)W(x|\omega) = F_{mech}(x|\omega)\frac{L^4}{YI}. \tag{3.35}$$

In general, the value of c_{sd} will vary based on the material properties. As discussed in [87], c_{sd} is given different values which correspond to beam resonances, and are empirically measured. This model also allows for c_{sd} to be a function of frequency, allowing for the effects of squeeze film damping [89] or other frequency-dependent damping features coming from irregularities in the fabrication [90] or piezoelectric shunting [91]. This term is neglected for the calculations in the rest of this thesis, but is noted here for its potential future use.

For modeling of the CIAO cantilevers, the bending modulus YI in Equation 3.33 is modified to include the bending modulus described in Equation 3.30 or 3.31; because the CIAO beams are wide the plane strain case is more accurate to the underlying cantilever physics.

Equation 3.35 can be generalized to the form

$$\frac{d^4 W(x|\omega)}{dx^4} - \beta^4 W(x|\omega) = \bar{s}(x|\omega), \tag{3.36}$$

where $\bar{s}(x|\omega)$ is a normalized forcing function and β is defined by

$$\beta = L\left(\frac{1}{YI}(\mu\omega^2 + \frac{\pi\rho b^2}{4\mu}\Gamma(\omega))\right)^{1/4}. \tag{3.37}$$

3.2.1 Sensing Response

In sensing configuration, Equation 3.35 can be solved either by the technique developed by Littrell [70, 71], which does not require SPC conditions, or with the Greens function solution to a fixed-free cantilever, which does. The Greens function that solves Equation 3.36 with fixed-free boundary conditions is given by [86]:

$$
G(x, x'|\omega) = \frac{1}{\gamma(\beta)}
\begin{cases}
[-\phi_1(\beta)\phi_2(\beta x) - \theta_2(\beta)\theta_2(\beta x)]\theta_1(\beta(x'-1)) \\
+[\phi_1(\beta)\theta_2(\beta x) - \theta_1(\beta)\phi_2(\beta x)]\phi_1(\beta(x'-1)) \\
\qquad\qquad\qquad\qquad \text{for } 0 \le x \le x' \le 1 \\
[-\phi_1(\beta)\phi_2(\beta x') - \theta_2(\beta)\theta_2(\beta x')]\theta_1(\beta(x-1)) \\
+[\phi_1(\beta)\theta_2(\beta x') - \theta_1(\beta)\phi_2(\beta x')]\phi_1(\beta(x-1)) \\
\qquad\qquad\qquad\qquad \text{for } 0 \le x' \le x \le 1.
\end{cases}
\tag{3.38}
$$

where the functions $\phi_{1,2}, \theta_{1,2}$, and γ are defined by

$$
\gamma(\beta) = \frac{1}{4\beta^3[1 + \cos\beta\cosh\beta]}
\tag{3.39}
$$

$$
\phi_1(s) = \cos(s) + \cosh(s)
\tag{3.40}
$$

$$
\phi_2(s) = \cos(s) - \cosh(s)
\tag{3.41}
$$

$$
\theta_1(s) = \sin(s) + \sinh(s)
\tag{3.42}
$$

$$
\theta_2(s) = \sin(s) - \sinh(s)
\tag{3.43}
$$

Both techniques produce equivalent solutions under SPC conditions. The Littrell solution is more precise when the small amount of piezoelectric coupling is considered, but assumes a uniform pressure distribution. The Greens function solution would need

to be modified to include SPC, but it does not assume a uniform pressure distribution. Both methods can incorporate changes to the β in their solutions, and can therefore be used to describe the resonance behavior in water.

3.2.2 Actuation Response

The actuation response of a piezoelectric cantilever is given by

$$w = \frac{\overline{MV}}{\overline{YI}\beta^2} \left[\frac{\sinh(\beta L) - \sin(\beta L)}{1 + \cos(\beta L)\cosh(\beta L)} (\sinh(\beta x) - \sin(\beta x)) \right. $$
$$\left. - \frac{\cosh(\beta L) + \cos(\beta L)}{1 + \cos(\beta L)\cosh(\beta L)} (\cosh(\beta x) - \cos(\beta x)) \right] \tag{3.44}$$

where $\overline{YI}$ and $\overline{MV}$ are defined in Equations 3.7 and 3.10, respectively. β is defined either for air or water damping, as discussed above.

3.2.3 Effects of Beam Geometry

A map of the expected first resonant frequencies for a matrix of beam lengths and widths was generated (using plane stress), in order to determine the beam lengths needed to produce the desired resonant frequencies of the beams in the CIAO device. Example maps for 1μm and 2.5μm thick AlN layers are shown in Figure 3.1. These maps demonstrate that for viscous fluids the beams width has an effect on the resonant frequency of the beam, because the hydrodynamic forcing function is proportional to b^2.

For a given resonant frequency, thicker piezoelectric layers require longer beams, allowing for larger electrode areas. The current induced in the perilymph is proportional to the surface area of the beams [7], therefore thicker, longer beams produce more current than thinner shorter beams, if the resonant frequency is held constant. This is the motivation for the use of wide, long, thick cantilevers in the CIAO device design. The relationship between beam length, thickness, and resonant frequency

56
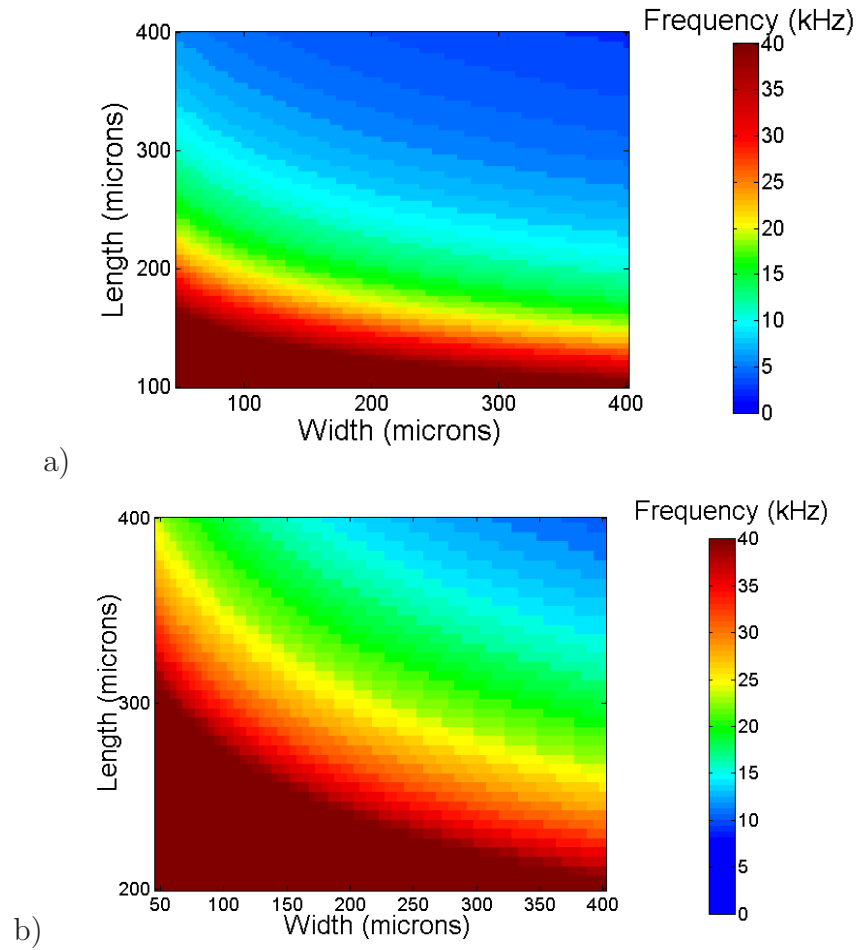
Figure 3.1: The resonant frequency of a piezoelectric bimorph, immersed in water, including viscous effects, as the length and width of the beam is varied. The thickness of the cantilever is fixed at 1μm (a) and 2.5μm (b).

57
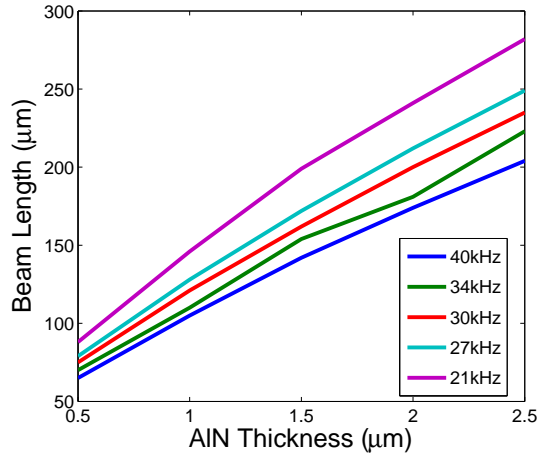
Figure 3.2: The variation in necessary beam length, for a given piezoelectric layer thickness, to achieve the desired resonant frequency in water. The beam widths are set at 400μm.

can be mapped differently, in order to facilitate device design. Figure 3.2 is designed to show the length needed to achieve a range of desired resonant frequencies, as a function of piezoelectric layer thickness. In this figure the width is set to 400μm, corresponding with pre-chosen beam widths for the CIAO device. The first generation CIAO prototype was designed using 2.5μm thick AlN layers (and the corresponding lengths shown in Figure 3.2). However, stress relieved 2.5μm thick AlN was very difficult to achieve on the AMS 2004 deposition tool and to etch and pattern because of added roughness and increased step heights. Therefore, the second generation CIAO prototype decreased the AlN layer thickness to 1.5μm, with correspondingly shorter beam lengths.

3.3   Predicted In Vivo Device Response

3.3.1   Electrodes in Ionic Fluids

The efficacy of the electrode-perilymph interaction is an important part of determining the current that is produced in the perilymph surrounding the implant.

Electrical charge is carried by electrons at electrodes, whereas charge is carried by ions in the surrounding fluid. The resulting charge transfer between an electrode and an ionized fluid is controlled by Faradic reactions [14].

A model describing the interface between an electrode and an ionized fluid was developed by Weiland, et al. [77], and is shown in Figure 3.3. In this figure, R_s denotes the resistance of the perilymph, C_{dl} denotes the capacitive double layer between the IrO ions, R_{ct} is the resistance of the charge transfer reaction, and C_s is the capacitance from the charging of the electrode. The constant phase element is added by Weiland to represent the electrode impedance. Together, C_{dl}, R_{ct}, CPE, and C_s can be clustered into an impedance term Z_p, which represents the overall impedance of the electrode [64].

3.3.2 Electrode Size

Smaller electrodes have more efficient current injection, such that four smaller electrodes would inject more current into an ionic fluid than a larger electrode of the same surface area [92] if driven by the same voltage. However, one single larger electrode will inject more current than one smaller electrode, as it sees a lower impedance than smaller electrodes. The effective impedance of the electrode-fluid system also is a function of frequency [92]. For electrodes of comparable material (Pt) and size (200μm) in the CIAO operation range, the impedance is 3-5kΩ.

3.3.3 Simple In Vivo Device Output Model

The electrode impedance Z_p can be characterized by an equivalent resistance R_p and capacitance C_p in parallel. Tykocinski measures the values for R_p and C_p in humans, and develops a model to predict the resistance and capacitance values as a function of the electrode area [7]. In this model the electrode is approximated as a sphere that is surrounded in a fluid and then bone. Using this model, and the
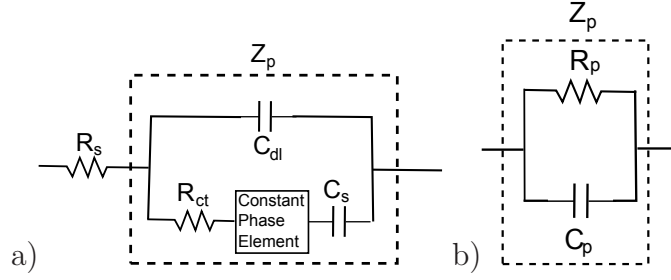
Figure 3.3: Electrical diagram of the IrO electrode - cochlear fluid system. Figure a) shows the expanded schematic, which includes components for each chemical reaction, while Figure b) shows the reduction of Z_p to a representative resistance (R_p) and capacitance (C_p).

Component	Governing Equation	Modeled Value	*In vivo* measured values
R_s	$\dfrac{1814\Omega mm}{\sqrt{A_e}}$	2267 Ω	2250 Ω
R_p	$\dfrac{1350\Omega mm^2}{A_e}$	2109 Ω	900 Ω
C_p	$17.667\dfrac{nF}{mm^2}*A_e$	11.3nF	6.5nF

Table 3.1: Extension of the Tykocinski model [7] for determining the approximate values for R_s, R_p, and C_p for electrodes of a given area A_e(in mm^2). Modeled area assumed to be 0.64mm^2, matching the *in vivo* area of the four functioning CIAO beams of the second implant.

fact that the resulting impedance relations Tykocinski derives do not depend on the duct size, the equations were extrapolated to apply to our project geometries and determined the perilymph resistance R_s and the electrode resistance and capacitance R_p and C_p, as a function of electrode area. These functions are shown in Table 3.1, as well as their approximate values for an electrode that is 400μm wide and 200μm long. In the case of all of the outer electrodes being shorted together the resistances would be reduced and the capacitance would be proportionally increased.

In his thesis [70], Littrell derives the voltage developed over a layer in a deflected piezoelectric beam in open source configuration, with the assumption of small piezo-
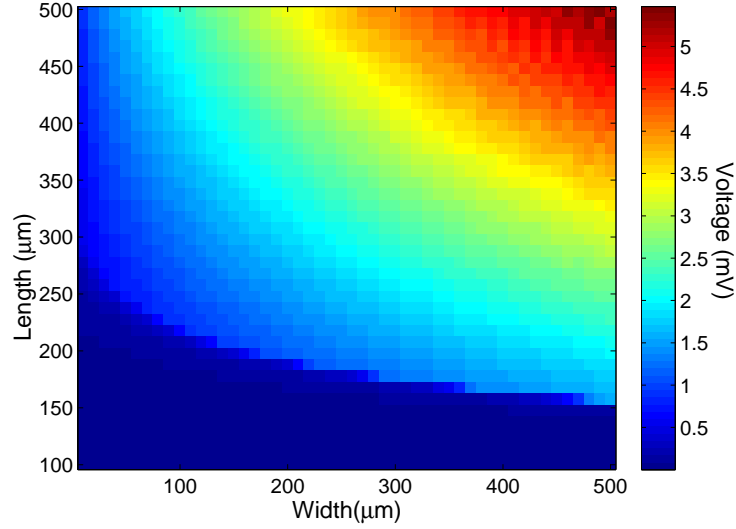
Figure 3.4: The open circuit voltage output of a piezoelectric beam, in water and at resonance, as its length and width are varied.

electric coupling, given in Equations 3.11 and 3.12. When the conditions for SPC are satisfied this reduces to:

$$V_n = - \left(\frac{PbL^2}{6YI} \right) \left(\frac{d_{31n}Z_{Qn}}{2\epsilon_n s_n} \right) \tag{3.45}$$

A map of this output voltage, as a function of cantilever length and width, is shown in Figure 3.4.

A full model of the CIAO device in the cochlea is shown in Figure 3.5. This figure includes both the impedance model for the CIAO device (purple) and the model for the electrode/cochlear fluid system (blue). Estimated values for R_s, R_p, and C_p that were derived from Tykocinski are given in Table 3.1, though *in vivo* testing indicated that the overall impedance of the fluid system can be approximated as a 5kΩ impedance (this value lowers to approximately 3kΩ at the CIAO operation frequencies). The CIAO cantilever impedances were measured to be C_{piezo}=40pF and R_{piezo}=1MΩ; when these are combined in parallel this impedance is over 100kΩ
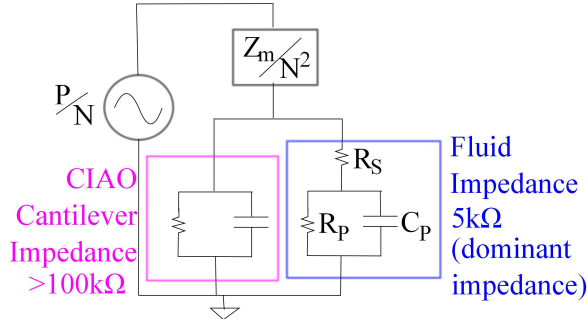
Figure 3.5: Representative circuit of the CIAO device operating in the cochlea.

for CIAO operational frequencies, therefore the fluid impedance always dominates. The model used in Figure 3.5 uses a pressure input (P, in Pa) and the mechanical impedance of the CIAO cantilevers, written as Z_m. The piezoelectric coupling factor, N, is used to convert the mechanical elements of the model into the electrical domain. The acoustic impedance can be decomposed into C_m and M_m, where the acoustic compliance is given by

$$C_m = \frac{b^2 L^5}{20 \overline{YI}} \tag{3.46}$$

and the acoustic mass term can be approximated for water by using the equation

$$\omega_{water} = \sqrt{\frac{1}{C_m M_m}}. \tag{3.47}$$

The turns ratio is given by

$$N = \frac{-10}{3} \frac{e_{31}}{h_{piezo} L^2} Z_{Q,piezo}. \tag{3.48}$$

Table 3.2 shows a summary of the values of C_m, M_m, Z_m and N for two CIAO cantilevers of 150 and 200μm lengths. As can be seen from the table, the mechanical impedance is significantly smaller than the impedance of the cochlear fluid. Because these are in series, the current injected into the cochlear fluid can be approximated

Component	150μm length	200μm length
$\overline{YI}$ (N·m^2)	3×10^{-10}	3×10^{-10}
C_m (m^5/N)	2×10^{-18}	8.5×10^{-18}
$M_{m,vacuum}$ (kg/m^4)	4.1×10^5	3.1×10^5
$M_{m,water}$ (kg/m^4)	9.3×10^6	7.1×10^6
$|Z_{m,water}|$ (kg/s·m^4)	1.1×10^{10}	1.1×10^9
N	139	78
$I_{cochlea,\text{6.3Pa input}}$ (μA)	0.8	0.4

Table 3.2: Modeled values for the mechanical impedance and turns ratio for a CIAO cantilever of length 150μm and 200μm (the range of the CIAO device lengths), operating at resonance. R_f is modeled at 3kΩ for the $I_{cochlea}$ calculation.

by the relationship

$$I_{cochlea} = \frac{p_{input}}{NR_f} \tag{3.49}$$

Expected currents from the device at 6.3Pa of differential pressure (corresponding to 110dB$_{SPL}$ of differential pressure across the cantilever) range from 0.4 to 0.8 μA for current beam geometries. Bhatti, et al. [63] measured auditory thresholds in the guinea pig require approximately 50(monophasic)-250(biphasic)μA. While this threshold was originally designed for, later testing using high frequency sinusoidal eABR stimulation revealed that a threshold of 600μA-1mA might actually be needed, depending on the health of the nerves of the deafened animal. This model indicates that auditory responses could be evoked, assuming a stimulation threshold of 150μA, with a differential pressure that is 171dB$_{SPL}$. Given that the maximum speaker output of the ABR system is approximately 110dB$_{SPL}$, an ABR could be evoked with the following conditions:

- At least 60dB$_{SPL}$ of amplification to the CIAO cantilever output.

- High integrity of the electrical connections to the CIAO device.

- Sufficient differential pressure in the cochlea to produce 110dB$_{SPL}$ of differential

63

pressure across the cantilevers (or less, if more amplification is used).

- Excellent nerve health, resulting in EABR thresholds of 150μA.

- No fibrotic tissue growth, which would dampen the mechanical motion of the cantilevers and increase the impedance at the electrodes.

Each of the above conditions are extremely difficult to meet in an *in vivo* situation, so realistically an ABR threshold could not be evoked using the passive CIAO device described in this thesis. This calculation indicates that future iterations of the CIAO device will need to use amplification. In this case, the amount of amplification will depend on whether the CIAO cantilevers are grounded in the center or externally. In the condition of a feedback loop where the outer cantilever electrodes are used as the stimulation electrodes the cantilever impedance will be the 3kΩ cochlear fluid impedance, but if separate stimulation electrodes are used and the cantilevers have grounded outer electrodes, the net impedance across the cantilevers will be significantly higher. Future consideration of each of these mechanisms is needed, and will not be discussed in this thesis.

3.3.4 Power Flow Into the Cochlea

The power of a plane wave entering the human cochlea at a sound pressure of 110dB$_{SPL}$ is 3.84μW, assuming an ear canal with a 7mm diameter. This incident power encounters the input impedance of the middle ear, which is measured to be 20-40MΩ (N·s/m^3 units) [93]. Using the equation

$$\text{Power} = \frac{\text{Pressure}^2}{\text{Resistance}} \tag{3.50}$$

this means that the net power entering the middle ear is approximately 0.9-1.8μW of power. The transmission efficiency of power between the ear canal and the cochlea

Location	Power
Plane wave in ear canal	3.84μW
Ear drum	0.9-1.8 μW
Entrance to SV	200-300 nW
Power needed for ABR response	50μW
Amplification needed	46dB

Table 3.3: Input acoustic power, as compared with the necessary power needed to evoke an ABR response.

is approximately 10-20% [18], so the power that reaches the scala vestibuli is around 200-300nW of power.

For comparison, stimulation of the auditory nerves using the CIAO implant requires at least 100μA of current, with a resistance of 5kΩ; this corresponds to a minimum power of 50μW. To achieve this, a minimum of 46dB of amplification is required, indicating that acoustic energy alone is not sufficient to power the CIAO device; this is shown in Table 3.3.

3.4 In Vitro Experimental Methods

This section details the experimental techniques used in the characterization of the CIAO device. Devices were characterized in air and water prior to *in vivo* implantation; the primary method of characterization was to measure the deflection of actuated cantilevers using a laser vibrometer. The laser vibrometer is able to measure sub-nanometer deflections at frequencies as high as 1.5MHz, allowing for highly precise measurements of the cantilever movements. The experimental techniques used to measure the sensing response of the CIAO devices is also discussed. Sensing measurements require a calibrated transducer and reference hydrophone or microphone; the calibration techniques are presented in this section. Squeeze film damping can

also affect the resonant behavior of resonating cantilevers in fluids, but is not a factor for the particular geometry used for the CIAO device testing.

3.4.1   Air Testing Procedure

Actuation measurements are performed using a linear 1 second long sweep/chirp signal with a fixed voltage magnitude generated by LabView. The signal is applied to the middle electrodes of the device, which are shorted together. Ground is applied to the outer electrodes, which are all shorted together but are not electrically connected to the middle electrodes of the cantilevers. Cantilever velocity responses were measured using a laser vibrometer [Polytec (Tustin, CA) OFV-303 sensor head]. The magnitude and phase of the device response, as measured by the vibrometer, are compared with the magnitude and phase of the reference sweep signal.

The vibrometer and probe are positioned in such a way as to maximize the signal amplitude reflecting from the cantilever back to the vibrometer. The reflectivity of the metal, the cantilever curvature due to the resultant residual stress mismatch between the layers, and the difficulty in gripping the device to precisely control the 3D angling required for the vibrometer response all contribute to a large variance in the amplitude of the vibrometer signal that is returned back to the computer. Cantilevers were measured at their location of best reflectivity, but this did not always correspond to the locations of maximum amplitude of response. For this reason, comparisons of amplitude responses of cantilever arrays will have noticeable difference in the low frequency magnitude response magnitude for those cantilevers where proper reflectivity was not achieved near the tip. In order to eliminate this effect, a more precise positioning and optics system is necessary.

All air measurements presented in this chapter were performed using cantilever actuation. Testing designed to measure the sensing resonant frequency response of the

cantilevers in air would require a calibrated speaker that is capable of operating in the 100kHz-150kHz range.

3.5 Water Testing Procedure

3.5.1 Actuated Measurements

CIAO actuated response testing in water is performed in the method described above for air actuated testing, but the probe is also submerged in a small container of water. For the tests described in this chapter the water was neither deionized nor deaerated. An epoxy was applied around the electrical connects at the base of the probe to prevent the device from shorting out in the water. The probes are mounted on glass slides, such that the cantilevers are approximately 0.5mm from the underlying glass slide. The container is filled with water to a height of at least 3mm higher than the top of the cantilevers, and the laser is shone down vertically onto the cantilevers to measure the cantilever actuated response. All measurements were performed at room temperature.

Actuated measurements were also performed using a pure silicone oil with a 20cSt viscosity, which is 20 times the kinematic viscosity of water. A sweep signal was applied to the cantilever and the velocity was recorded using the laser vibrometer using the same technique that is detailed for measuring the actuation response of a CIAO device in water.

3.5.2 Water Sensing Measurements

Measurement of the probe response to acoustic stimulation is first performed using an underwater transmitter [Reson 4013] and the laser vibrometer. The laser vibrometer is positioned at the tip of one of the cantilevers, and the transmitter is positioned 2cm from the cantilever. Both the probe and the transmitter are submerged in water.
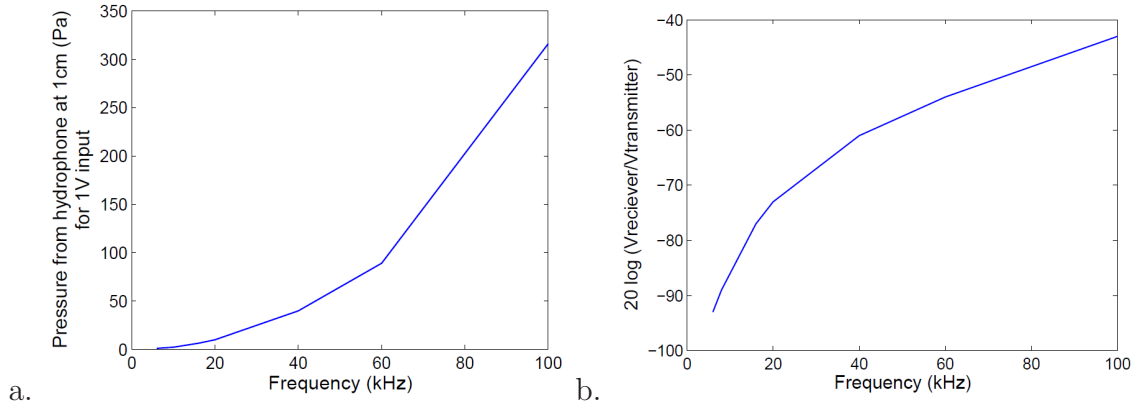
Figure 3.6: (a) The pressure output from the Reson 4013, functioning as an underwater transmitter, for a 1V input signal, calculated at a distance of 1cm from the transmitter. (b) The 4013 transmitter-hydrophone transfer function. This figure is generated using the calibration information for the 4013 transducers, and shows the ratio of the receiver voltage output for a 1V applied signal to the transmitter, at a distance of 1cm, in an ideal environment. This is extrapolated from 1m data, and does not take into account the effects of the geometry of the hydrophone.

A chirp is played through the underwater transmitter, and the output of the vibrometer measurement of the cantilever velocity is compared with the signal sent to the transmitter.

The output of the CIAO device can also be measured directly, rather than by using a vibrometer. The low frequency sensitivity from the CIAO cantilevers was modeled to be 113μV/Pa using the model described above, but this was not experimentally confirmed. This is a relatively low sensitivity, so sensing tests are improved through the use of either a loud pressure source or amplification. When the CIAO was amplified, an AD621 instrumentation amplifier was used, set to a constant gain of 100. This instrumentation amplifier is low noise and has a constant gain across the entire range of measurement frequencies.
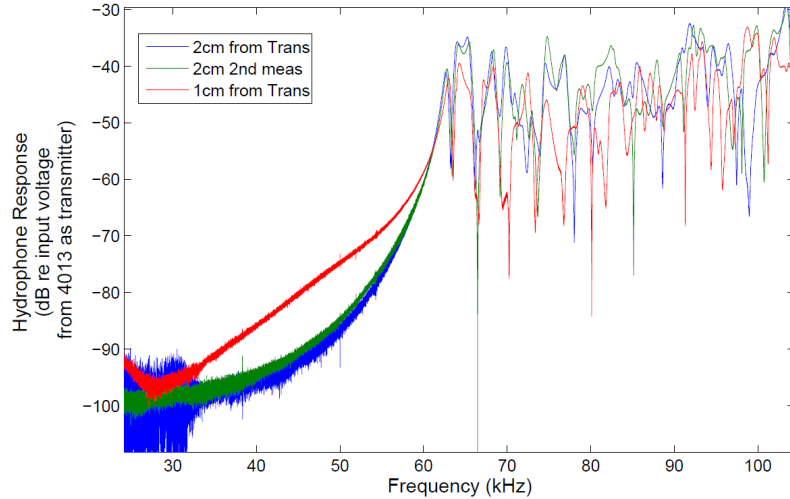
Figure 3.7: The measured input from the Reson 4013 receiver, using a second 4013 as an underwater transmitter for the water container used for hydrophone experiments. The measurements are referenced against the output signal to the transmitter.

3.5.3 Underwater Transmitter/Hydrophone Characterization

A Reson 4013 hydrophone was used as an underwater transmitter for the purposes of measuring the sensing response of the cantilever array in water using the laser vibrometer. As a transmitter, the Reson 4013 outputs between 10 and 40Pa of pressure in the 20-40kHz range when a 1V signal is input, but only when it is 1cm from the probe (Figure 3.6a). Additionally, the calibrated sensitivity of the 4013s as both transmitters and receivers at 1m is known; when this is extrapolated to a 1cm distance the idealized transfer function between the pair can be calculated, which is shown in Figure 3.6b. Using this knowledge, the water container can therefore be characterized using the 4013 pair. The container box response is shown in Figure 3.7, measured with 2cm and 1cm separations between the 4013 pair. Free-field sensing calibration in water either requires very large chamber or time gating to eliminate signal reflections. For example, if the device and transmitter had at least 0.5m of distance from every surface (and assuming the reflections from the head of the trans-

mitter were negligibile and that the device was close to the transmitter), the travel time of the emitted pulse would be approximately 0.67ms, which is the maximum length of the output chirp. Shortening the chirp in this way, however, reduces the time window over which the noise gets averaged.

Alternately, a pressure calibration can be done in a small enough container such that the reflections and resonances are out of the range of measurement. An approximation of this method was performed by using a small container, because it allowed for a small footprint testing area and did not require devices that were submerged to large depths, which would have required changes to the wiring used to make the CIAO devices. Pressure field calibration was achieved with limited success: the chamber response did not show significant peaks or nulls in the desired 20-40kHz testing range (such as are seen above 60kHz in Figure 3.7), though there is a large change in transmitter sensitivity across that frequency range. Future pressure sensing tests will certainly require a more sophisticated measurement setup.

3.5.4   Squeeze Film Damping Considerations

The water frequency response testing is all done with the underside of the CIAO probe attached to a glass slide. Because the cantilevers are positioned 0.5mm from the bottom surface, the effects of squeeze film damping needs to be considered. Naik and Longmire [87] define a large gap in squeeze film damping to be gaps that are on the order of the cantilever width and larger. For this condition, the mass loading in the fluid dominates over the viscous damping by a ratio of

$$\frac{f_{viscous}}{f_{pressure}} \sim \frac{4\eta}{(b^3/h)\omega} \tag{3.51}$$

where η, b, and h are the kinematic viscosity, width, and height of the cantilever. For the CIAO device in water, this ratio equals 1.5×10^6, indicating that squeeze film

70

Freq (kHz)	δ_{air} (μm)	δ_{water}(μm)
1	70.7	17.8
5	31.6	8.0
10	22.3	5.6
20	15.8	4.0
50	10.0	2.5
100	7.1	1.8

Table 3.4: Boundary layer heights for an oscillating plane in air and water.

damping is not a consideration for this measurement.

Alternately, the boundary layer can be calculated for an oscillating plate, starting from the equation

$$u_{,t} = \eta u_{,yy}. \tag{3.52}$$

In this case the plate is along the x axis, and the vibration motion is in the y-axis direction. The solution form to this equation is

$$u(y,t) = e^{-i\omega t}(Ae^{i(1+i)y/\delta} + Be^{-i(1+i)y/\delta}) \tag{3.53}$$

where $\delta = \sqrt{\frac{2\eta}{\omega}}$, and describes the evanescent decay of the motion; this can be considered an approximation of the boundary layer. Table 3.4 shows values of δ for different frequencies, in air and water. Because the CIAO device operates at 20-40kHz, its boundary layer is under 5μm in both air and water.

3.6 In Vitro Results and Discussion

3.6.1 Air Actuated Response

A representative measurement of the magnitude and phase response of a CIAO probe in air is shown in Figure 3.8a. The resonances of each cantilever in air are

spaced between 90kHz and 160kHz; a closeup of these resonances are shown in Figure 3.8b. The air response of a CIAO cantilever, as measured by the laser vibrometer, is a flat frequency response in the low frequency ranges, followed by a sharp, high Q peak at the first resonance. The phase response is correspondingly flat, with a sharp π transition at resonance.

The model predictions of the cantilever response are matched to each cantilever, and show good accuracy through the first resonant peak. The mismatch of the model to the measured response in the frequencies higher than the first resonant frequency represent a discrepancy between the modeled location of measurement (distance along the length) and the measure location. This effect is particularly apparent in the high frequency response of beam 4 in Figure 3.8b (the beam is light blue), where the model diverges from the experimental magnitude after the first resonance. The model response has been accordingly normalized to match the low frequency sensitivity of the cantilever. A small amount of mechanical crosstalk is observed between the cantilevers, but this effect is small compared to the effect of current spread when the device is implanted.

3.6.2 Water Actuated Response

Figure 3.9 shows the water actuation response of the same probe as was used for the air actuation response in Figure 3.8. In this figure, the modeled device response, using plane strain conditions, is shown in the top plot. The second measured magnitude response is shown in the middle plot, and the measured phase response of the device is shown in the bottom plot. It is established [94] that the hydrodynamic function defined in Equation 3.35 was derived with the assumption that L is much greater than b. This formulation, used in Sader [86], assumes an infinitely long cantilever, such that the fluid approaching the cantilever flows around it, as it would a cantilever with a circular cross-section. However, in the case of cantilevers that satisfy b/L≅1
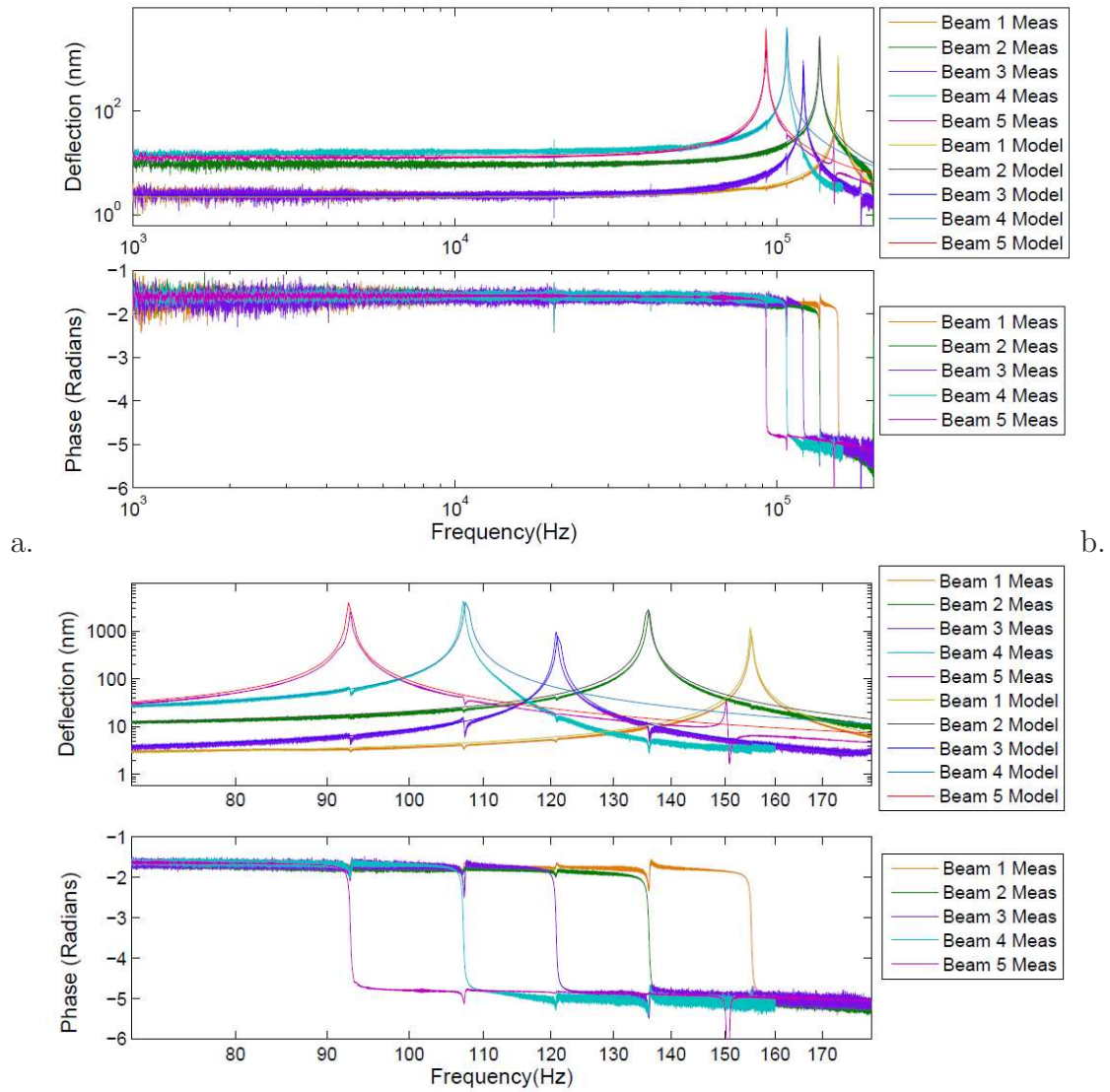
Figure 3.8: The magnitude and phase response of a fabricated CIAO device in air (a), and close-up of the resonant frequencies (b). Air resonance models are fitted to the magnitude responses, corrected to match each cantilevers low frequency response amplitude. All five cantilever outer electrodes were shorted together and to ground for this measurement, and a voltage was applied to a common middle electrode. Individual cantilever response is measured using a laser vibrometer.

73
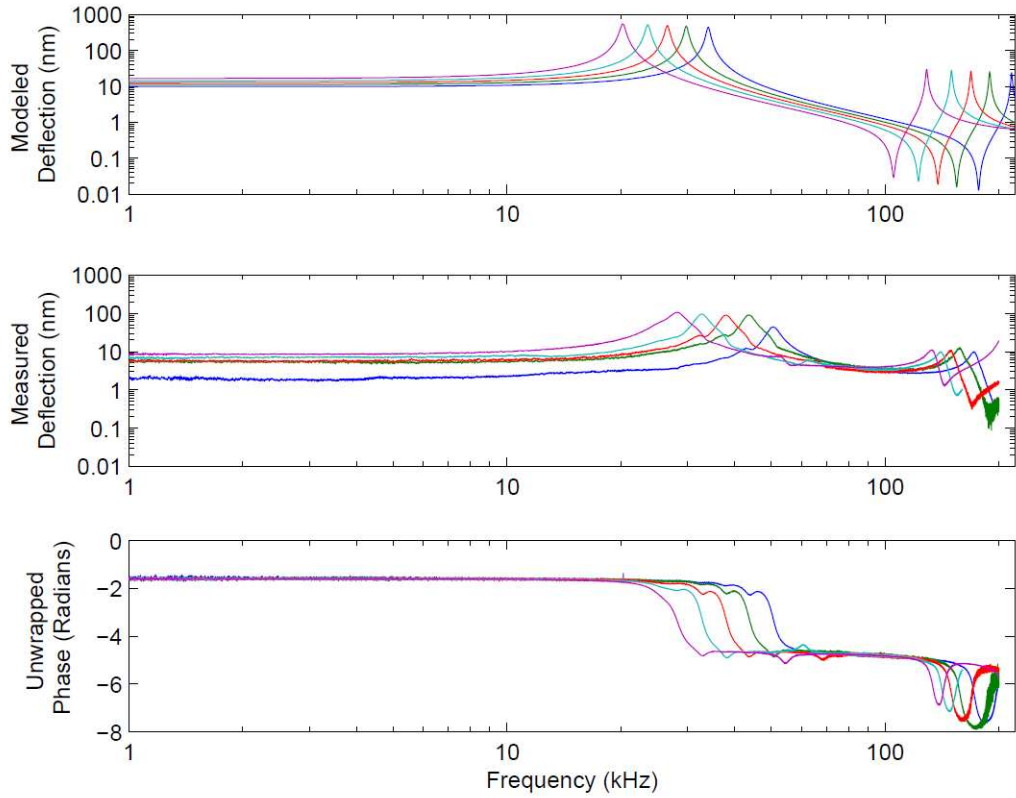
Figure 3.9: The modeled (plane strain, top plot) and measured magnitude (middle plot) and phase response (bottom plot) of the device in Figure 3.8 actuated in water, as measured with the laser vibrometer.

74

(such as the case of the CIAO cantilevers, where b/L$\cong$2), the dominant path of fluid flow is around the tip of the cantilever, rather than around the sides. This case is more similar to the case of an infinitely wide cantilever, which looks like a ledge to the incident flow. Using the Sader model for a wide beam, therefore, overestimates the amount of fluid moving in phase with the cantilever, as the mass loading is calculated as if the fluid is passing an infinitely long cylinder of width b.

This poor fit is demonstrated in Figure 3.9, where the resonant frequency predictions are off by 50%. The modeled and measured cantilever responses are shown in the top plot of Figure 3.10, demonstrating this poor fit. In an attempt to better approximate the response, the width used in the hydrodynamic forcing term is changed from b to $\sqrt{bL}$ in the lower plot of Figure 3.10. This approximation reflects that the dominant length term in the problem is no longer the width, but is intermediate between the length and width. As shown in Figure 3.10, this approximation holds well for the CIAO cantilever first resonances, though it is untested for other b/L ratios. In addition to the mismatch between the model predictions for resonant frequencies, there is also a discrepancy between the measured and predicted amount of damping of the first resonant peak. It is likely that part of the source of additional measured damping comes from poor cantilever definition during fabrication. As shown in Figure 3.11, there is a discrepancy between the defined edges for the AlN, which was patterned to match the edges of the DRIE, and the actual edge of the Si prescribed by the DRIE, due to an undercut during etching of approximately 20μm. The mismatch results in a longer cantilever whose length is prescribed by the edge of the Si, but also results in a cantilever that has two strips of AlN extending out from the sides of the cantilever. This overhang of AlN also mechanically couples each cantilever to the next; this coupling can either constructively or destructively couple [95]. Figure 3.12 shows a comparison of the measured high frequency actuation response of three cantilevers in water (solid lines), as compared with the model (dashed lines). The measured
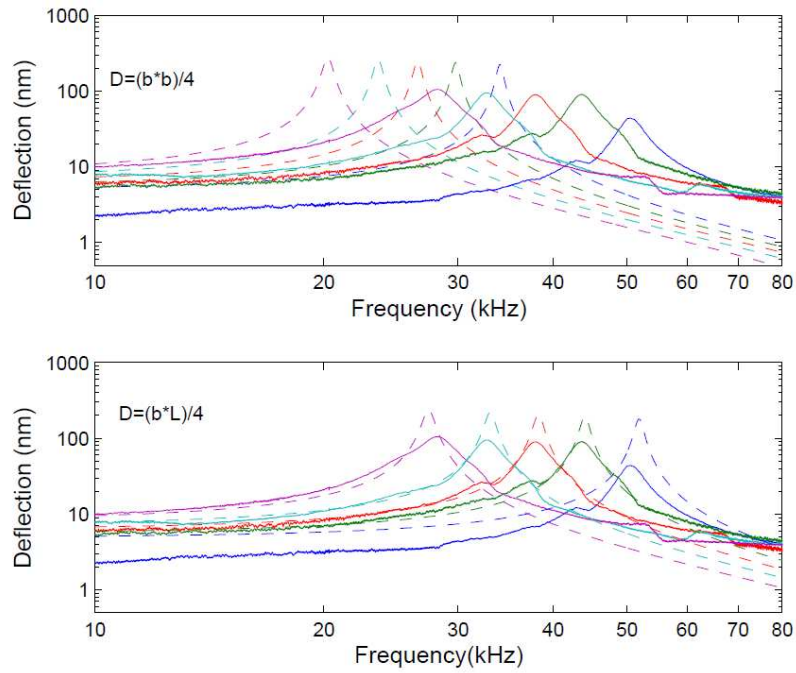
Figure 3.10: Comparison between the scaled cross-sectional area defined in Sader $(b^2/4)$ and the modified area $(bL/4)$ that was modified to reflect that the cantilever width was significantly bigger than its length. Measured data is presented in solid lines, and the modeled data is dashed. Model and measured data is color matched for each cantilever.
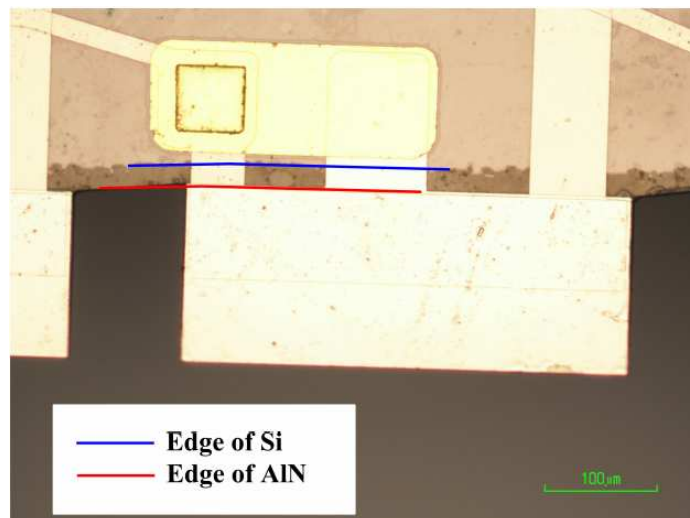
Figure 3.11: A close-up view of one cantilever. The silicon undercut the edge of the cantilever by approximately $20\mu m$, lengthening the resulting cantilever. The edge of the AlN was not undercut, however, so a thin strip of AlN remains extending from the sides of the base of the cantilever.

76
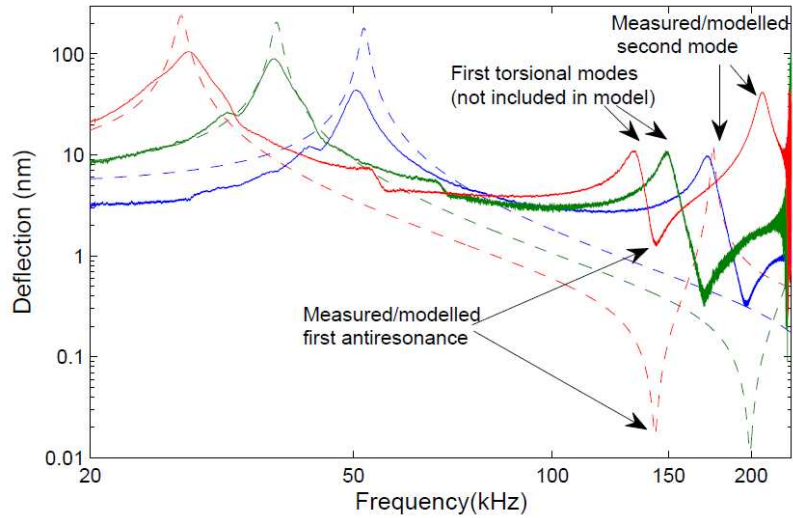
Figure 3.12: A comparison fitted model prediction (dashed lines) and measured response (solid lines) of the high frequency response of three cantilevers. The first antiresonance is shown, as well as the second mode resonance for the longest beam. The measured cantilever response includes a torsional mode that is not included in the model.

response shows the first resonance, first torsional mode, and first antiresonance of each cantilever. The second resonance of the longest cantilever (shown in red) was also low enough to be compared, as well. In general the model predicts that the first antiresonance will occur at higher frequencies than measured, though the frequency location of this minimum in response is highly dependent on the location along the length that is measured. Additionally, the torsional modes of the cantilevers are not included in the model, but are present in the measured signal, because the vibrometer was positioned near the centerline of the beam to minimize torsional responses, but often acceptable vibrometer reflection was only achieved closer to the sides of the cantilevers. Maximizing signal response was prioritized over the minimization of torsional modes.
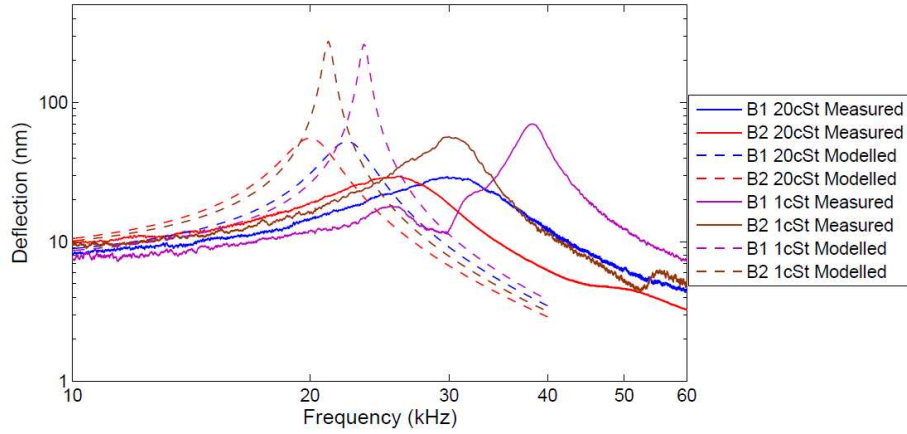
Figure 3.13: The measured (solid line) and fitted model (dashed line) frequency response of two cantilevers in water and a silicone oil with 20cSt viscosity.

3.6.3 Viscous Fluids Actuated Response

Viscous effects were explored by comparing silicone oil (kinematic viscosity of 20cSt) with water (1cSt). The resulting response of two cantilevers actuated in water and the silicone oil are presented in Figure 3.13, along with the predicted response using Equation 3.35. For the measured cantilevers the viscous fluid resonance was 15-22% lower than the water resonance. This difference was much less pronounced in the model (4-6% difference). Figure 3.13 demonstrates that Equation 3.35 overestimates the amount of mass loading on the cantilever but underestimates the amount of fluid damping; all measured resonances were more damped than the equivalent modeled response.

3.6.4 SPC in Water

The material properties of AlN satisfy the small piezoelectric coupling (SPC) conditions; this means that the resonant response of the cantilever should not depend on the electrical conditions of the cantilever. When acoustically driven, the cantilever should respond the same when shorted or electrically open.

This was tested for all five cantilevers of the same probe that was used for the air and

78

water tests discussed above (Figures 3.8 and 3.9). The cantilevers were actuated by a Reson 4013 underwater transmitter, and their deflection was measured using a laser vibrometer. The magnitude and phase of the shorted and open voltage responses of each cantilever are shown in Figure 3.14. The first, third, and fourth beams all operate as expected: there are measured resonant responses that match the actuated resonances, and these resonances are invariant between the short and open voltage conditions. However, the second and fifth beams have significant differences between the resonances of the two cases. These differences are apparent both in the phase and the magnitude responses. It is unclear what produced the differences, this needs further characterization in the future.

The sensing tests of Figure 3.14 also illuminate some of the repeatability challenges that are faced in acoustic sensing tests. The response of Beam 4 between 40-50kHz differs by up to 40dB in response magnitude, this is likely due to slight differences in the probe and vibrometer positioning relative to the water container during measurement.

3.6.5 Probe Sensing Response in Water and Saline

The measurement of the voltage response of the CIAO device is different from the vibrometer response because the CIAO response is the sum of all five beams, whereas the vibrometer measures a single beam response. Therefore, the phase response at each resonance is the sum of one beam in resonance combined with four that are not. The summed response of a CIAO device is shown in Figure 3.15; the vertical lines indicate the measured water resonances. Correct resonances are apparent for four of the five cantilevers, though the longest cantilever is slightly more damped than when previously measured. A container resonance occurs at 52kHz.
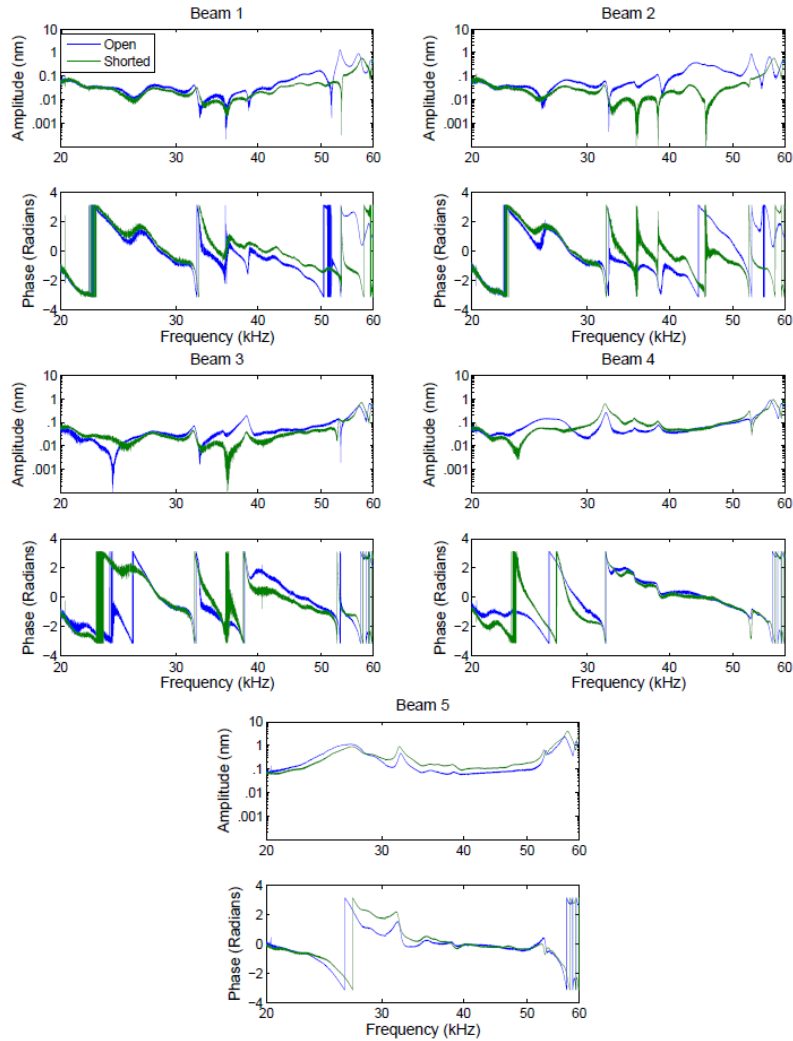
Figure 3.14: The open and short circuit CIAO cantilever deflection responses, measured using a vibrometer to sense the response of each cantilever. The same device was used as is shown in Figures 3.8 and 3.9. A hydrophone plays the chirp 2cm from the device, and a laser vibrometer was used to measure each cantilevers frequency response. Actuated responses of the device were measured at 51, 44, 38, 33, and 28kHz (beams 1-5, respectively).
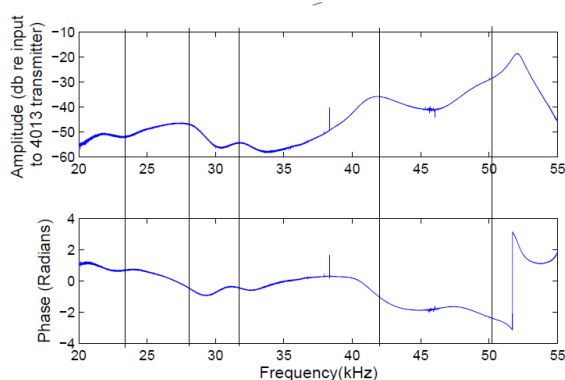
Figure 3.15: Measured probe output, amplified 40dB. Sound played by a 4013 transmitter 2cm away from probe. Lines represent the measured actuated resonant frequencies of the system underwater.

3.7 Device Noise

The input referred noise (IRN) for a CIAO cantilever that is open electrically is given by

$$IRN = v_n^2 \left(\frac{1}{S^2} \right) = \frac{4kTtan(\delta)}{\omega C} \left(\frac{1}{S^2} \right) \tag{3.54}$$

where k is the Boltzmann constant, T is the temperature in Kelvins, $tan(\delta)$ is the film dissipation factor, ω is the frequency, C is the capacitance, and S is the sensitivity of the CIAO device. The units of the IRN are given in $Pa^2/sqrtHz$. For the CIAO device the sensitivity is modeled to be $113\mu V/Pa$ at low frequencies. Figure 3.16 shows the modeled IRN for the CIAO device as a function of $Pa/\sqrt{Hz}$. The noise floor of the CIAO device has not been measured, though; this needs to be measured in the future. However, when the CIAO device is implanted in the cochlea, the dominant source of noise becomes the resistance of the fluid (this resistance, at CIAO operating frequencies, was measured to be between 2-3kΩ). In this electrical condition, created when the middle CIAO electrode is shorted to animal ground and the outer CIAO

81
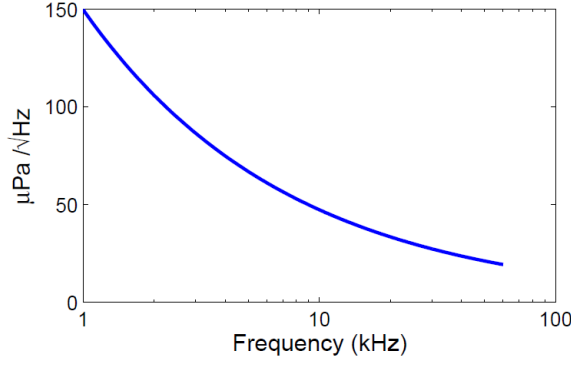
Figure 3.16: Input referred noise for the CIAO device.

electrodes are open to the cochlear fluid, the input referred noise becomes

$$IRN = v_n^2 \left(\frac{1}{S^2} \right) = 4kTR_f \left(\frac{1}{S^2} \right), \tag{3.55}$$

which corresponds to a voltage of $9\text{nV}/\sqrt{Hz}$ device response. For CIAO operating frequencies, and with the assumption of a $3\text{k}\Omega$ impedance across the CIAO device, this corresponds to a noise level of $0.98\mu\text{V}$ (20kHz) to $1.39\mu\text{V}$ (40kHz). This is higher than what was measured, (0.05-$0.08\mu\text{V}$ was measured), but is still a lower voltage than the maximum CIAO output, which was $2\mu\text{V}$. It is possible the discrepency between the prediction and the experimental value is due to the added resistance of the coaxial cabling that ran from the CIAO output to the lock-in amplifier; this resistance was in parallel to the CIAO device, which would reduce the net resistance (and therefore the net Johnson noise) that was recorded by the lock-in amplifier.

CHAPTER IV

AlN Characterization

With beneficial electrical properties, CMOS compatibility, and relative ease of fabrication, aluminum nitride (AlN) has become an increasingly preferred material for filtering, timing, and low noise sensing applications. AlN is widely used in radio frequency timing and filtering applications due to its ability to provide high quality factors and its high acoustic velocities [96, 97]; it also has successful applications as a sensor because of its low dissipation factor [71]. For these applications achieving a reliable deposition process that ensures films have high piezoelectric coefficients is both necessary and challenging.

This chapter presents the metrology techniques that are used to determine AlN quality. A discussion of the various factors that impact AlN stress and crystal quality are then discussed, with particular emphasis on the effect of AC target power because the effect of AC target power on AlN S-Gun sputtered films was not previously well characterized in the literature. Transmission electron microscopy (TEM) images of two AlN films deposited at two different powers are presented, demonstrating that the AlN films deposited at the University of Michigan generally have good orientation and stacking characteristics, but that the films have less optimal behavior at the top of the film that should be addressed. With these contributions, the stress and crystal quality of AlN deposited using an AMS 2004 S-gun sputter tool can better be pre-

dicted and fine tuned to provide consistent AlN films. Finally, a comparison of AlN wet etchants and masking materials for wet etches is provided, demonstrating that the KOH-based AZ400K developer is a suitable alternative to hot phosphoric acid etching, and in some circumstances AZ400K demonstrates preferable, more uniform etching characteristics.

4.1 AMS 2004 S-Gun Magnetron Sputter Tool

The AMS 2004 S-gun sputter tool consists of two concentrically arranged conical Al targets that effectively function as two separately controlled magnetrons, as each target has its own set of magnets. A 40kHz, 10kW AC power source is connected between the two targets, which alternate acting as anode and cathode [98]; in this design no additional anode is needed, as shown in Figure 4.1. Unlike the Tegal Endeavor AlN deposition tool, which has a similar concentric Al target configuration, the AMS 2004 does not have the capabilities to monitor deposition rate or any chamber temperature conditions, nor does it have a stress adjustment unit. Because stress control of AlN films deposited by this tool can only be achieved through variation of deposition parameters, a portion of the work covered in this thesis is dedicated to better understanding these controllable deposition parameters such as target power and gas flow.

4.2 Measurement of AlN Properties

The quality of deposited AlN is measured using a number of metrics. Initial film characterization, done during the fabrication process, includes measurement of the film thickness, nonuniformity, and stress. X-ray diffraction measurements of the AlN film crystal quality are also performed on the blanket AlN layers. Dissipation and capacitance measurements are also measured once AlN vias are etched, allowing for
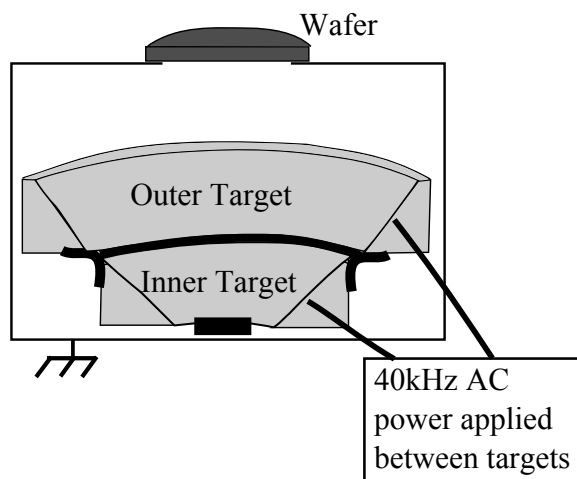
Figure 4.1: Cross-sectional view of the AMS 2004 S-gun magnetron AlN sputter tool. The S-gun sputtering technique uses two concentric Al targets with a 40kHz power applied between the targets. The wafer sits at the top of the chamber.

access to the lower electrode layers; these measurements quantify how lossy the film is and measure the trace capacitances. When the device is released the piezoelectric coefficient d_{31} is measured using a laser vibrometer. Each of these techniques is discussed below.

4.2.1 Thickness and Nonuniformity

Measurement of the film thickness and nonuniformity is very important, as the film thickness for each piezoelectric layer affects the resonant frequency of the cantilevers. Thickness and nonuniformity are measured using the NanoSpec 6100, using a 5 point scan that provides the AlN thickness, thickness standard deviation, and nonuniformity percentage. Each point fits a measured spectra of AlN on oxide to a spectra predicted using the optical properties of AlN and thermal oxide. Typical AlN nonuniformities are approximately 3-6% for films that are 1.5-2.5μm thick.

4.2.2 Stress

For this work, all stress measurements of AlN were performed using the Flexus 2320-S Thin Film Stress Measuring Apparatus. This tool operates by using one or both of two different wavelength lasers (670 nm and 785nm) to take a line measurement of local film curvature. Line measurements were taken at 0 and 90 degrees. When the tool is given wafer and film property information, and when the line measurements are taken before and after the film deposition, the Flexus computes an average radius of curvature for the wafer and uses this value to predict an average line stress for the film. However, the tool does not provide a standard deviation for these stress values, which oftentimes can be quite large for thin films, films with nonuniform thickness, or films that dont reflect either laser well.

A second method of evaluating stress utilized by the Flexus extrapolates a 3D stress map (using an unspecified algorithm), and outputs an average film stress and stress deviation. While this map is an extrapolation, it does have two advantages: it outputs the standard deviation, and it better represents the effects near the edges of the wafer by averaging across an area rather than a line. The Flexus stress measurement only allows a single input film thickness value, so the tool records a stress that overly tensile for the wafer center and is overly compressive for the wafer edge for AlN, which is thicker in the center than at the edges.

In short, both of these stress evaluations are limited. For publication and for this thesis the preferred method of recording stress is the average of the 0 and 90 degree line out stress measurements for the laser wavelength that produces a higher overall response intensity, as this is a more standard, less extrapolated measurement. Figure 4.2 demonstrates how a given film can have up to a 400MPa range of stress values, depending on which stress measurement technique and laser is chosen.
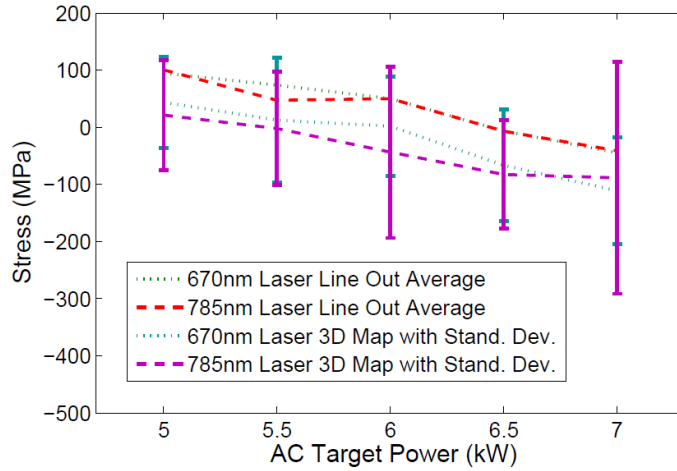
Figure 4.2: Measured stress values for five films of varied thickness, used as an example to show the discrepancy between different measurement settings on the Flexus stress mapping tool. Error bars represent one standard deviation, as reported by the tool. Films were measured first with line out measurements at 0 and 90 degrees, then a 3D extrapolated map was rendered, providing a second stress value and a stress standard deviation value.

4.2.3 X-Ray Diffraction

X-ray diffraction measurements of the AlN film are performed to measure film crystal quality. In the $\theta-2\theta$ measurement, the X-ray source is rocked from a beginning θ angle of incidence to an end angle of incidence. The detector is also rocked a value of 2θ from the plane of incidence of the source. For a wurtzite crystal such as AlN, various angles of incidence of the source will reflect a large number of X-rays to the detector, corresponding with a particular spacing in the crystal structure (Bragg reflection). AlN films with good piezoelectric properties and vertical poling will have a strong peak at a 2θ angle of 36.2° and very small peaks at angels corresponding to other AlN planes. An example $\theta - 2\theta$ curve is shown in Figure 4.3a. Secondly, a rocking curve measurement is performed. For this test, the detector is held fixed at a peak (for AlN rocking curves are taken at 36.2°) and the source is rocked, and a bell curve shape results; an example rocking curve is shown in Figure 4.3b. Rocking
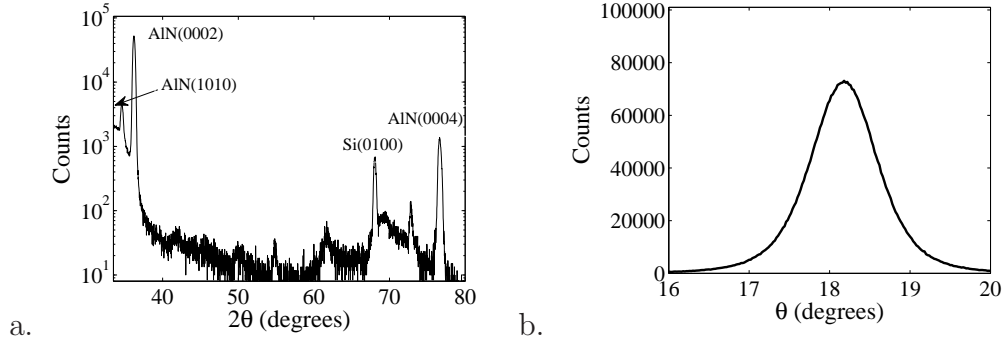
Figure 4.3: Representative XRD $\theta - 2\theta$ pattern of AlN films (a) and rocking curve diffraction peak magnitude (b) plots demonstrating c-axis oriented AlN films.

curve values are quantified by their full width half maximum (FWHM) values, which is the angular width of the rocking curve at the location of half counts. In general, a film with a FWHM of under 2° is considered to be of good quality, and will generally demonstrate high piezoelectric coefficients [99, 100, 101]. A number of factors can affect FWHM values for rocking curves, such as mosaicity of the film, film micro strain, stacking defaults, film surface roughness, so a larger FWHM value may not always correlate to a lowered piezoelectric performance.

4.2.4 Dissipation Factor and Capacitance

The resistance of a capacitive piezoelectric sensor is given by

$$R_f = \frac{1}{\omega C_f \tan\delta}, \tag{4.1}$$

where C_f is the film capacitance and $\tan(\delta)$ is the loss angle (the tangent of the angle that a lossy capacitor lags behind an ideal capacitor), also known as the dissipation factor. The Johnson noise (thermal noise) can be determined from the dissipation factor using the relation

$$\bar{v}_n^2 = 4k_B T R_f, \tag{4.2}$$
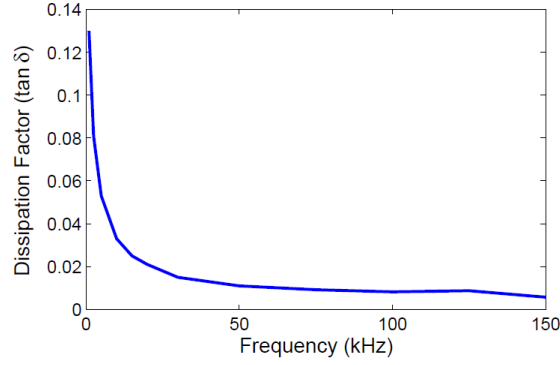
Figure 4.4: Measured dissipation factor, as a function of frequency. Added sources of trace capacitance give the dissipation factor measurement a frequency dependence that is not present in test capacitors.

where $\bar{v}_n^2$ is the root mean square power spectral density, k_B is the Boltzmann co-efficient, and T is the temperature in Kelvin. The capacitance and loss angle are measured using an Agilent 4284A LCR meter using a four terminal probe connection. Capacitance across film layers is also measured, as well as trace capacitance, depending on the design. Trace capacitance is minimized in designs by avoiding overlaid traces and making traces thin and well separated. Trace capacitance can also affect the measurement of the dissipation factor, as shown in Figure 4.4, where a trace impedance causes a frequency-dependent reading of the dissipation factor; this dependence is not present in test capacitors that do not have stray capacitances.

4.2.5 Piezoelectric Coefficient

The piezoelectric coefficient d_{31} is measured using a laser vibrometer [Polytec (Tustin, CA) OFV-303 sensor head] to measure the out of plane velocity of an actuated cantilever. The velocity response is measured every 20μm along the length of the cantilever, using a 35μm laser spot size and a micrometer for positioning. The response is recorded at each location for a set frequency range, which is chosen to be significantly lower than the first resonance of the beam. The magnitude of the
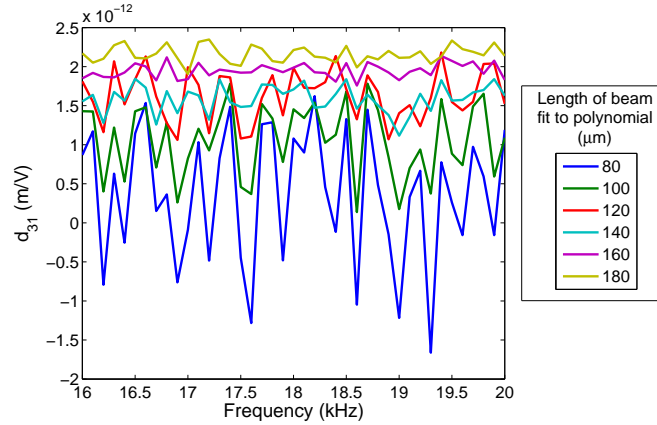
Figure 4.5: d_{31} values, as a function of frequency and by how much of the beam length, from the fixed end of the cantilever, was used for a polynomial fit to measure the curvature. As the polynomial fit improves with beam length the d_{31} value converges to approximately -2.1pm/V.

velocity responses are then converted to displacement measurements, which are fitted against a polynomial to obtain the beam curvature. The curvature is then used to calculate the d_{31} value in the method laid out in [70]. Figure 4.5 shows how the d_{31} fit improves as more data points along the length are taken into consideration.

4.3 Factors Affecting Stress

Achieving tight, repeatable control of AlN stress characteristics can be challenging, because AlN stress is dependent on the chamber target power and gas flow, the RF substrate bias during deposition, the target life, the film thickness, and the metallization of the substrate. AlN stress therefore has to be tuned on a wafer-to-wafer basis, using gas flow changes to compensate for changes in target life. An approximate guide of the effect of the above mentioned factors is shown in Figure 4.6, and descriptions of each of these factors is provided in this section.
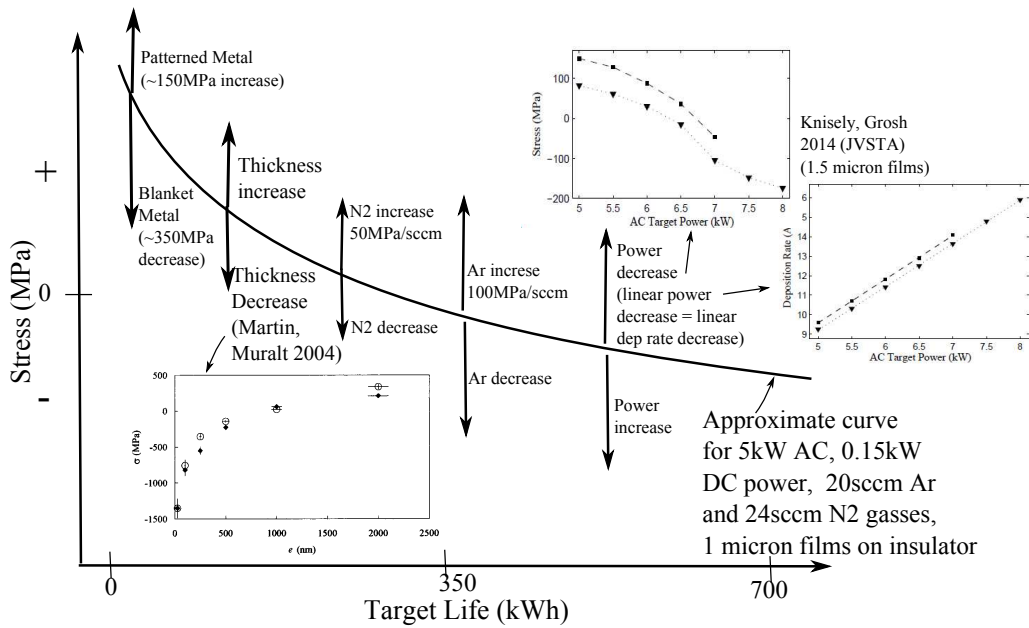
Figure 4.6: d_{31} values, as a function of frequency and by how much of the beam length, from the fixed end of the cantilever, was used for a polynomial fit to measure the curvature. As the polynomial fit improves with beam length the d_{31} value converges to approximately -2.1pm/V.

4.3.1 Gas Flow

In general, stress control of AlN films can be achieved by changing the N_2 and Ar gas flow concentrations. A 2sccm increase in Ar results in a 100MPa more tensile shift in wafer stress, while a 2sccm increase in N_2 gas produces a 50MPa tensile shift. The effect of gas concentrations on AlN orientation and crystal quality is well studied [102, 103, 78, 104, 105, 106], and in general the AMS 2004 produces high quality films when the ratio of N_2 to Ar is approximately 1.5:1 to 2:1. Because the AlN deposition power and target life are prescribed by operating procedure, changes to gas concentrations is the simplest method for achieving desired film stress.

4.3.2 RF Substrate Bias

One of the challenges of producing thick AlN films is producing a thick AlN film without high tensile stress (in excess of 300MPa tensile). For the application

91

of bimorph cantilevers, it is ideal to have stress passivated films; however, for thick AlN films the gas pressure often cannot be sufficiently lowered to compensate for the tensile stress, particularly during early target life. Applying RF bias to the substrate during deposition has been shown to shift film stress more compressive [98, 101, 103, 78, 107], but unlike the Endeavor S-Gun sputter tool, the AMS 2004 is not designed to have RF bias applied during deposition. Although this capability exists, it was found that the network providing RF bias during deposition had crosstalk from the AC power source, and the RF bias source had substantial problems with impedance matching. Additionally, the RF source was designed to operate optimally at 200W (for etching), but had problems at the lower power levels needed for substrate biasing during deposition. The minimum operating power that produced acceptable impedance matching was found to be 50W, so finely tuned low levels of RF bias were not available on the AMS 2004. Additionally, the total gas flow in the chamber had to be almost doubled in order to hold plasma when the RF biasing was applied. Although the application of RF bias makes films more compressive, this gas flow doubling shifted the films more tensile, and it was found that there was no net benefit to applying RF bias to the substrate.

4.3.3 Substrate Preparation

AlN stress and quality varies significantly depending on the surface preparation of the substrate. The effects of surface roughness on AlN deposition is a well studied field; AlN shows better orientation when it is deposited on smooth surfaces [108, 99, 109, 110]. The amount of metallization on the substrate surface affects AlN stress. AlN deposited on blanket metal, or doped Si wafers, will generally have stresses that are 300MPa more compressive than those that are deposited on an insulative substrate, such as Si with a thermal oxide layer. AlN that is deposited on blanket thermal oxide with patterned metal (small features, $<500\mu$m) has been measured to

92

be 50-100MPa more tensile than an insulative surface (the opposite of a blanket metal deposition). Because of the stress difference between blanket oxide and patterned metal, wafers prepared for the CIAO project have all non-patterned wafer space patterned with a block of 400μm square metal electrodes that have 50μm separation. The majority of the measured curvature response measured by the Flexus is therefore measured on patterned metal, better representing the stress of the AlN deposited on the metal patterning of the CIAO device.

4.3.4 Thickness

AlN films transition from compressive to tensile as they grow thicker [103, 111, 112, 113]. Typically, gas parameters are tuned during wafer characterization runs such that 1μm correspond to the zero crossing, or stress passivation. Thicker films, such as those used in the CIAO project, therefore require a reduction of gas, to compensate for the tensile shift as the film is grown past 1μm thick. It should also be noted that deposition rates decrease with target life. This is due to the fact that a groove is worn into the targets, which defocuses the reflected ions and neutrals away from the substrate.

4.4 Effect of AC Power on AlN Properties

The dominant mechanism for the determination of intrinsic stress in AlN layers is atomic peening, in which ions or accelerated neutrals that are reflected from the target bombard the substrate in a shotgun-type effect, where each bombardment creates a local area of compressive stress [106, 114, 98]. Atomic peening is dependent on the ion flux, momentum, and angle of incidence. N atoms dissociated from N_2^+ ions are the most influential bombardment molecule because of their high probability of reflection [106]. Because of this the percentage of N_2 used during deposition is very important, as is the total gas pressure; high pressure during deposition will lead to

an increase in collisions between incident ions, lowering the net flux and energy of the atoms incident on the substrate.

While the effects of gas concentrations and pressures and RF bias on the substrate do have a large impact on the stress and orientation of AlN films, they do not encompass a complete description of the atomic peening mechanism. Specifically, they neglect the effect of the power applied to the target, which plays a large role in determining the momentum of incident ions and neutrals. The effect of the target power is not well quantified, particularly for S-gun magnetron sputtering of AlN films. Kusaka, et al. [115] found that an increase in input DC power in a DC magnetron sputtering system results in larger grain sizes, increased deposition rates, and more compressive stresses, and correlations between target power and stress and between target power and rocking curve FWHM have been demonstrated in pulsed-DC deposition systems [116, 117, 103], but this has not been characterized for S-gun magnetron systems, where 40kHz AC power is the dominant power source, which co-deposits with a secondary, lower power DC source used to increase film uniformity. As the main mechanism for deposition, the AC target power influences a variety of film characteristics, including uniformity, thickness, stress, and crystal quality, and characterization of these effects are useful when determining optimal deposition parameters.

4.4.1 AC Power Experimental Procedure

AlN films were deposited on silicon substrates prepared with 575nm thermal oxide films. An insulative substrate consisting of thermal oxide on a Si wafer is chosen in order to mimic deposition conditions used to fabricate bimorph cantilever sensors, which have large sections of AlN deposited on thermal oxide on Si. The AlN films were deposited using the dual cathode S-Gun AMS 2004 magnetron sputter tool. For all depositions the system was pumped down to a base pressure of less than 2.3μTorr and the chamber was conditioned prior to each deposition. Ar flow and N_2

flow were maintained at 16sccm and 30sccm, respectively; as a result, the chamber pressure maintained a range of 2.75-2.98mTorr during deposition. The AC power delivered across the target cathodes was varied from 5 to 8kW, and the accompanying DC power across the target cathodes was held constant at 150W during deposition. Deposition times were varied such that all resulting AlN films were $1.45\mu m \pm 0.05\mu m$ thick. Films prepared in two depositions underwent a 700s initial deposition resulting in films of varied thickness, followed by a second time-adjusted deposition to match the thickness of the wafers deposited by a single deposition. Cross-sectional film images were obtained using a Hitachi In-line SEM using a conductive coating to prevent charging. Grain boundary analysis was performed using ImageMetrology SPIP6 software.

4.4.2 AC Target Power and Target Life Effects

All AlN films presented exhibited good c-axis orientation when measured by XRD, exhibiting strong (002) peaks, shown in Figure 4.3a. Rocking curves measured at at the (002) peak of 36.2° all demonstrate low (¡1.5°) full width half maximum (FWHM) values, such as the rocking curve shown in Fig. 4.3b. Target life affects AlN film characteristics such as stress and deposition rate, so AlN films prepared further into the target life (200kWh) are denoted separately from those that were prepared earlier in the target life (130kWh). Figure 4.7a shows a linear dependence of the deposition rate as AC target power is increased; as target life is increased the trend remains linear but the rate is uniformly decreased due to the decrease in target surface area that is directed at the substrate as tracks in the targets form. The error bars for Figure 4.7a are smaller than the plot points. Nonuniformity was also found to increase with target life (Figure 4.7b), though it is not clear if this is repeatable or if this is due to degradation of the magnets that control the target plasma that was discovered shortly after the 200kWh target life depositions. Nonuniformity was measured using
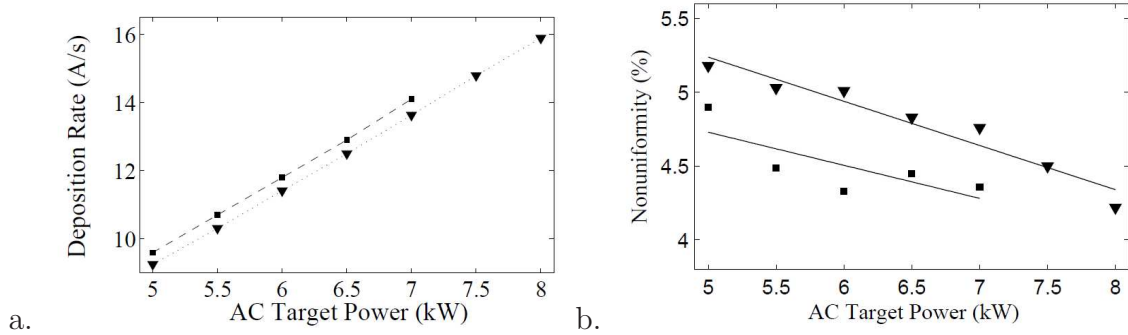
Figure 4.7: AlN deposition rate versus AC target power, performed at 130kWh targetlife (squares) and at 200kWh target life (triangles). Trend lines on this and subsequent figures are for visual reference only.

a five point measurement of film thickness[Nanospec 6100 reflective spectrometer]. Error measurements on the accuracy of the five point nonuniformity measurement are not available for error bars. Polycrystalline films, such as magnetron sputtered films, can be characterized by three zones, depending on the deposition parameters. Zone 1 of the structure zone model describes films with porous, columnar stacking and tensile film stresses due to inter-grain "zipping" forces. Zone 2 films are dense with compressive stresses that are dominated by atomic peening [118]. The transition zone between zones 1 and 2, called the T Zone, is characterized by dense, columnar polycrystalline films that shift from tensile to compressive film stress as momentum of the ions and accelerated neutrals is increased. An increase in bombardment momentum can be achieved in a number of ways, including by increasing target power or decreasing gas pressure [119, 114]. The measurements of film stress, as a function of target power, that is shown in Fig. 4.8(a) demonstrate the expected shift from tensile to compressive film stress as bombardment momentum is increased, consistent with the model of T zone films [114]. This zone assessment agrees with the grain structure observed in other S-gun deposited AlN films [98]. As the target life is increased the stress trend shifts more compressive by approximately 60MPa across the power range, reflecting a change in the target and chamber impedance as the target is eroded. By
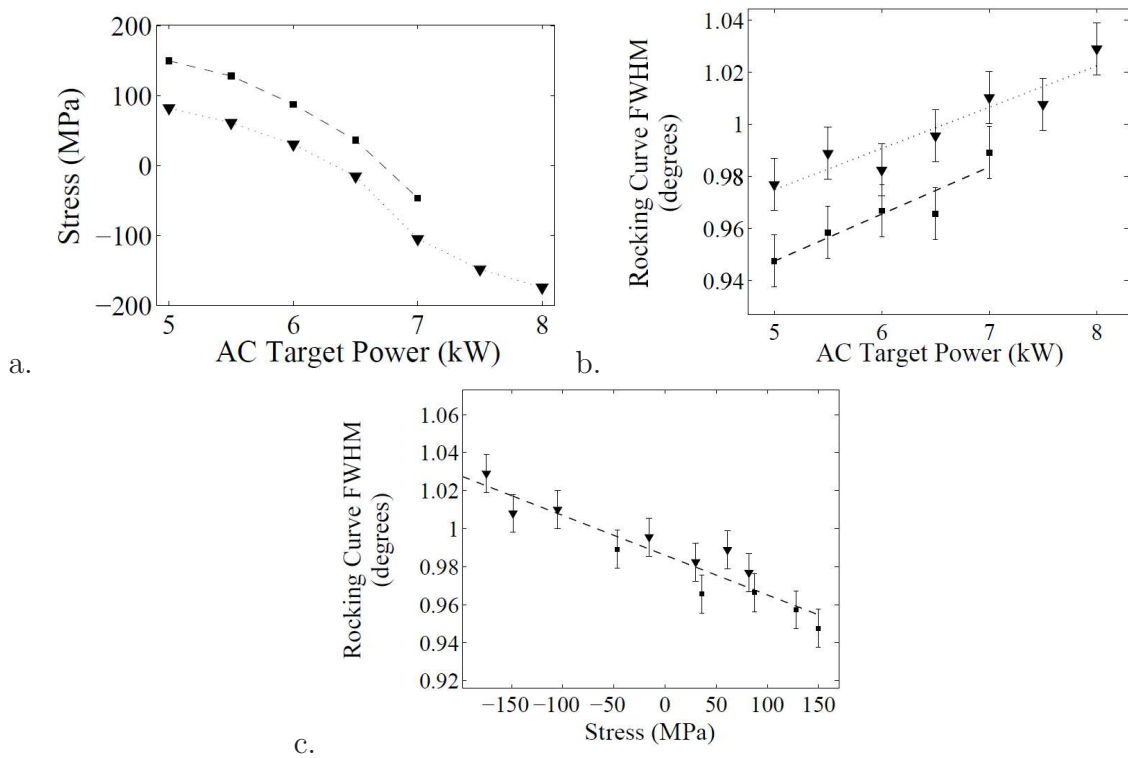
Figure 4.8: Relationship between residual film stress (a) and rocking curve FWHM (b) measurements as a function of AC power for AlN films deposited at 130kWh (squares) and at 200kWh (triangles) target life. A linear correlation exists between stress and rocking curve FWHM (c) that is not affected by target life. Error bars for FWHM values represent tool precision error. Each point represents a single deposition; repeatability testing was not performed due to subsequent tool failure.

contrast, increasing the AC target power had only a small effect on the XRD rocking curve full width half maximum (FWHM), taken at the (0002) peak (Figure 4.8b). All rocking curve FWHM values are below $1.03°\pm0.01°$, indicating high quality films with few defects. A correlation has been demonstrated between low rocking curve FWHM values and high d_{33} piezoelectric constant [107, 99, 101]. We find a linear trend was found between the stress and the FWHM such that more tensile films had slightly smaller FWHM values. If this change were due to changes in film stacking behavior this trend would be expected to have a positive slope, as more tensile films are closer to Zone 1, and should therefore be more porous and have higher FWHM values. Instead, the variation in FWHM observed is likely due to microstrain, rather than crystal quality (Figure 4.8c).

4.4.3 Effects of One Versus Two Depositions

Thick AlN films ($> 1\mu$m thick) have a number of advantages, including better crystal quality, higher piezoelectric coefficients, and low dissipation factors [111]. However, thick films are difficult to achieve in a single deposition due to the build-up of material on chamber walls that leads to plasma instability during deposition. Preparing AlN films in multiple depositions can be advantageous, as the stress of films deposited in multiple depositions can be controlled to a higher degree by altering deposition parameters in response to wafer stress measurements of previous depositions. Stress control and characterization is particularly important for applications that use stacked layers of AlN such as bimorph cantilevers [71, 120], as the stress gradient through an AlN film is significant and can result in curled beams [111, 121].
In order to study the discontinuities introduced into a film by breaking vacuum between depositions, a second set of wafers was prepared and compared with the wafers discussed in section 4.4.2 of this thesis. Five wafers first underwent a 700s deposition, with AC power varied from 5 to 7kW. Each wafer, at its respective AC power, then
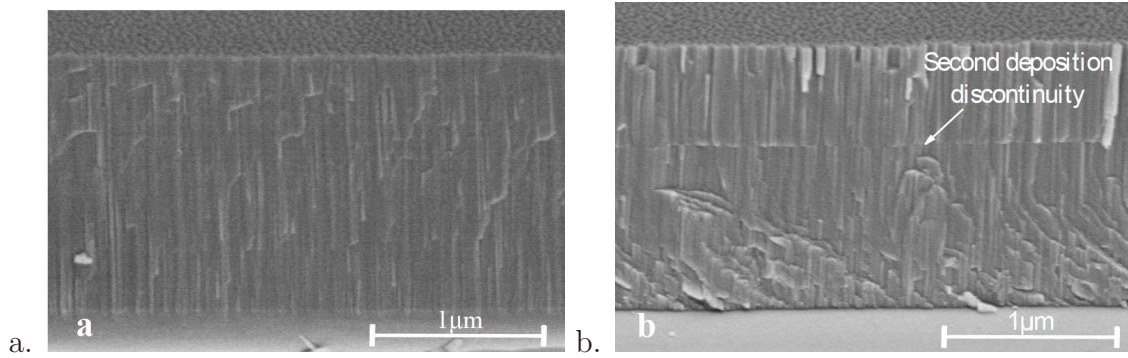
Figure 4.9: SEM images of a film deposited in one deposition (a), and with two depositions (b). A break occurs in the columnar structure of the film with two depositions. Each film is 1.5μm thick, and was deposited using 6.5kW AC power.

underwent a second deposition to increase its thickness to $1.5\mu \pm 0.05\mu$m. A 180s, 200W RF substrate bias etch step was performed prior to each deposition to remove residuals from the surface of the wafer. Figure 4.9 shows scanning electron microscope (SEM) cross-section images of the wafers deposited at 6.5kW AC target power. Figure 4.9(a) shows continuous, c-axis oriented columnar crystal structure growth from a film that was deposited in a single deposition. In contrast, a line of discontinuity in the columnar structure is apparent in the dual deposition film (Figure 4.9b), indicating that the AlN columns do not necessarily resume growth from the underlying film structure in a second deposition, instead a new lattice structure is formed in each deposition. Both images in Figure 4.9 show dense, columnar films consistent with T zone structure. The two primary differences between single and dual deposition films of the same net thickness were observed to be changes in the roughness and the XRD rocking curve FWHM values (Figure 4.10a,b). As shown in Figure 4.9, a break in vacuum between depositions introduces a discontinuity to the film from roughening from exposure to air, particles, and a second RF biased etch step. Consequently, films that were grown using two depositions had approximately double the roughness of those that were grown in a single deposition, as shown in Figure 4.10a. This discontinuity

99

in the crystal growth, in addition to the added roughness, resulted in an increase in the rocking curve FWHM values by approximately 0.35° (Figure 4.10b). Error bars in this plot represent the tool precision error. This precision error was measured by repeating the same measurement five times at the same location on a sample and assessing the standard deviation of the measurement values. This was repeated for three separate wafers with comparable results. However, the film stress is not affected by the discontinuity; this is consistent with what would be expected from the atomic peening model, as none of the parameters that affect stress are varied between the depositions (Figure 4.10c). An analysis of the grain sizes of the two films used for SEM images in Figure 4.9 supports this, revealing little change in average grain size; the single deposition film had an average grain diameter of 38.9nm ±12nm, and the dual deposition film averaged 36.3nm ±12nm. Images of the surfaces used, before and after grain boundary assessment, are shown in Figure 4.11.

4.5   TEM Imaging of AlN

X-ray diffraction (XRD) measurements of AlN crystal quality are good predictors of a films piezoelectric performance; low rocking curve full width half maximum (FWHM) values are roughly correlated with higher piezoelectric coefficients [99]. However, rocking curve FWHM measurements are convolutions of film micro strain and mosaicity, crystalline defects, wafer curvature, and beam penetration, though not all of these mechanisms for FWHM broadening contribute to degraded piezoelectric performance. Transmission electron microscopy (TEM) observations of thick AlN films are therefore useful to further understand the underlying stacking behavior of the AlN film, in order to identify parts of the deposition process that contribute to degraded film quality. The TEM imaging in this section focuses on identifying the stacking irregularities that occur at the beginning and ends of AlN deposition, as well as the stacking that occurs when an AlN film is deposited on top
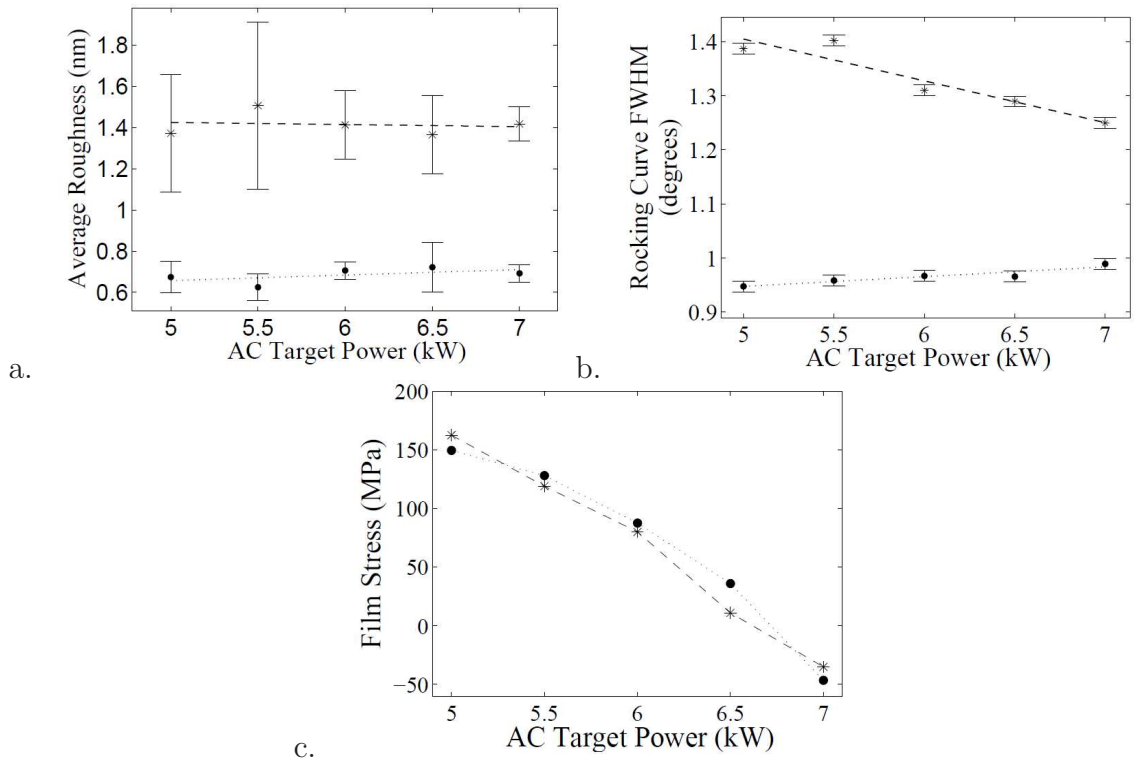
Figure 4.10: Comparison of roughness (a), residual stress (b), and X-Ray diffraction rocking curve FWHM (c) measurements of films, as a function of AC target power, deposited by a single deposition (circles) and by two depositions (stars). Error bars for FWHM values represent tool precision error.

101
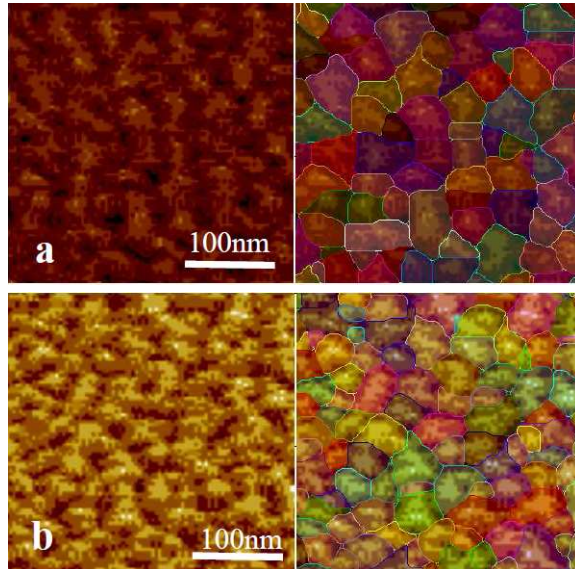
Figure 4.11: Closeup of the grain structure of the SEM image (angle corrected) of the single deposition (a) and two deposition (b) films shown in Figure 4.9, before and after definition of the grain boundaries.

of a previously deposited AlN film. Understanding this behavior provides insights into potential changes in the deposition procedure to produce higher quality films.

4.5.1 TEM Sample Preparation

TEM imaging was performed on the 6.5kW, dual deposition film described in Section 4.4 above, and which appears in the SEM and grain boundary images of Figures 4.9 and 4.11. A review of its deposition parameters, such as gas flow and target power, is given in Table 4.1. Properties of this film are compared with the 6.5kW single deposition film (also in Figures 4.9 and 4.11) in Table 4.2, for reference. Subsequent to this measurement two other AlN film samples were measured using TEM. These samples were the 5.5kW and 8kW double deposition samples whose properties are characterized in Section 4.4. The 8kW sample had poor preparation due to too much ion milling, but images from the 5.5kW film are presented in Section 4.5.6.

TEM samples were prepared by bonding two thin slices of a sample together film-

Parameter	Value
Substrate	4" Si wafer, 575nm oxide
Vacuum Prior to Deposition	2.3μTorr
Deposition Pressure	2.83mTorr
AC Target Power (40kHz)	6.5kW
DC Target Power	150W
Substrate Roughness	1.36nm (average)
Ar Gas Flow	16sccm
N_2 Gas Flow	30sccm

Table 4.1: AlN deposition parameters.

to-film. The sample was then manually shaped into a thin and tapered slice using sand paper, such that the film-film boundary ran lengthwise along the sample. The sample was mounted on a 3mm molybdenum grid, with the thinnest part of the sample aligned to the center of the grid. The thin tip of the sample was then ion milled using the Gatan PIPS Model 691 Fine Ion Milling tool for several hours, until it was approximately 20nm thick. TEM imaging of the sample was performed using the JEOL 3011 High Resolution Electron Microscope. The sample was loaded using a double tilt sample holder, which enabled alignment to the AlN grain axis.

4.5.2 Measured AlN Properties

Both 6.5kW AlN films exhibited good quality c-axis orientation, exhibiting a strong (002) peak and a rocking curve FWHM values under 1.3°. The θ-2θ and rocking curve response of the two-deposition film is shown in Figure 4.12a and b, respectively. Both AlN films had low (< 50 MPa) stresses, and had comparable film thicknesses and grain sizes (Table 4.2). Interestingly, the two-deposition AlN film had lower nonuniformity, which is likely due to nonuniformity in the RF bias etch that was performed in between depositions, though this could be due to problems with the

AlN Film Property	Two Dep Film	Single Dep Film
Thickness	$1.50 \pm 0.09\mu$m	$1.47\pm0.1\mu$m
Grain Size	36.3 ± 12nm	38.9 ± 12nm
Film Nonuniformity	4.0%	4.45%
Roughness (1st dep)	4.30nm	N/A
Roughness (2nd dep)	6.15nm	4.09nm
FWHM at (002) peak	$1.29\pm0.01°$	$0.97\pm0.01°$
Stress	14MPa	38MPa

Table 4.2: AlN film properties.

plasma due to burnt out target magnets. For AlN film applications that require low nonuniformity tolerances, a potential mechanism for reducing nonuniformity may be to apply an RF bias etch after deposition. Selected area electron diffraction of the 6.5kW dual deposition AlN sample, shown in Figure 4.12c, confirmed that the film was of good quality and c-axis orientation. The c-axis lattice coefficient was measured to be 4.97 ± 0.1 Å, matching well with literature values of 4.981Å [122].

4.5.3 6.5kW Dual Deposition AlN-Oxide Interface

HREM measurements of the AlN growth from the oxide substrate is shown in Figure 4.13. Nucleation sites for the AlN occur every 4-10nm along the oxide substrate, but they resolve into well structured AlN within the first 5-6nm of deposition, corresponding with the first 3-5 seconds of deposition. This collection of poorly defined dense grains, without evidence of shadowing, is consistent with a film in the transition zone (T zone) of the structure zone model [118]. Films in this zone lack the void areas due to shadowing that are characteristic of Zone 1, but are not deposited with sufficient energy to form the large, distinct grains that are characteristic of Zone 2 [118].
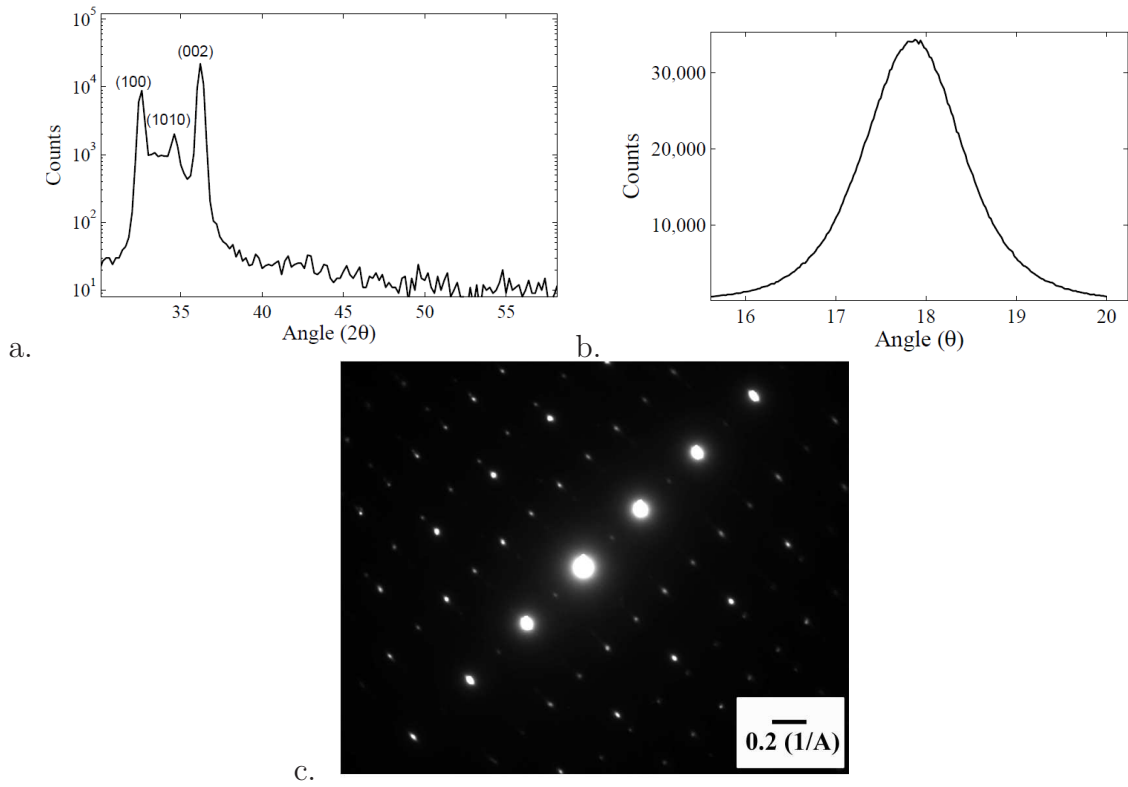
Figure 4.12: X-ray diffraction (a,b) and SAED (c) of the two-deposition AlN film, demonstrating high quality c-axis oriented AlN.
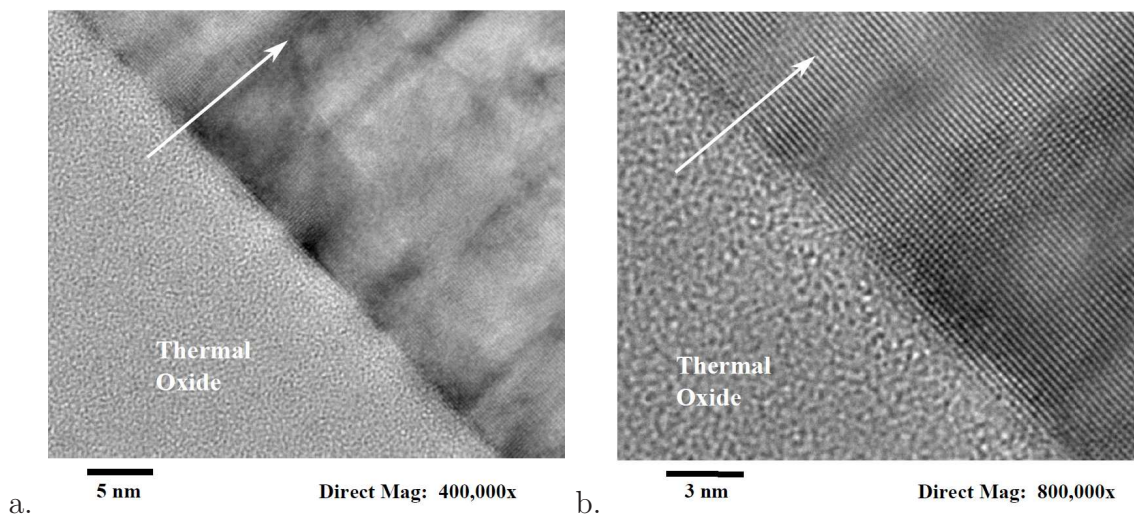
Figure 4.13: HREM measurement of the AlN growth off of the thermal oxide substrate at 400k times (a) and 800k times (b) magnification. The arrows represent the direction of the film growth.

4.5.4   6.5kW Dual Deposition Sample AlN-AlN Interface

Surface contamination occurs when vacuum is broken, so each additional deposition cycle (with vacuum broken in between cycles) is expected to produce additional surface roughness. Breaking vacuum also returns the substrate to a lower temperature at the start of a second deposition (the AMS 2004 can neither measure nor control this temperature change), which reduces adatom surface mobility. As a result, in breaking vacuum between two depositions results in a layer of process induced dislocations and faults form at the junction between the two depositions. This line of discontinuity can be seen in the bright field macroscopic image of the two-deposition film (Figure 4.14a); the line is magnified in Figure 4.14b and c. In the HREM magnified views, the AlN growing from the junction site shows a number of dislocations (examples shown with black arrowheads). The film mosaicity is also increased; an example of this is shown with the dashed lines in Figure 4.14c, where the line with long dashes is parallel to the AlN crystal growth plane prior to vacuum being broken and the short dashed line is parallel to growth during the second deposition. A second long dashed line is placed near the short dashed line, to demonstrate the change in angle. As with the AlN growth from the oxide substrate, the stacking becomes ordered about 5-6nm from the AlN-AlN interface, and the grains established in the first deposition are largely continued.

4.5.5   6.5kW Dual Deposition AlN Film Top Surface

Figure 4.15 shows dark field imaging of the top of the two-deposition AlN film, as well as a high magnification image of the film near the film surface. When AlN is deposited in the AMS 2004 sputter tool, the film deposition is terminated simply by turning off the power to the plasma. High magnification imaging of the top of the AlN film (Figure 4.15b) reveals 5-6 nm of poor stacking behavior that likely corresponds to the residual deposition that occurs after the power has been turned off. This top

106

a.

AlN-AlN Interface

Thermal Oxide

300 nm   Direct Mag: 10,000x

b.   5nm   Direct Mag: 400,000x

c.   3nm   Direct Mag: 800,000x
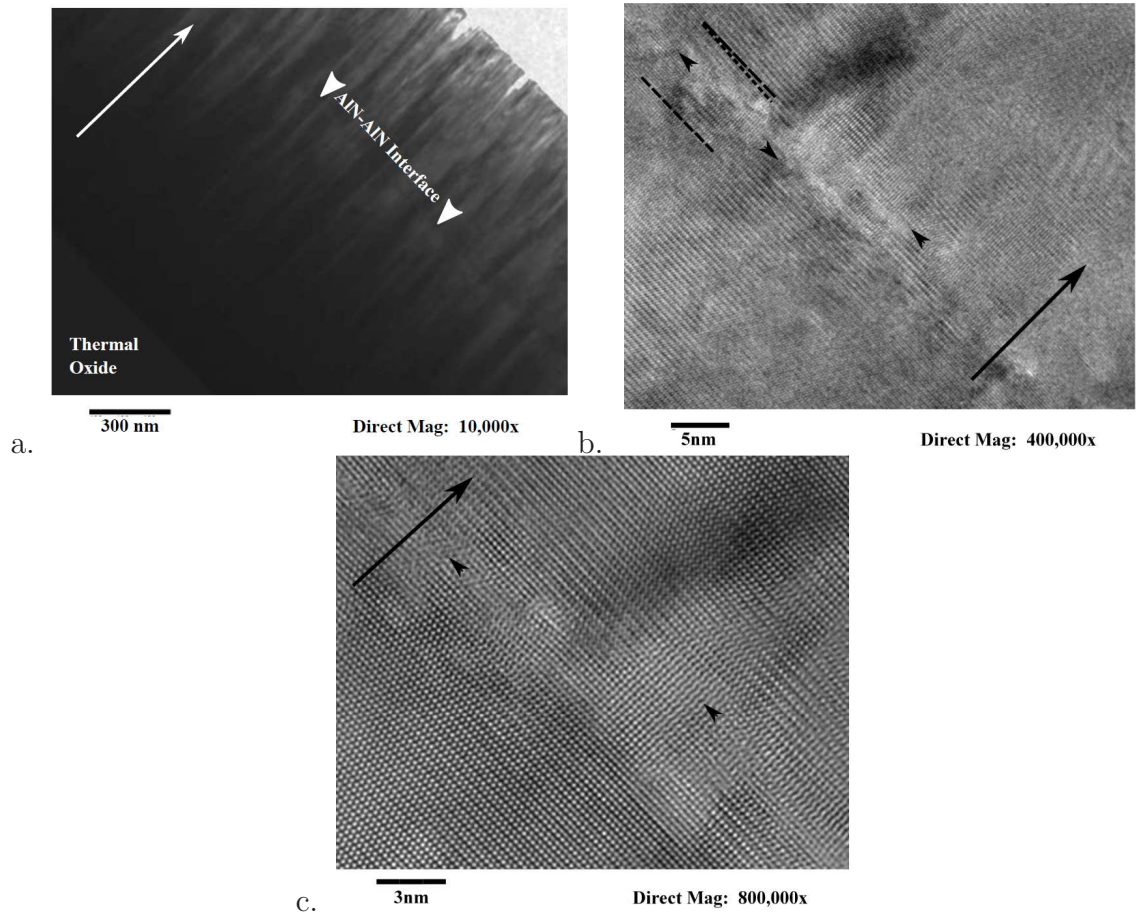
Figure 4.14: An AlN-AlN interface (white arrowheads, a) is formed between two depositions of AlN. 400k times (b) and 800k times (c) magnification views of this interface show dislocations (examples shown with arrowheads), as well as changes to the grain growth angle (dashed lines). The arrows represent the direction of the film growth.
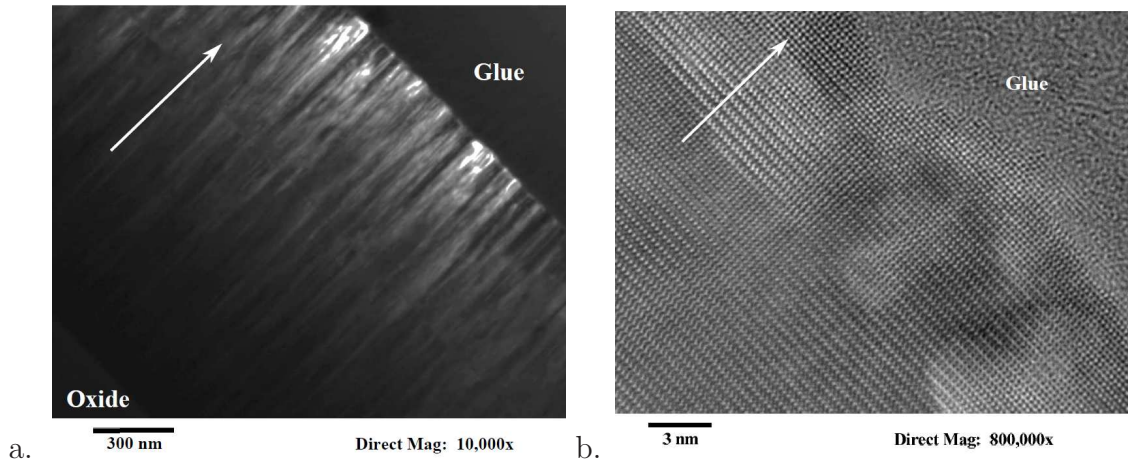
Figure 4.15: The dark field image of the two-deposition film (a). The AlN grain growth is well ordered, except for a degradation of film quality and granular orientation near the top of the AlN film, seen with 800k times magnification (b). The arrows represent the direction of the film growth.

layer adds an extra amount of surface roughness. While the thin layer likely does not affect piezoelectric quality for thick films, thin AlN films may be improved by a short RIE etch or polishing to remove this layer. Removal of this layer may also be beneficial for wet etching where etch rates are dependent on film quality and surface roughness.

4.5.6   5.5kW Dual Deposition TEM Images

The images in Figure 4.16 show the oxide-AlN growth interface of the 5.5kW film. As with the 6.5kW film, shown in Figure 4.13, the AlN stacking generally resolves into larger crystal structure within 5-6nm of growth. No difference between the 6.5 and 5.5kW AlN-oxide interface was apparent. Figure 4.17a is a magnified image of the AlN-AlN interface, similar to the images in Figure 4.14. In this image, it is apparent that the first blanket AlN layer has very few structural defects, and that the second deposition initial growth is less ordered for approximately 5-6nm, also agreeing with the results seen from the 6.5kW sample imaging.

The AlN film surface of Figure 4.17b, however, does not demonstrate the same 5-10nm
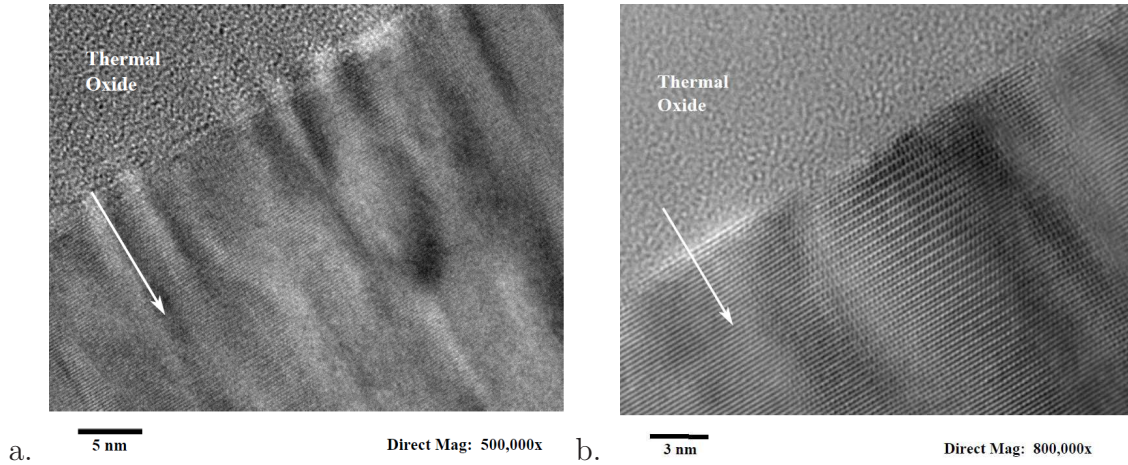
Figure 4.16: 5.5kW Oxide Interface at 500k times and 800k times magnification. White arrows represent the direction of growth.

of disordered growth that is seen in Figure 4.15. The grain growth in the top 100nm of Figure 4.17b is angled, and grains are growing in curved directions, particularly for the last 50nm of growth. This behavior is possibly due to grain zipping behavior as the 5.5kW film is tensile, whereas the 6.5kW film is compressive, and its packing behavior is more dominated by atomic peening, rather than tensile inter-grain forces. However, more testing is needed, as only one sample was tested, and the curvature could also be an effect of an off-angle sample preparation, or of damage from ion milling.

4.5.7   TEM Imaging Conclusions

TEM imaging of the AlN-AlN interface for both the two-deposition 6.5kW film and 5.5kW film revealed process induced faults and dislocations, as would be expected with an interruption in deposition. These anomalies resolved within 5-6nm from the site where vacuum was broken; this contributes to the increase in FWHM and roughness of the two deposition film. Imaging of the initial AlN growth on the oxide showed similar behavior, with high quality AlN forming within 5-6nm of seeding. This small layer of defects is unlikely to compromise the piezoelectric quality of thicker AlN
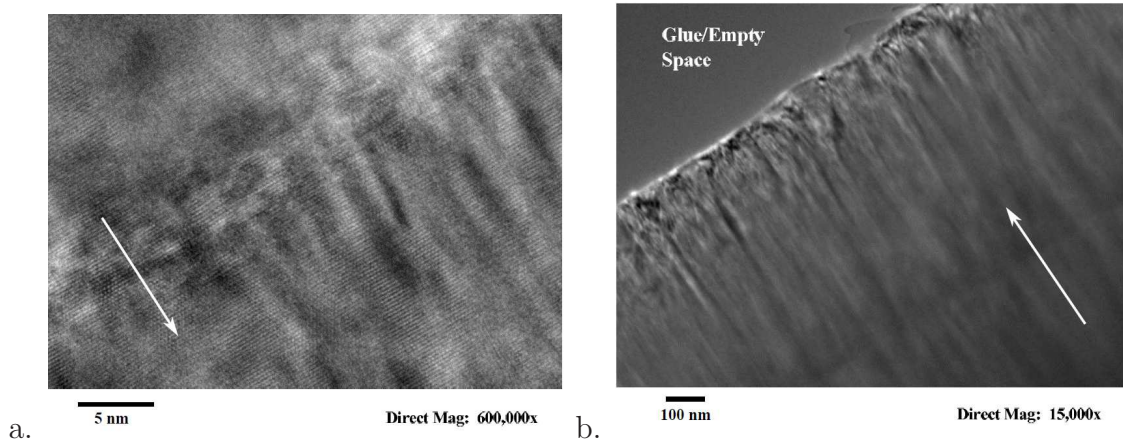
Figure 4.17: 5.5kW AlN-AlN interface (a) and film top surface (b). White arrows represent the direction of grain growth.

films.

High resolution imaging near the 6.5kW film surface shows a thin (5-6nm thick) layer of AlN with poor stacking, indicating that the method of terminating film deposition may produce a residual film of less ordered, rougher AlN. The 5.5kW film also had disordered surface behavior, with curved grain growth in the last 100nm of deposition. In both of these cases the removal of the top 50-100nm would likely improve both the optical and piezoelectric performance of the films, particularly for thin film depositions.

4.6   Wet Etching of AlN

Dry etching via locations in AlN (a Cl_2 and BCl_3 etch performed in the LAM 9400) is challenging because RIE etching of AlN is has poor selectivity to the underlying metal. Wet etching (a heated bath using phosphoric acid, TMAH-, or KOH-based etchangts) is an alternative that has good selectivity to metals, but it produces a large undercut.

In this section the relative merits of common AlN wet etching techniques are discussed. The efficacy of two wet etchants (hot phosphoric acid and the KOH-based developer

110

AZ400K) were compared using the metrics of undercut, mask pinhole etching, and how well the etchant removed residual amorphous AlN from the metal pads. PECVD oxide was used as a mask, and was found to be effective for smooth surfaces but less effective for open mask edges where a step height is present. Pinhole etching behavior presented quickly with hot etching, but the oxide mask was found to be sufficiently resilient to enable etching of 1μm thick AlN films.

4.6.1   Comparison of Common AlN Wet Etchants

Common etchants for AlN are hot phosphoric acid and KOH-based etchants, such as AZ400K [123]. Heated Al etchant can also be substituted for hot phosphoric acid with no noticeable difference. AlN etching using hot phosphoric acid was previously demonstrated by Littrell [70]. However, hot phosphoric acid, when not properly masked, can have a lateral undercut of up to 50:1 [120]. TMAH based etchants etch AlN very slowly, causing more of a surface roughness change than an actual etch (the etch is approximately 1μm per 10 hours). It is this roughening that makes traditional TMAH-based developers (AZ 300, MF 319) poor options for use as developers; CD-30 must be used instead. KOH and KOH-based developers (namely AZ400K) are also well documented etchants of AlN, as well [124]. KOH etches AlN isotropically and quickly, but an oxide or nitride mask is necessary with KOH based etching of patterns, as many photoresists (SPR 220 3.0 and others) are instantaneously removed by KOH, as were metal masks that were tried.

In general, masking AlN for wet etching is challenging: photoresist will delaminate in 1-3 minutes of etching, PECVD oxide masks have pinhole etching and undercutting after as few as 3 minutes of etching, and metal masks showed high amounts of delamination within seconds of exposure to etchants. Of these options PECVD oxide masking, using 2μm of oxide or more, has shown the most potential, provided that the AlN material etched is not more than 1-2μm of AlN, and provided that the
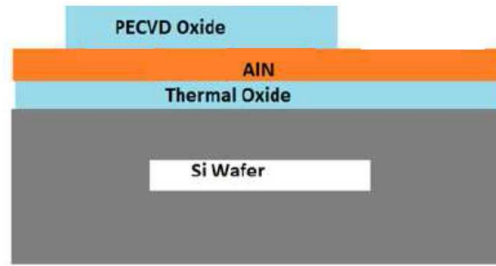
Figure 4.18: The cross-section view of the patterning for wafers undergoing an etch test using blanket AlN with a patterned PECVD oxide mask.

temperature of the etchant is not too hot (85C for hot phosphoric acid, and over 60C for AZ400K etching, as is detailed in this section.

4.6.2 Wet Etching Using a Patterned PECVD Oxide Mask on Unpatterned AlN

An initial test of wet etchants was performed using wafers prepared with 565nm of thermal oxide and 1μm blanket AlN. The stresses of the AlN films used used were measured, and the crystal quality of the AlN was not verified. 2μm PECVD oxide was deposited using the GSI at 380C for use as a mask. The oxide was patterned with large rectangular test features, shown in Figure 4.18. The AlN layers were etched in one of four different etchants: Hot phosphoric acid at 85C for 3min (Fig. 4.19a) and AZ400K developer at 20C for 17min, 40C for 2min 20s, and 60C for 1min (Fig. 4.19 b-d, respectively). Etch times were determined visually. Minimal undercut can be seen on all patterns, but residual amorphous AlN left on the electrode post etching was least present for 60C AZ400K etching and most present for 20C AZ400K etching.
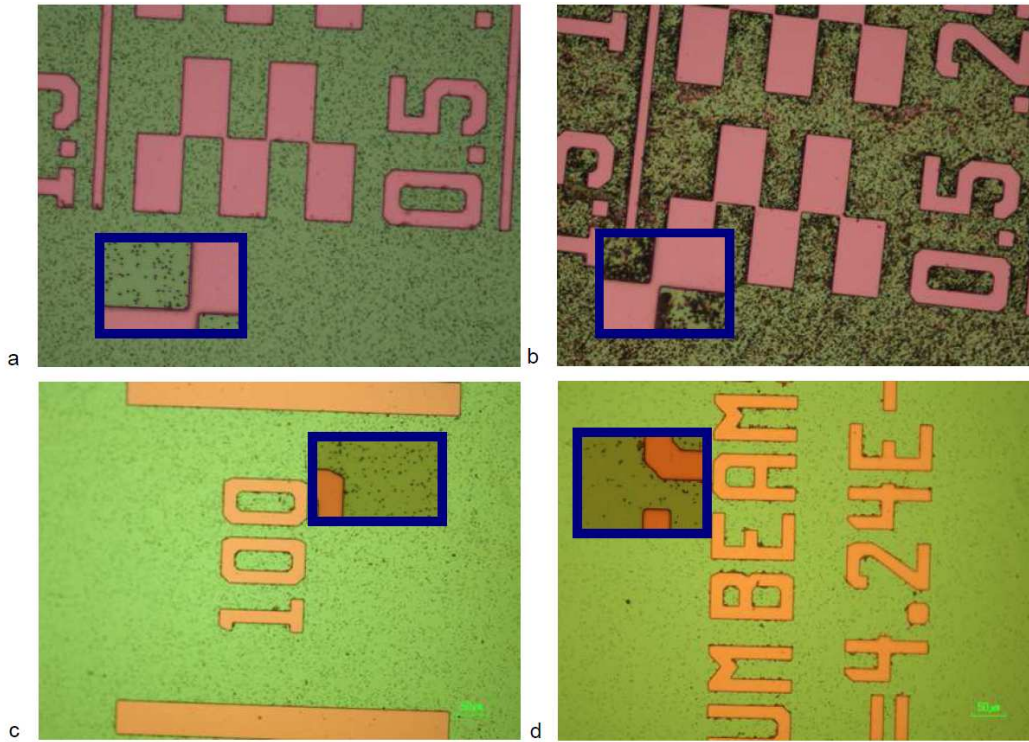
Figure 4.19: 20 times magnification images of wafers etched using 85C hot phosphoric acid (a), and AZ400K developer at 20C (b), 40C (c), and 60C (d). The pink/orange patterning are the areas where the AlN was masked by PECVD oxide, while the green areas are areas where the AlN was exposed and etched away, exposing the underlying layer of thermal oxide. Magnifications of each image are shown in the blue boxes.
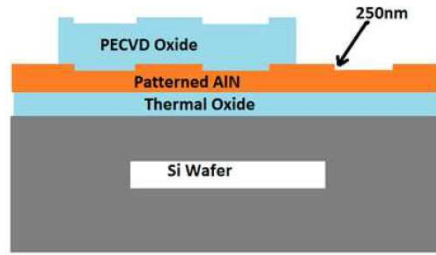
Figure 4.20: The cross-section view of the patterning for wafers undergoing the second etch test, where patterned AlN was masked by PECVD oxide mask patterned differently from the AlN patterning.

4.6.3   Patterned PECVD Oxide Mask on Patterned AlN

A second test was designed to examine the effectiveness of the oxide mask that was deposited on a patterned AlN surface. Substrates were prepared as described in the previous section, but prior to the oxide mask deposition the AlN was etched 250nm using a mask with many 400x400μm wide squares. This mask was chosen to maximize the number of step heights that were covered by the oxide pattern. The oxide mask was deposited and patterned as in the first test. This process is shown in Figure 4.20. Hot phosphoric acid at 85C and AZ400K at 60C were chosen to be the test etches for the patterned AlN wet etch test. In Figure 4.21 results of etching the one patterned AlN wafer for 2min, 3min, and 5min (Fig. 4.21 a-c, respectively) in 85C phosphoric acid are shown. After two minutes of etching residue of the AlN is still visible, whereas after 5 minutes of etching significant lateral undercuts start to occur. By carefully monitoring etch times, in this case three minutes, an ideal etch time can be found that minimizes both residue and undercut.

The PECVD mask did not conform as well to AlN that had 250nm step height features (red areas in Figure 4.21, resulting in undercut of up to 50μm at locations where the edge of the oxide mask intersected an AlN step height; a cross-section of this is shown in Figure 4.22. Poor coverage of the oxide mask at the step height

2 min hot phosphoric etch
380C PECVD oxide mask

50 um

400 um

a.

Image taken at 10x Mag

3 min hot phosphoric etch
380C PECVD oxide mask

50 um

400 um

b.

Image taken at 10x Mag

5 mín hot phosphoric etch
380C PECVD oxide mask

50 um

400 um

c.

Image taken at 10x Mag
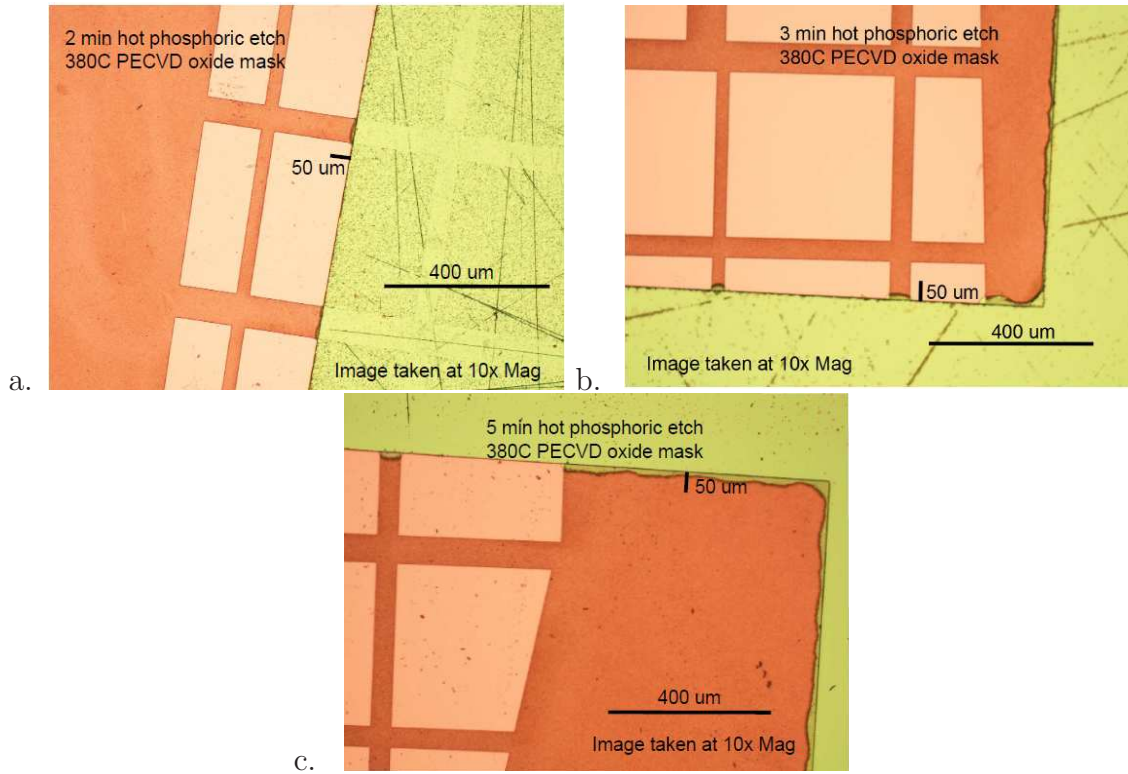
Figure 4.21: 10 times magnification images of a wafer etched in 85C phosphoric acid after 2,3, and 5 minutes of total etching time (a,b,c respectively). White areas in this image indicate areas with 1μm AlN covered with 2μm PECVD oxide, red areas indicate areas where the AlN is 750nm thick and covered with 2μm PECVD oxide, and green areas are where there was no PECVD oxide mask and the AlN has been etched away to reveal the underlying thermal oxide. In b) and c) the edge of the (clear) PECVD mask can be seen, as well as the undercut of the etch of the AlN.

No oxide gap where edges
of AlN patterning occur.
No etching at the middle
of the oxide pattern.

Gaps where etchant
can enter, exposed
at the edge of the
oxide patterning
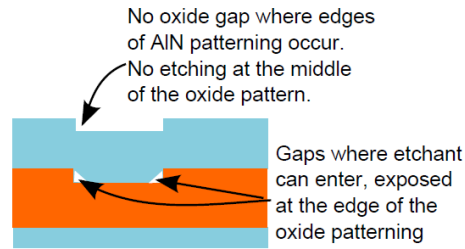
Figure 4.22: Cross section of the patterning. Poor step height coverage of the PECVD oxide at the edges of the AlN patterning allow areas where the etchant can undercut. However, the 2μm thick oxide mask was sufficient to fully mask the AlN everywhere but at the edges of the oxide patterning.

locations produced a gap in masking at the mask edge - step height intersection.

Figure 4.23 shows the results of a 3min 40s etch of a patterned wafer in 60C AZ400K; this etch time was determined visually by the time it took for the patterning to fully clear. However, as can seen by the locations of significant undercut (for this etchant a partial undercut, which appears black, occurs), visual inspection does not constitute the best method for determining etch time at such a high temperature because the etch is occurring too rapidly. In conclusion, heated AZ400K and phosphoric acid both left minimal residue and had fast etch rates, but the PECVD oxide mask showed better resilience to hot phosphoric acid than to 60C AZ400K, which showed evidence of pinhole formation/exacerbation. Hot phosphoric acid was found to be a preferable etch for patterns with high step heights, but it produced higher degrees of undercut than the AZ400K etchant produced. 40C AZ400K etching showed a good compromise of low residue, minimal undercut, and no pinhole formation. For films that do not have significant step heights, 40C AZ400K provides fast etching with minimal problems with pinholes or undercut.

a.

b.

c.
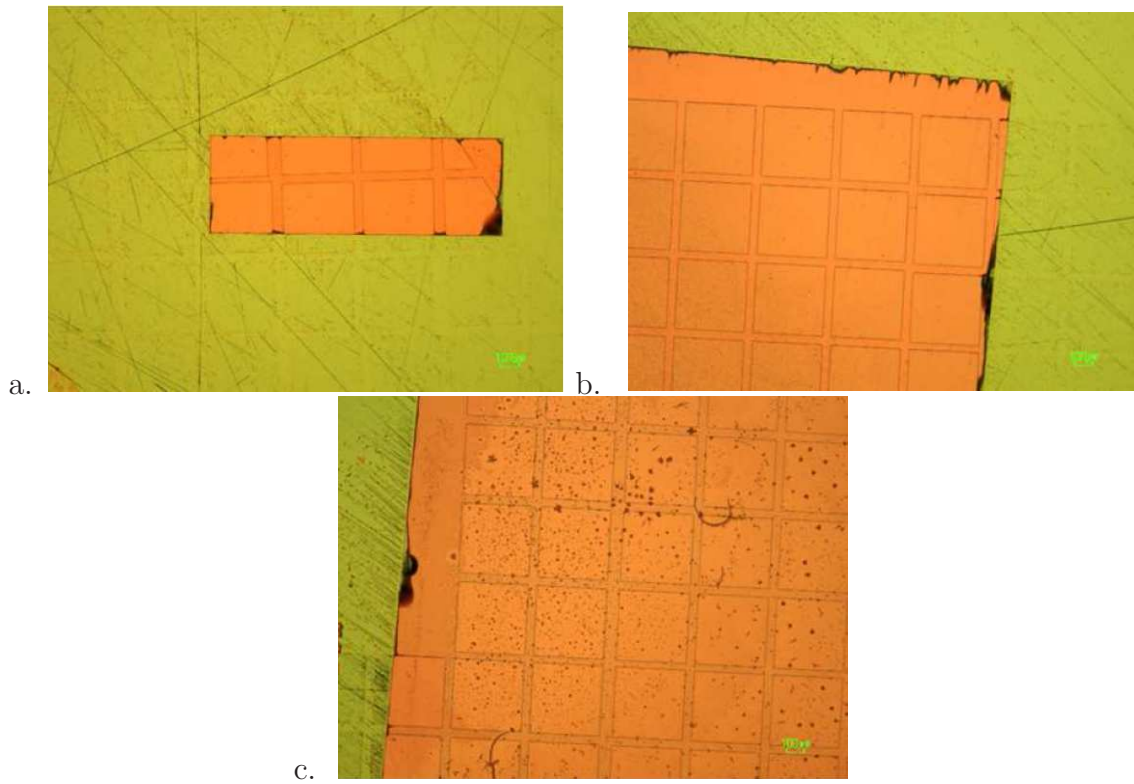
Figure 4.23: 5 times magnification imaging of a wafer with patterned AlN and a PECVD oxide mask after etching in 60C AZ400K. Significant undercut of the mask can be seen around the edges of the oxide mask in a) and b). Unlike the 85C phosphoric etch, pinholes in the oxide were seen after long etches in 60C AZ400K (c).

CHAPTER V

In Vivo Performance

Once fabricated, the performance of the CIAO device is measured *in vitro* using a laser vibrometer to measure the frequency response of the device in air and fluid. While these tests confirm the device functionality as a sensor and actuator, it is important to also measure the device performance *in vivo*. The goal of the *in vivo* experiments discussed in this chapter was to demonstrate that a CIAO device could be successfully implanted and used to measure the pressure response of the fluid of the ST when a sound is played at the entrance to the ear canal.

Functional CIAO prototypes were implanted in two guinea pigs (one prototype per animal). The purpose of these implantations was to characterize the *in vivo* performance of implanted CIAO devices. The first CIAO implant was broken during the surgical implantation, but the second implantation was successful; four beams were found to be intact both during the acute *in vivo* testing and later during the *post mortem* examination, indicating that the design had good mechanical robustness.

Electrical *in vivo* testing was used to confirm that the CIAO implant had electrodes that were capable of evoking a brain response when a current was applied. Most notably, *in vivo* testing also confirmed that the CIAO implant was capable of transducing sound pressure in the ST perilymph into electrical signals, which is the first step towards having a CIAO device capable of restoring hearing. In this chapter,

the implant preparation, surgical procedure, and *in vivo* device performance are discussed.

5.1   Implant Preparation

5.1.1   Pt-Ir Wire Attachment

Both generations of CIAO prototypes were designed to include electrical cabling, but this cabling was not used for the initial acute *in vivo* tests described in this chapter because robust electrical attachment of the cabling to the probes was never achieved. Instead, probes were prepared by silver epoxying two wires to the probe. One wire was the ground plane of the cantilevers (the middle electrode layer); this was shorted to animal ground. The other electrical path shorted the outer electrodes for all cantilevers together. This simplified design reflects the fact that the perilymph provides a low impedance path between the outer electrodes together when the device is implanted; individual access to each outer electrode is not necessary.

The wires were made of a Pt-Ir alloy, and were each 127μm in diameter and coated with perfluoroalkoxy alkane (PFA) for insulation. All exposed electrical sites on the base of the probe were coated with epoxy for electrical insulation and added mechanical strength. The epoxy provided a high quality electrical seal, but residual stress that formed while the epoxy dried often resulted in degraded electrical quality of the probe contact sites.

The other end of the two wires were connected to a head piece that consisted of two female pin receptacles. The ground wire was jointly soldered to the pin along with a second Pt-Ir wire with a spherical metal ball at its termination, but it was found that a more preferable configuration would be to provide the ground wire with a separately addressable pin, so that the CIAO device can be used as either a transducer or a sensing array during *in vivo* testing. The wire-ball combination, which is shown in
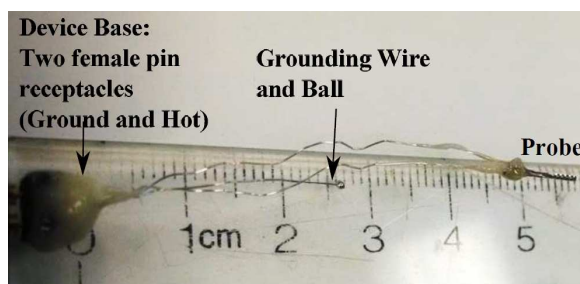
Figure 5.1: An image of the CIAO device construction that was used for *in vivo* testing. The Pt-Ir wires are epoxied to the probe using conductive silver epoxy; the wires are soldered at their other end to two female pin receptacles for external access. The ground wire, with the grounding ball, is co-soldered to the ground pin receptacle, such that there is an electrical connection between animal ground and the middle electrode layer of the probe.

Figure 5.1, is implanted subcutaneously along the neck of the animal, and serves as the connection to animal ground. The head mount pins are coated in epoxy for insulation and mechanical strength. Hard setting epoxies had better electrical insulation than the flexible elastomer (Silastic MDX4-4210) that was initially used.

5.1.2   In Vitro Device Testing Protocol

Prior to the release of probes, the quality of the piezoelectric material is verified using θ-2θ and rocking curve X-ray diffraction (XRD) measurements using a Rigaku Ultima IV X-Ray Diffractometer. All AlN films used for probe measurements displayed low rocking curve full width half maximum (FWHM) of values of 1.61° or lower at the (002) AlN peak. The loss angle for the AlN films, which determines signal to noise level, was measured using a four-point probe station and an Agilent 4284A Precision LCR meter, and was found to be low (0.6%) for all device films. Trace capacitances were measured to be 1-2pF, compared with 8pF cantilever capacitances. The AlN film d_{31} piezoelectric coupling coefficient value was found to be -2.1pm/V, and was obtained by measuring the low-frequency curvature of the cantilever under an applied voltage; this technique is detailed in References [70, 71].
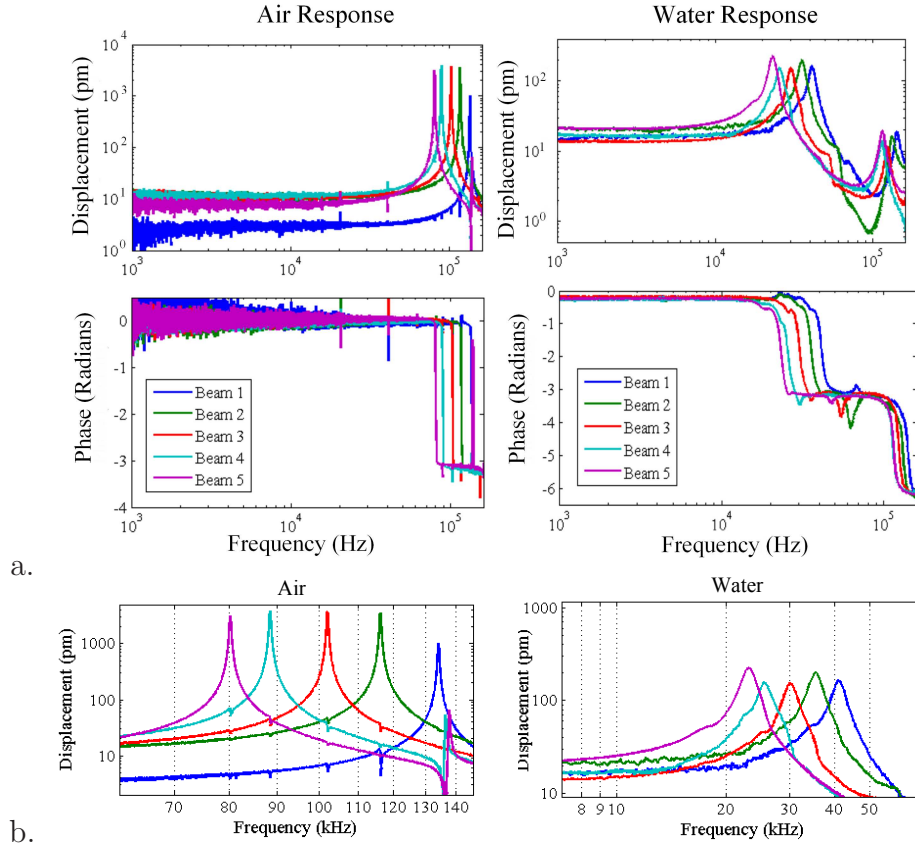
Figure 5.2: Representative magnitude and phase frequency responses of a CIAO device, connected in the method described in Section 5.1.1, in air and water (a). Closeups of the amplitude response are shown in (b).

Air and water resonances of the cantilevers were measured by applying an AC voltage between the center and outer electrodes of each cantilever and measuring the deflection response using a laser Doppler velocimeter [Polytec (Tustin, CA) OFV-303 sensor head] measurement apparatus. A lens is used to focus the laser to a spot size of approximately 30μm, which is then focused on the tip of each cantilever to measure maximum cantilever deflection. Figure 5.2 shows the air and water frequency responses of a representative device for 1V of actuation (with all five beams shorted). Each response curve represents the vibrometer response of each cantilever under this uniformly applied voltage. The cantilever resonant frequencies in air were measured to be 80.3, 88.6, 101.9, 116.3, and 134.2kHz, with Q values of approximately 170.

121

Corresponding resonances of these cantilevers in water were 23.8, 25.4, 30.1, 35.5, and 41.0kHz, respectively, with Q_{3dB} values of approximately 5.8.

5.2 In Vivo Surgical Procedure

Surgical implantation and the subsequent acute *in vivo* testing of a CIAO device was performed on two guinea pigs. The animal surgeries were conducted at the University of Michigan Kresge Hearing Research Institute, and were conducted by Dr. Cameron Budenz and Ms. Debbie Colesa, with the aid of Dr. Yehoash Raphael, Ms. Lisa Kabara, and Dr. Bryan Pfingst. All animal experiments were performed approval from the University of Michigan's institutional animal care and handling committee (UCUCA).

The guinea pigs were deafened 17 and 24 days prior to the date of implantation (first and second implantation, respectively). Each guinea pig was deafened in both ears using a pump infusion of $10\mu L$ of neomycin (5%) over the course of 2 minutes. The infusion was located 0.7mm apical to the round window. The animals showed no signs of inflammation during the recovery period prior to implantation. On the day of implantation, 1-2mL/100g of warm sodium chloride was administered to keep the animals blood pressure elevated. Post deafening ABRs (auditory brainstem response) were then performed on both ears, prior to implantation of the CIAO device. ABR measurements were taken at 4, 12, and 36kHz on each ear, evoking no response at any frequency for any of the four ears tested.

The animals were anaesthetized using 40mg/kg of ketmine and 10mg/kg of xylazine initially, with supplemental doses of ketamine and xylazine administered every hour during the acute testing to ensure that the animal stayed unconscious. Atropine (0.05mg/kg) was also administered to help with respiration in conjunction with the ketamine and xylazine administrations. The animal was placed on a hot water heating pad during the surgery and subsequent testing to maintain body temperature, which

was monitored using a temperature probe. Opthalmic ointment was applied to the eyes to prevent drying, and lidocaine was injected at the incision site to prevent the animal from feeling pain.

Following the pre-implantation ABR measurements, the CIAO device was implanted. An incision was made into the soft tissue over the bulla, exposing the temporal bone and the hole that was used to insert the deafening chemicals. This hole is carefully widened to a diameter of 2-3mm, allowing for easy visualization of the basal section of the cochlea and the round window. A large cochleostomy is then made approximately 1mm from the round window; this site is 1.25-1.5mm in diameter, exposing a large portion of the basal turn of the ST, and also allowing for clear visualization of the BM. The CIAO implant is inserted at an angle that lines up the flats of the cantilevers parallel with the BM. The probe is inserted until resistance is felt, and is then secured using a fascia plug. Maintaining the angle of the implant while the implant is secured is challenging; in the future it is proposed that a microdriver be used to increase accuracy and stability of the probe during positioning. The temporal bone hole is then closed with dental cement.

The head piece of the CIAO implant is then secured to the animals skull. An incision is made from the bulla location to the bregma of the skull, where a the tissue is widened to expose an area large enough for the head piece. The head piece is affixed to the skull using dental cement, and the incision is closed over the Pt/Ir wires of the CIAO implant. Three stainless steel screws were also secured to the skull for EABR (electrical auditory brainstem response) recording.
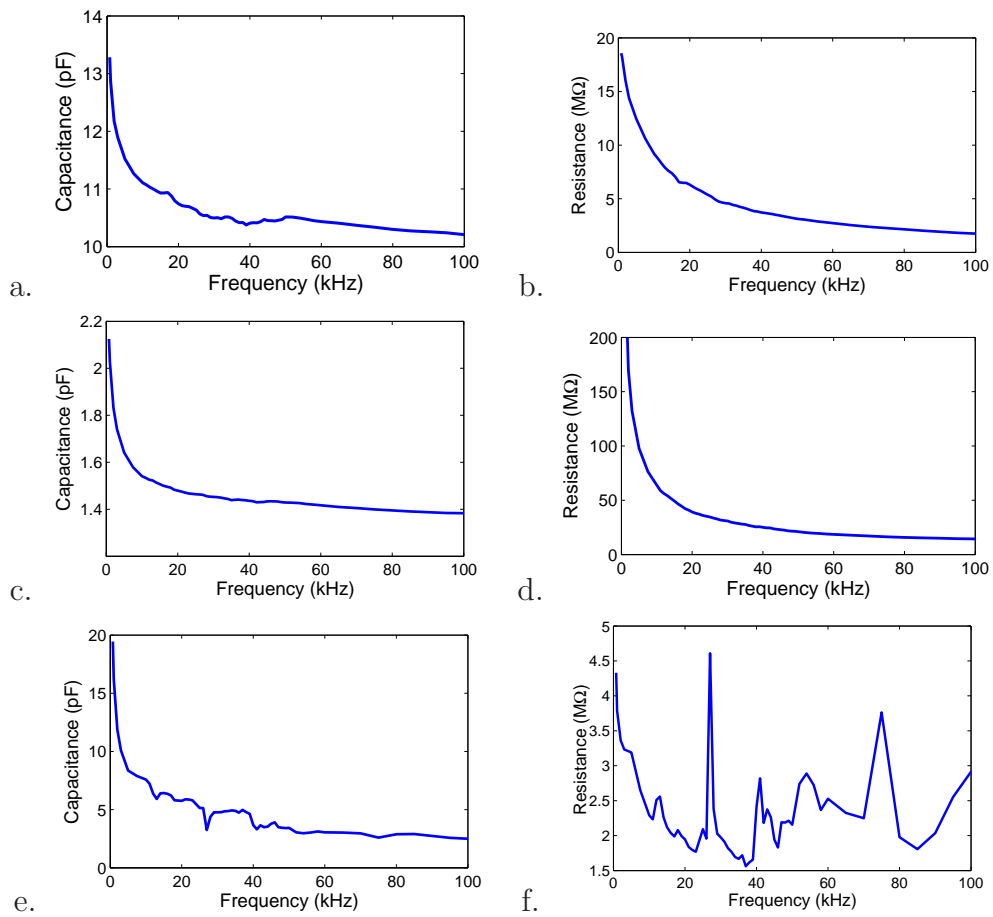
Figure 5.3: The *in vitro* capacitances and resistances of the probe used in the first implantation in air (a,b), water (c,d), and saline (e,f).

124

5.3 Impedance Measurements

5.3.1 In Vitro Measurement

One easily executed metric for establishing the quality of the electrical connections along the probe is to measure the impedance of the probe. For *in vitro* measurements, this is measured in air, water, and saline. In air the expected probe impedance is 40pF (approximately 8pF per cantilever, hooked in parallel), with a large resistance between ground and the outer electrodes (at least 1MΩ). When the probe is submerged in saline (or water that is not deionized) there should be no drop in measured resistance, which is an indication of fluid shorting.

As previously mentioned, the application of epoxy around the silver epoxy joints will compromise the joint integrity, resulting in a shift in the impedance response of the probe. The response of a typical probe, after both epoxy steps, is shown in Figure 5.3. In this Figure, the capacitance and resistance are not the expected smooth curves, but rather show signs of degraded electrical contact. Of particular note is the large test-to-test variation between the capacitance measurements, which would not vary if the electrical connection were secure. In the case of the probe in Figure 5.3, none of the measured capacitances reach the expected capacitance value of 40pF that was measured between the wires extending from the silver epoxy joints prior to the application of the insulative epoxy. All probes were confirmed to have the correct capacitance (40pF) prior to the application of the insulative epoxy. The probe resistance also drops in the saline test relative to the water test, indicating that there is some permeation of the saline ionic content.

For all tests shown in Figure 5.3 the resistance remained over 1MΩ, which is large in comparison to the 5kΩ shunt between contacts that occurs from the conductivity of the animal. In general, the impedance measurements of the implanted CIAO probes demonstrate that electrical connection continues to be a challenge, and that more
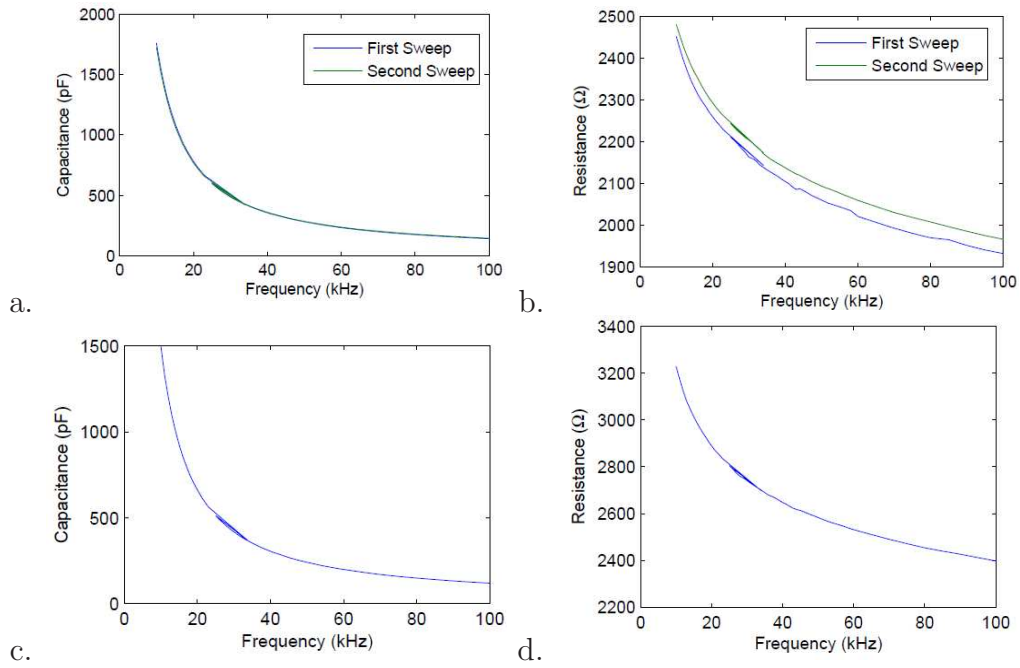
Figure 5.4: The *in vivo* capacitances and resistances of the probes used in the first implantation (a,b) and the second implantation (c,d).

secure methods of electrical connection such as gold ball bump bonding should be pursued in the future.

5.3.2 In Vivo Measurements

In vivo measurements of the impedance of the probes are shown in Figure 5.4 for both implantations. The impedance was measured using an Agilent 4980A LCR meter with a four-point probe configuration with an output limited to 0.1V in order to limit the current that was injected into the animal (larger amounts of current cause strong muscle twitches in the animal); this is shown in Figure 5.4. The impedance was also measured using a 1kHz handheld impedance meter. The capacitance measured *in vivo* for each animal was significantly higher than the capacitance of the probe in air or water, and was measured at approximately 140pF. This capacitance was consistent between implantations, despite the first implant having no cantilevers remaining at the time of measurement. This capacitance arises from the electrode - fluid interface,

126

which is discussed more in Chapter III.

5.4   EABR Protocol

The electrical auditory brainstem response (EABR) is used to establish the health
of the nerve system (VIII cranial nerve). For the EABR of the CIAO device, a si-
nusoid signal (single period at a specified frequency) is applied across the two CIAO
device pins. The signal is constant current; because of this EABR thresholds do not
provide any information about the exposed electrode area because the output voltage
is adjusted to account for changes in electrode size. Therefore, EABR measurements
only provide information about the health and density of the auditory nerves. This
measurement is particularly important for animals that are more than a week post
deafening, as the enervation deteriorates rapidly post deafening. Measured EABR
thresholds from the second implantation are shown in Table 5.1. The thresholds in-
crease as the test frequency is increased, which can indicate either that the animal
had low nerve density at basal locations or that the high frequency pulses do not
have enough power because of the short pulse duration (or both). EABR data is not
available for the first implantation, as no evoked response was ever achieved.

The lowest measured threshold was evoked with 625μA of current at 20kHz. This
threshold is higher than typical in an animal with healthy hearing thresholds; for
comparison, an animal not involved in the CIAO experiments had thresholds be-
tween 100-200μA for the same stimulus that were observed by Ms. Colessa during
(unpublished) behavioral tests. This elevated threshold is not surprising due to the
long period (24 days) between deafening and testing, and it indicates likely degener-
ation of the spiral ganglion. Future implantations can reduce this damage through
the application of neurotrophic factors, such as BDNF [125, 126].

Frequency (kHz)	Threshold (μA)
20	625
25	800
30	900
35	>1000
40	>1000

Table 5.1: Measured EABR Thresholds for Second Implantation.

5.5 Device Placement

The device integrity and placement of both CIAO implants used in *in vivo* tests were assessed using *post mortem* dissections. The goal of these dissections was to confirm that a CIAO implant can be fully implanted into a guinea pig scala tympani without significant damage to the implant cantilevers or the basilar membrane. Correct orientation of the CIAO implant, with intact cantilevers parallel to the BM, was achieved during the second implantation.

5.5.1 First Implantation

Post mortem dissection of the first implantation is shown in Figure 5.5. A left ear was implanted, using a CIAO device with beams pointing to the right (when the tip of the probe is pointing up and the patterned traces are facing the viewer). A close-up of this probe is shown in Figure 5.5a, and the placement of the probe is shown in Figure 5.5b. In this figure, it can be seen that the implant was implanted into the scala tympani, but that the implant punctures the BM such that the location of the most apical two cantilevers would be located in the scala vestibuli, rather than the scala tympani. The implant is also rotated 90° from the desired angle of implantation; in the desired orientation the cantilevers would be parallel to the basilar membrane, rather than parallel to the modiolus, as is the case for this implantation. For clarification, a schematic showing the orientation of the probe as it appears in
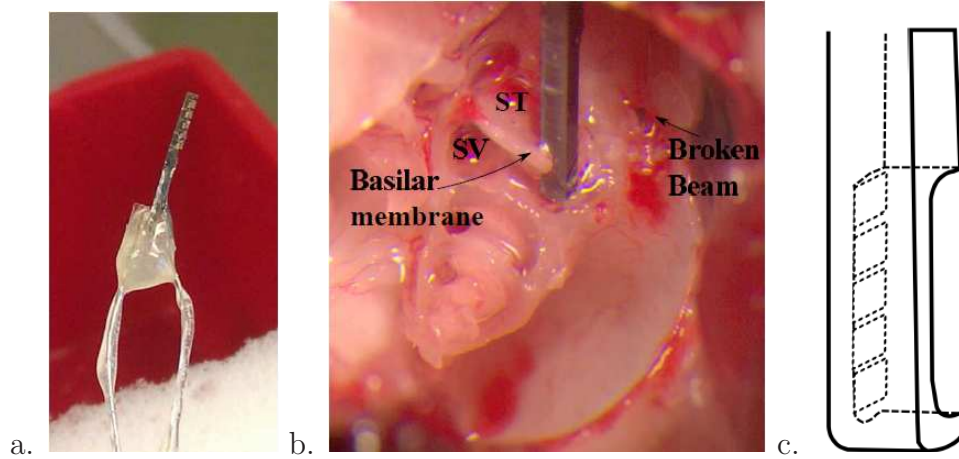
Figure 5.5: The first implanted probe (a). *Post mortem* dissection (b) indicated that the tip of the probe punctured the BM, and that the probe was rotated 90° from desired placement, such that the cantilevers face the mediolus instead of the BM. In this rotation the beams (believed to all be broken during implantation) are obscured by the Si backbone, as shown by the diagram of the probe implant orientation (c).

Figure 5.5b is shown in Figure 5.5c. Although no view angle was achieved where the cantilever sites were visible to confirm that the cantilevers were broken off during implantation for this implantation, it was determined that the cantilevers were not present because of visual cues during implantation and the presence of one broken beam in Figure 5.5b.

5.5.2 Second Implantation

The placement of the second implant is shown in Figure 5.6. This implantation was in a right ear, so the CIAO implant patterning was correspondingly reversed, with the beams facing left, instead of right (when compared to the probe imaged in Figure 5.5a). The probe was implanted at the correct angle, such that the cantilevers were parallel to the basilar membrane. The CIAO implant has no tip sensor to inform when the tip of the probe contacts the BM, so the probe was implanted until the surgeon felt resistance. This resulted in a partial damage to the BM, as part of the

tip of the probe pierced the BM (Figure 5.6a). The most basal cantilever ("Beam 1") broke off during implantation when it contacted the muscle plug that was used to seal up the cochleostomy site (Figure 5.6b). This cantilever also did not fully insert into the scala tympani, indicating that the initial insertion depth estimation of 2.5mm should be reduced to 2mm. This can be accomplished either by the removal of the shortest cantilever, or by redesigning the existing cantilevers to have narrower widths. The middle three beams were intact, though the fourth beam (next to longest) was surrounded by tissue (Figure 5.6b,c). Imaging of the most apical beam was difficult due to insertion depth and the dissection angle of approach, but it appears to be present but shorter than originally fabricated, indicating that part of the cantilever broke off during implantation (Figure 5.6d).

The backbone of the probe was largely intact, but there was damage to the edges of the backbone (shown in the red circles in Figure 5.6e). The damage occurs along a fragile overhang of the probe lithography that extends approximately 20μm off of the edge of the backbone Si, caused by an undercut of the DRIE etch step. The common ground trace, which connects the middle electrode layers of all of the cantilevers together, runs along this overhang location. Therefore, damage to this overhang, such as the damage shown in Figure 5.6e, will sever the ground connection, adding a large series impedance into the electrical path. This results in significantly degraded probe sensitivity, and will be discussed more in the following section.

5.6   Device Performance

In this section the *in vivo* performance of the CIAO device from the second implantation is presented. The device performance is quantified by measuring the voltage output of the device when a pure-tone signal is played at the entrance to the guinea pig ear canal. The noise floor and crosstalk generated from the system were also measured, and found to be insufficient to produce the signal that was measured. Varying
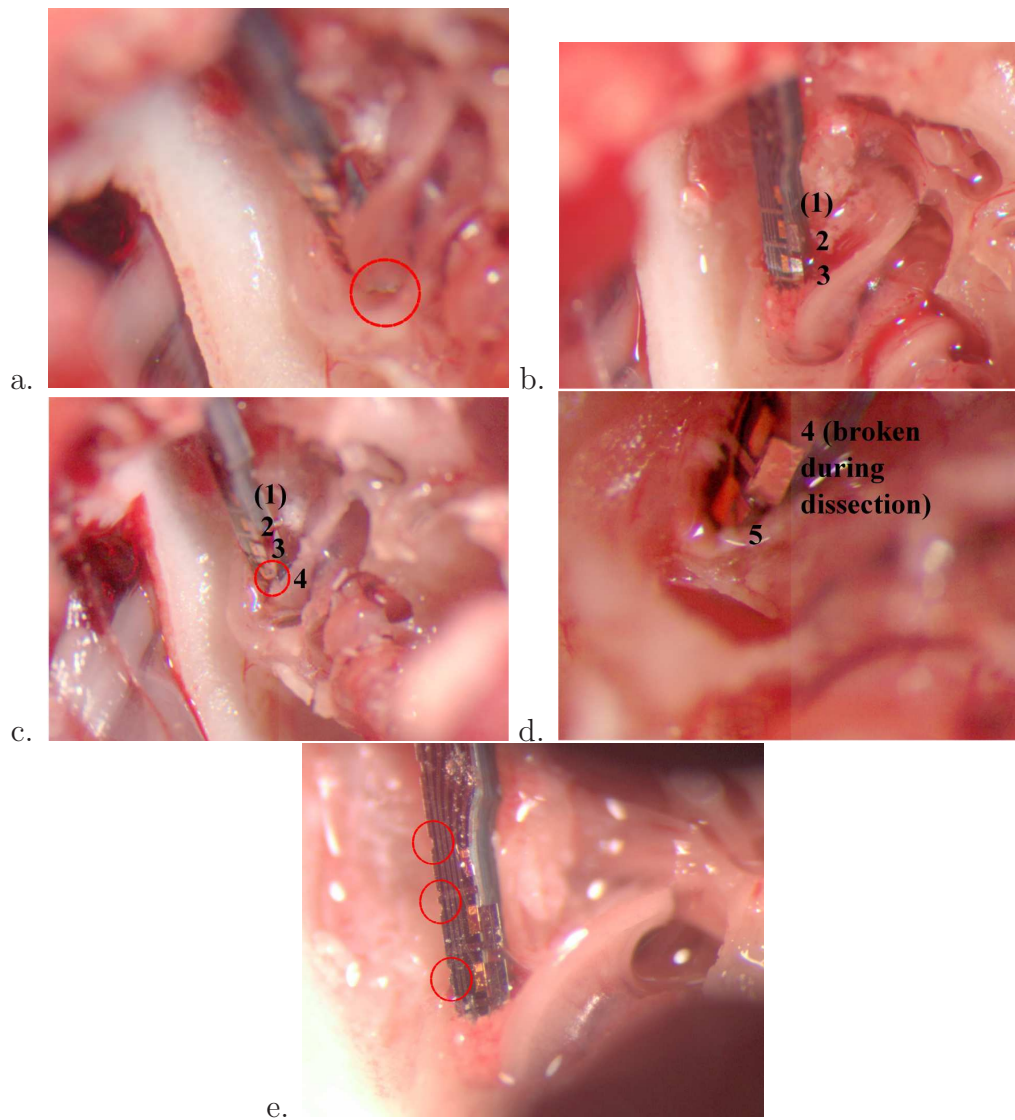
Figure 5.6: *Post mortem* dissection images from the second implantation. Initial opening of the cochlea revealed that the tip of the probe punctured the BM (a), and that the shortest and most basal beam (beam 1) was broken during implantation, but that beams and 3 were intact (b). Further dissection revealed that beam 4 was intact but surrounded by tissue (c), and that beam 5 (most apical, longest) was present but half of its original length (d, beam 4 had been broken off *post mortem*, prior to the image). Finally, the probe suffered damage along its top edges, which damaged the ground trace (e, with the damage circled in red).

131

the input sound pressure level produced a linear output response from the device.

5.6.1 In Vivo Device Testing Setup

The CIAO device performance is measured by comparing the output voltage signal of the implanted CIAO device to the input sound signal that was applied to the ear canal of the guinea pig. This input sound mechanism is the same system and orientation as for the ABR testing, and uses a Tucker-Davis Technologies amplifier and calibrated speaker. Unlike for an ABR response the speaker is set to play a continuous sinusoidal output at a preset frequency. At 9V the output of the speaker ranged between 98dB_{SPL} and 116dB_{SPL} (1.58Pa to 12.6Pa). A SRS 830 lock-in amplifier is used to compare the CIAO signal with the reference signal, the lock-in integrated over a time period of 300ms. The magnitude and phase (if locked) are reported as the device response.

The noise floor measurement was the magnitude response of the lock-in amplifier when the sound source is turned off. This represents any ambient noise in the room, as well as the noise from the cabling and the CIAO device. The lock-in amplifier phase is not recorded, as the noise signal is incoherent. Crosstalk was measured when the speaker turned on and was in position, but the leads that connect to the pin receptacles of the CIAO head piece are instead connected to an exposed $5\text{k}\Omega$ resistor. The $5\text{k}\Omega$ resistance value was chosen to match the 1kHz-measured impedance that is experienced by the CIAO device when it is implanted.

Future CIAO implant testing is to be conducted using an AD621 instrumentation amplifier to provide 40dB of amplification to the CIAO output. The amplifier has flat frequency response across the CIAO measurement range and a noise floor of $9\text{nV}/\sqrt{Hz}$ at 1kHz. The CIAO device response can also be measured using a sweep output function, rather than a point-by-point measurement system. Using a sweep response is advantageous because more data points are achieved in significantly less

measurement time, which reduces the overall time the animal needs to be anaesthetized. However, transient responses of the device need to be considered in this approach.

Device linearity was measured at 20kHz, because this was the frequency that produced the highest CIAO voltage response. The output to the speaker was stepped from 0V to 9V in 1V increments, and the device response was recorded. Phase locking was confirmed for all data points, and remained in the range of 130-134° for data points taken above the crosstalk threshold. Magnitude data were recorded as the maximum and minimum magnitude data points that were presented by the lock-in amplifier over a 5s period (the magnitude data refreshed after every 300ms sampling period).

5.6.2 Measured Device Performance

The measured device response, crosstalk, and noise floor are shown in Figure 5.7. The raw voltage output is given with the blue line; this is uncorrected for the speaker calibration. The measured device response ranged from 0.21μV to 1.99μV of response, with the maximum response achieved at 20kHz. The dashed purple line shows the response when corrected for speaker calibration. This was calculated by adjusting the device output for a reference sound output of 110dB_{SPL}, assuming linear device response. The adjusted response shows a maximum response at 48kHz, and local high sensitivity locations at 28kHz and 38kHz. The measured *in vitro* resonant frequencies of the four implanted cantilevers, as measured in water, are shown with stars, for reference. The noise floor is shown as the red line in Figure 5.7, and never exceeds 0.09μV. The average noise floor value is 0.0724μV. Crosstalk is shown in green in the same figure, and ranges from 0.37μV to 0.67μV.

The device phase response is shown in Figure 5.8. In this Figure, the upper plot shows the raw and compensated response curves, replotted from Figure 5.7. The lower
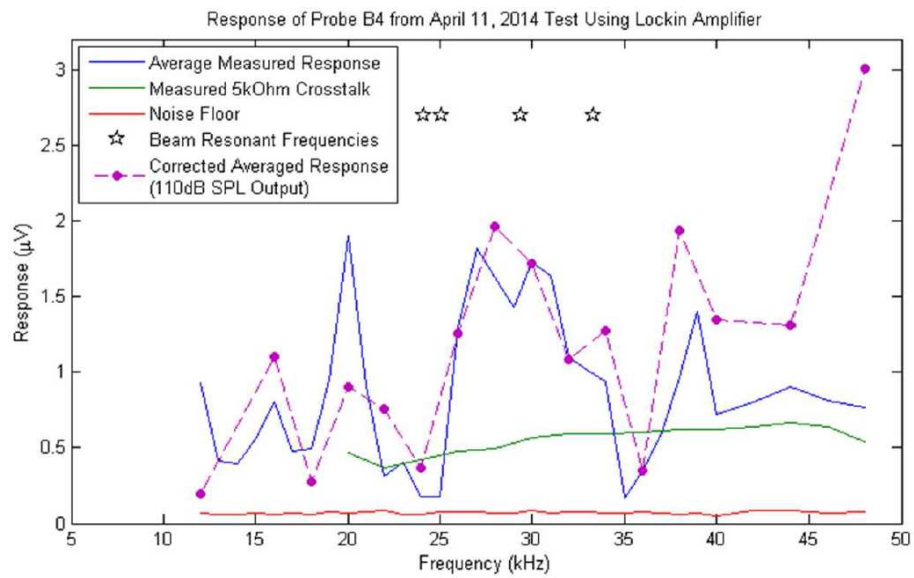
Figure 5.7: The magnitude response of the second implanted CIAO device. The measured device response is shown in blue, the crosstalk is displayed in green, and the noise floor is shown in red. The dashed purple line represents the response that is corrected to represent the device response for a 110dB_{SPL} pressure source at the ear canal. The stars show the *in vitro* measured first resonant frequencies of each of the four intact cantilevers.
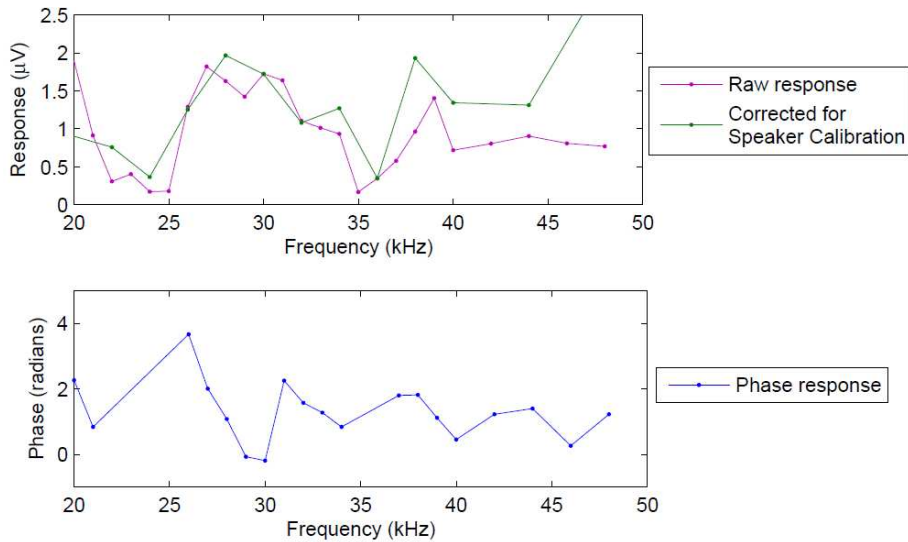
Figure 5.8: The magnitude and phase response of the second implanted device. The purple line represents the uncalibrated magnitude response signal from the device, while the green line is the response compensated for the speaker calibration (these are the same as in Figure 5.7). In the lower plot, the phase response, in radians, is shown in blue. Data points where the device response was below or comparable to the crosstalk level were removed because the phase could not be guaranteed to represent the pure device phase response.

plot shows the phase response, in radians, of the device output. Data points were removed for frequencies where the magnitude response of the device was comparable to the measured magnitude of the crosstalk, as the phase response for those data points could be from the crosstalk, device, or both.

The linearity of the device, measured at 20kHz, is shown in Figure 5.9. In this figure the error bars represent the maximum and the minimum recorded magnitude device responses from the lock-in amplifier; the data point plotted is the average of these two values. A linear fit to the device response is provided with red dashes, and is a good fit to the data (the norm of residuals is 0.13μV). The speaker output was limited to 9V of output because this was the upper limit of functionality without harmonic distortion effects.

135
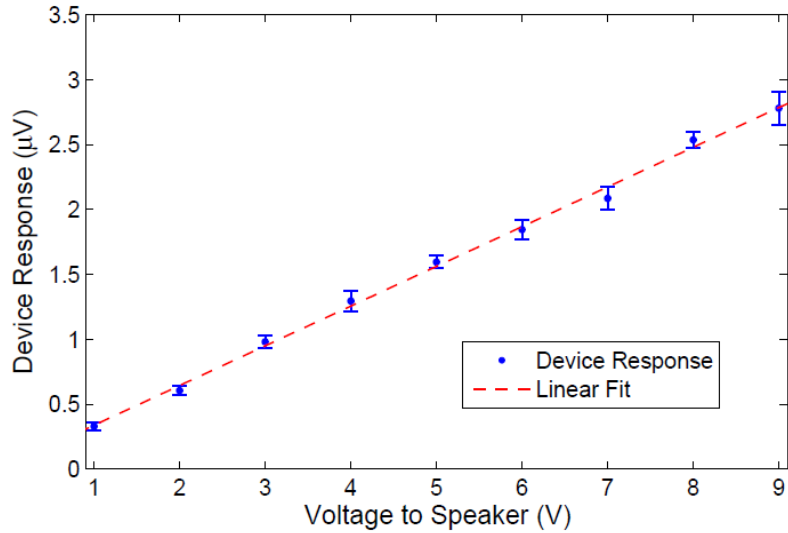
Figure 5.9: The measured linearity of the device response *in vivo* for a 20kHz acoustic signal applied at the entrance of the guinea pig ear canal. The device output increases linearly as the voltage applied to the ear canal speaker is linearly increased. 20kHz was chosen because it was the frequency of maximum device voltage output.

5.6.3 Discussion of Device Performance

The response of the CIAO device, shown in Figure 5.7, is sufficiently high that it cannot have been produced by crosstalk or a noise response. By eliminating these external sources of signal contamination, we propose that the response that was recorded does in fact represent a signal produced by the CIAO device, in response to a pressure applied within the cochlea.

Local areas of high device sensitivity occur at 28khz, 38kHz, and at 48kHz. The high sensitivity responses at 28kHz and 38kHz, however, are most likely due to coupling between the basilar membrane and the cantilevers. This coupling could represent locations where the cantilevers were closest to the BM without limiting its vibration. Alternately, these high-sensitivity frequencies could represent resonances of the cantilevers that were higher than the measured *in vitro* resonances due to beam length reduction within the ST (for example, at least one of the beams was observed in *post*

136

mortem analysis to be significantly shortened from breakage, though it is unknown if this cantilever was the correct length during the acute testing).

The response at 48kHz, on the other hand, is unlikely to be a CIAO device signal. At this drive frequency the speaker output the lowest pressure of any test frequency ($98dB_{SPL}$), and therefore the device response was likely below the crosstalk threshold. The measured device response had a large correction when the response was compensated for the speaker calibration, and it is likely that the high corrected device response is simply crosstalk with the large calibration correction.

The low pressure sensitivity of the implanted device was modeled to be $113\mu V/Pa$. This was derived by first matching the model to the air actuated response, and then using those parameters to model the sensing response and the sensitivity. The sensing response of the CIAO device was not experimentally measured; this should be measured in future tests to confirm the device low frequency sensitivity.

The CIAO device output of $2\mu V$ corresponds to 17.6mPa of sound pressure in the cochlea, as compared with 6.3Pa of input sound pressure. This represents -51dB of sound pressure relative to the input sound pressure. When operating at resonance, the sensitivity increases to $266\mu V/Pa$, which is -39.6dB sound pressure relative to the input pressure. Previous measurements of pressure in the ST for the frequency range of 20-40kHz have recorded a 20dB increase in ST pressure relative to the input ear canal pressure [127, 128]. This discrepancy between previous measurements and our results is most likely due to the damage that occurred during implantation to the ground trace of the CIAO probe. The damage produced several locations where the ground trace was fully severed, introducing a large impedance in the electrical path used to measure the cantilever responses.

Additionally, it was observed that the first cantilever was not fully implanted within the ST, but rather extended outside of the cochleostomy site. Though this

Parameter	Predicted	Measured
Device output at 110dB_{SPL}	0.7-1.7mV (off/on resonance)	0.6-2μV 0.6-2μV
Frequency response	Peaks corresponding to water resonant frequencies (24,25,29,34kHz)	Higher amplitude responses at 28kHz and 38kHz
Linearity	Linear	Linear
Phase response	Phase roll at locations corresponding to water resonances	Too few data points
Noise floor	30μPa/$\sqrt{Hz}$	619μPa/$\sqrt{Hz}$
EABR threshold	100-200μA	625+μA
ABR	No response	No response

Table 5.2: Predicted and achieved *in vivo* CIAO device performance.

cantilever broke off, there remained a gold pad near that beams location, which is used to short the beams top and bottom electrodes together. This pad is electrically open to the surrounding tissue, and in the case of this implantation, was surrounded by a muscle plug that was connected to animal ground, potentially providing an additional shunt between the hot and ground electrical paths.

Finally, a third possible source for this reduced response is a failure of either the silver epoxy wire-probe joint or of the wire-pin receptacle joint. If fluid was able to enter the outer electrode electrical path at one of these joints a new path to animal ground would be established. In this scenario the observed shift in the measured impedance would be very small, as the cantilever capacitance is small compared to the capacitance that is added from any open electrodes having access to an ionized fluid. This scenario only applied when the outer electrode path is compromised. If fluid is able to penetrate to both electrodes a full short will occur, as was observed during the first implantation.

The average measured *in vivo* noise floor of the device (per Hz) was 0.07μV. This corresponds to a pressure of 619μPa. In comparison, the input referred noise for the CIAO device was modeled 30μPa$/\sqrt{Hz}$ (Chapter III), which is well under the noise floor of the rest of the *in vivo* system, so the noise floor inherent to the CIAO device is sufficiently low to not be a concern during testing.

Measurements of the crosstalk aimed to quantify the amount of electromagnetic interference that occurred between the output speaker signal and the wiring that relayed the CIAO device response to the lock-in amplifier. This crosstalk needs to be quantified because the speaker is placed in close proximity to the headpiece and because the speaker runs a significantly higher level signal (up to 9V) than is produced by the CIAO device (2μV). For comparison, the typical amount of crosstalk on a multiplexing NI DAQ card is about 0.1%, which in this case would be 9mV; this crosstalk value would still be 450 times higher than the measured device signal. Given the large

difference in amplitude levels between the drive line and the CIAO device line, it is obvious that great care needs to be taken to ensure that the measured response is not simply crosstalk. The *in vivo* crosstalk was measured to be no higher than 0.67μV for all tested frequencies, which is below much of the CIAO device output level.

There were instances where the measured crosstalk was higher than the measured CIAO device performance, which should be impossible because the lock-in amplifier would simply lock to the crosstalk signal were it dominating. While there has not been any established reason for this discrepancy, it is likely that the explanation for this is that the method used to measure the crosstalk was inadequate, resulting in an overestimation of the crosstalk value. While the 5kΩ resistor was an adequate approximation for the purposes for initial testing, a more precise method for measuring crosstalk in the future is to either plug the speaker (limiting the acoustic output of the speaker) or to remove the speaker from the ear canal (producing a significant change in the acoustic pressure delivered to the implanted CIAO device).

Future *in vivo* device designs will approach crosstalk differently. Instead of two output pins that represent device hot and device ground/animal ground, the design will have three pins: device hot, device ground, and a separate animal ground pin. In this setup the CIAO device can be turned off by shorting the device ground to device hot, but the crosstalk can still be measured between device hot and animal ground. The device can easily be made operational by shorting the device ground back to animal ground. In this way the interference will be better separated from device signal.

The phase response of the device contained too few data points to make any substantial claim about the phase response of the device. It is possible that the approximate shift of π radians at 27-28kHz could correspond to the resonance that appears to occur in the magnitude response. However, the difference in input travel length of the cabling between the reference signal and the device signal was not measured, and could result in a constant phase offset that would produce a phase roll that would only

be visible with more data points. This constant phase difference effect also appears when the phase of the crosstalk signal is off by a constant time delay from the measure signal, as well. In this case, the phase would represent the propagation time between of the sound signal through the ear canal, ossicles, and cochlea to the location of the cantilevers. Finally, the phasing between the cantilevers at different locations in the cochlea will affect the measured phase response, as well. Given all of these potential factors affecting the phase response, it is not possible to determine which factor is dominant in determining the measured phase response shown in Figure 5.8. Establishing the linearity of the device response is important to verify the output signal of the device. AlN bimorph cantilevers have been measured to have linear responses to high sound pressure levels (Littrell measures 3% distortion for sound pressure levels of 128dB$_{SPL}$ [70]). The application of neomycin should also remove nonlinear responses that are observed in healthy cochleae, as well. As a result, the device response to a linear output should be linear; this was verified in Figure 5.9.

5.7   ABR Measurements with the CIAO Device Implanted

After the device performance is measured the animal has a final ABR measurement performed, to test for a device-evoked threshold. No ABR response was detected for either device. However, this result is not surprising. In the second implantation the recorded EABR minimum current needed was 625μA. In order to produce this current, with a measured resistance of 5kΩ, over 3V of potential would need to be provided by the CIAO implant, which is well out of its range of operation (this would require 174dB$_{SPL}$ of pressure across the cantilever). In ideal operation, the CIAO device would output 0.7mV for an incident pressure of 110dB$_{SPL}$, negating any additional pressure amplification that occurs in the ST. Without amplification, this would produce 0.14μA of current. Therefore, a two part response is needed to evoke an ABR response using the CIAO implant: the nerves need to be better

preserved to reduce the threshold requirements to the range of 150μA, and the CIAO device requires at least 60dB of amplification If these requirements are met, it is feasible for the CIAO device to evoke a response.

5.8 Summary of In Vivo CIAO Measurements

Two guinea pigs were implanted with fabricated CIAO devices. The first implantation produced no device response; *post mortem* examination revealed that the probe had punctured through the basilar membrane, was rotated from the preferred direction of insertion, and likely had all cantilevers broken off during implantation. *Post mortem* analysis of the second implantation revealed that the probe was implanted with the correct orientation, but the tip of the probe did puncture the basilar membrane. Four beams were intact, though one beam was encased in tissue and a second was broken in such a way that it ended up being half as long as fabricated. Pre-implantation ABR measurements of the deafened animal confirmed no residual hearing. Once implanted, EABR testing using single phase sine wave signals supplied by the CIAO device electrodes established a 625μA current injection threshold to evoke a response at 20kHz; this threshold grew progressively higher for higher test frequencies. From these tests, it was verified that the animal had no functioning organ of Corti, but that it did have remaining spiral ganglion cells, though the high thresholds of the EABR response demonstrate that the nerve structures were somewhat degraded.

Measurement of the *in vivo* performance of the CIAO device was conducted by comparing the output of the CIAO device to the speaker signal that was played at the entrance to the guinea pig ear canal. The CIAO device output 2μV of signal, corresponding to a reduction of 39.6dB_{SPL} of pressure relative to the input pressure. *Post mortem* examination of the device revealed that this reduction was likely due to damage to the ground trace and a physical connection between the first cantilever

electrode and the surrounding animal tissue. The device output was higher than the measured noise floor of the device and higher than the electromagnetic interference between the speaker and device, indicating that the measured device response was not an artifact from noise or crosstalk.

CHAPTER VI

Conclusions and Future Work

6.1 Summary

This thesis presents a novel design for a completely implantable cochlear implant. This CIAO design utilizes piezoelectric transduction to locally convert sound pressure in the cochlear fluid into electrical signal, negating the need for an external microphone or sound processing unit. This thesis presents the design, fabrication, and testing of a CIAO prototype consisting of a straight backbone with five cantilevers that was designed to reach the basal portion of a guinea pig cochlea, though a fully realized version of this design would be flexible enough to reach apical cochlear locations and contain many cantilever units. When immersed in an ionic fluid such as the cochlear perilymph, the electrical signal of the CIAO cantilevers is transmitted into the cochlear ionic fluid, stimulating the the spiral ganglion.

The CIAO device is designed to match the tonotopic mapping of the cochlea by tailoring each cantilever such that its resonant frequency in water matches the tonotopic location in the cochlea corresponding to its implantation depth. The cantilever frequencies were determined using a model that was developed to describe the response of the cantilevers in a viscous fluid. This model includes consideration for the plane strain cantilever boundary conditions, the multiple AlN and Pt layers, and the viscous fluid environment surrounding the cantilevers. *In vitro* testing of cantilever responses

in air, water, and silicone oil revealed that this model overestimated the mass loading and underestimated the fluid damping experienced by the cantilevers, because the cantilever widths exceeded the conditions under which the model was valid.

The quality of the cantilever AlN was characterized for stress, crystal quality, and piezoelectric response. As the deposition power was increased the AlN stress became more compressive, and the deposition rate increased. Target power was found to have only a small effect on film quality, as measured using X-ray diffraction. AlN films that were deposited in two depositions were found to have significantly higher rocking curve FWHM values than comparable films deposited in a single deposition. TEM analysis of the dual deposition films revealed a line of process induced faults and dislocations at the location of the start of the second deposition. While the stacking disorder resolved within 5-6nm, the resulting dual deposition film did display increased mosaicity and roughness, when compared with the single deposition film; these were the underlying mechanism for the increase in the rocking curve FWHM.

In vivo acute testing of the CIAO device produced a device response signal with a 2μV maximum amplitude, in response to a 116dB_{SPL} sound played at the ear canal of the implanted animal. The measured *in vivo* crosstalk and noise floor were lower than the measured device signal, indicating that the response was not due to signal contamination or noise. The 2μV response was lower than the predicted response, likely because of damage to the ground trace that occurred during implantation. *Post mortem* analysis of the device revealed that four of the five cantilevers were intact during and after the implantation and testing, confirming that the CIAO device can be successfully implanted without the cantilevers breaking off.

In summary, the CIAO device was fabricated successfully, achieving a good match between *in vitro* measured electrical and mechanical performance and the model predictions for device performance. Implantation and acute *in vivo* testing of the device in a guinea pig serves as initial validation in the devices capability to function as a

cochlear implant, though future testing with amplified devices will be needed to confirm that the device can indeed evoke an auditory brainstem response. In contrast to previously published completely implantable CI designs, the device described in this thesis was implanted, sealed, and tested *in vivo*. No part of the device was external to the animal during *in vivo* testing, and no surgical incision or excision was used besides the standard cochleostomy procedure.

6.2 Contributions

The contributions of this thesis are presented in Table 6.1. The primary contribution of this thesis is the design, fabrication, and implantation of an implantable cochlear transducer array that is capable of transducing sense cochlear fluid pressure signals into electrical signals. To date, no group has performed an *in vivo* acute test of a device that, with some degree of amplification, can function as a completely implantable cochlear implant. The CIAO device presented in this thesis produced a response while implanted in an animal for acute testing. The device was completely sealed, with access only available at the head piece on the animals head; the same method will be used for future chronic tests. The ability to fabricate a device that can function in a chronic environment is a crucial step towards the development of a fully implantable cochlear implant.

This thesis also presents contributions towards the characterization of the effect of deposition power on AlN film quality. Factors such as deposition rate, film quality, roughness and nonuniformity were quantified as a function of AlN deposition power. High magnification TEM imaging of AlN films revealed locations of process-induced faults and dislocations in the AlN stacking behavior. In particular, a layer of stacking irregularity was observed at the surface of the AlN film that should be removed for improved crystal quality.

Finally, this thesis provides a comparison between the experimentally measured fre-

Project Goal	Realization
High Quality AlN Deposition	XRD and TEM metrology of the AlN films indicated high quality films with c-axis orientation and low dissipation factors. Film properties were characterized as a function of AC target power. Analysis of the interface that occurs when two AlN depositions are sequentially performed with vacuum broken in between revealed a layer of process induced faults and dislocations that resolved within 5-10nm of the start of the second deposition.
Accurate model that predicts water response	A model of the device response in viscous fluid was developed. The model assumed long and narrow beams; this did not match the designed CIAO geometry. As a result the model overpredicted the fluid mass loading effects and underpredicted the fluid damping experienced by the cantilevers.
Cabling with separate electrical access to each CIAO cantilever	Not achieved. Monolithic integration of cabling and probes produced devices with poor or missing electrical contact. Bonding techniques between cables and probes that are fabricated separately is in development, but was not achieved in the scope of this thesis. Silver epoxy was used to provide access to one common ground trace and one common electrical path to all outer cantilever electrodes; this was used during *in vivo* testing.
In vivo testing	Two acute *in vivo* tests were performed, consisting of pre-implantation ABR to ensure deafness, implantation, EABR to measure nerve health, measurement of the device response to sound introduced at the animal's ear canal, and an ABR to test if the CIAO device produced sufficient current to evoke an auditory brainstem response. Device was completely sealed off during implantation; access to the device for testing was only available through two pin inputs located at the top of the animal's head. Implantation method was compatible with future chronic *in vivo* testing.
In vivo device response of 1.4mV for a 116.4dB$_{SPL}$ incident sound (at ear canal, 20kHz)	Maximum achieved signal was 1.99μV device response at 20kHz for an 13.2Pa (116.4dB$_{SPL}$) sound source at the ear canal. Performance was low due to damage to the common ground trace, possible shorting between the outer electrodes and animal ground from contact with the fascia plug used to seal the cochleostomy site, and possible detachment of the electrical contacts at the silver epoxy joint at the base of the probe.
Linear *in vivo* device response	Linear changes in device response were confirmed for a linear change in voltage to the input speaker.

Table 6.1: A list of the desired CIAO project goals and the corresponding achievements covered in the thesis.

quency response of the CIAO cantilevers and the response predicted by the Sader model describing the response of a cantilever in a viscous fluid [86]. In this comparison the model was modified to represent a multimorph cantilever made of Pt and AlN under plane strain conditions. The model was found to predict the resonant frequencies of wide cantilevers in water rather poorly; there was a 50% discrepency between the model and experimental measurements of the first bending mode frequency. The accuracy of the model was limited because the width to length ratio of the measured cantilevers exceeded the conditions under which the model operates.

6.3   Application to Humans

The ultimate goal of the CIAO implant project is to create an implant that functions in humans. A schematic of the human CIAO design is shown in Figure 6.1. This design is made flexible by a mass-spring system, where cantilevers are housed on blocks and connected by metal meanders. Amplification and stimulation would ideally be performed locally on each block. A parylene ribbon cable extends along each block, providing the necessary electrical connections to each site (power for the amps, back telemetry, etc.).

One concern about the future CIAO device is whether proper cantilever placement can be achieved, such that phasing and amplitude modulation is avoided while still allowing for sufficient space between each cantilever to allow for the amplifying units and the flexible meanders. To address this, an example CIAO design was created using 15 cantilevers that spanned the frequency range of 1.8kHz to 12.2kHz. The summed magnitude and phase response of all of the cantilevers is shown in Figure 6.2a. This summed response indicates that the cantilevers can be designed such that the summed response is smooth.

For this design, each cantilever was 100μm wide, and the lengths spanned between 80μm and 200μm. These lengths are acceptable in the human cochlea, where the

148
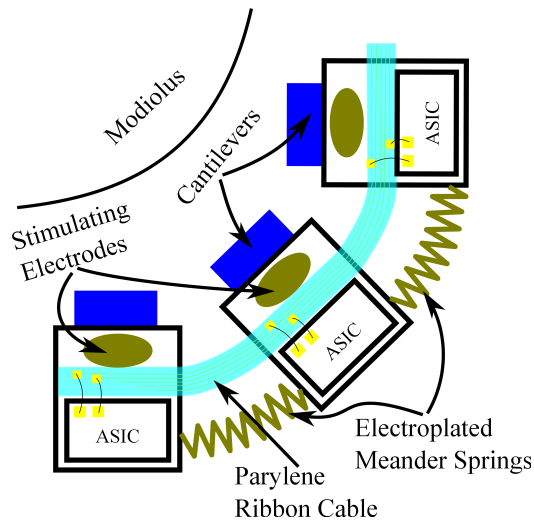
Figure 6.1: A proposed design for a flexible CIAO device with integrated amplification.

width of the ST does not drop below 1mm for the basal 24mm [129]. This width allows for the integration of both a cantilever and a block with an optional stimulating electrode and/or integrated amplifier. The AlN layers were reduced in the model to 200nm thick; this thickness is possible, but will be of lower quality. Figure 6.2b shows the frequency location of each cantilever in this hypothetical array, as a function of the corresponding tonotopic location along the BM (from the apex). This mapping was derived from the Greenwood frequency place map [69]. This figure demonstrates that cantilevers can be sufficiently separated to allow the space needed for Si blocks, small amplifiers, and meanders. Inter-cantilever spacing for this hypothetical array ranges between 800μm and 1.1mm. Additionally, it is possible for multiple cantilevers to be placed on each block, allowing for the potential for the device to follow the low frequency envelope of the BM.

In summary, the CIAO implant can be designed to fit the human cochlea. Cantilevers can be spaced such that flexible meanders, stimulating electrodes, and integrated amplification blocks could all be incorporated into a flexible implant design. Summed magnitude and phase responses of the cantilevers show that the cantilever resonances
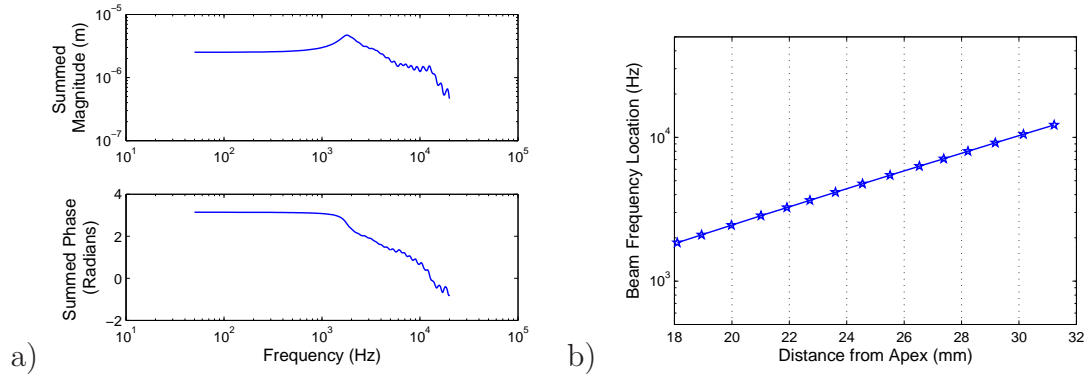
Figure 6.2: The summed magnitude and phase responses of a hypothetical CIAO device for the human cochlea (a). Cantilevers are 100μm wide, with 200nm thick AlN layers. Lengths span from 80μm to 200μm. A map showing each cantilever's resonant frequency, mapped against its corresponding insertion depth (measured from the apex, in mm), shows that the spacing between cantilevers spans from 800μm to 1.1mm, leaving adequate room for both blocks to house the cantilevers and a flexible meander.

can be tuned in a spacing that minimizes comb filtering effects between cantilevers, allowing for a smooth phase response. Finally, this design easily fits into the human ST, which was measured to be at least 1mm wide in the portions of the ST that are being considered.

6.4 Future Work

While the initial testing of the CIAO device was positive, there remains significant work that is needed before the CIAO implant would be appropriate for commercialization and general use. Table 6.2 lists a summary of future necessary action steps for the CIAO project; a few of the most important steps are also further described in the enumeration that follows.

- Integration of amplification. An application specific integrated circuit (ASIC) was developed by Dr. Angelique Johnson for integration with future CIAO generations. This amplifier should be integrated with future CIAO devices, in order to amplify the device response closer to the current threshold necessary

Future Project Steps	Description
Improved cable and electrode materials	Parylene C was chosen because it is easily deposited, waterproof, and biocompatible. However, specific formulations of other materials such as silicone and polyimide have improved flexibility and metal adhesion. Pt was excellent for initial CIAO prototype electrodes because it has relatively high charge injection and is easy to deposit. However, other materials such as IrO, Pt black, and PtIr have improved current injection, and should be considered as alternatives.
Robust bonding	The attachment of the cable to the probes needs to be both mechanically and electrically robust. The silver epoxy technique used in this thesis had significant problems with maintaining good electrical contacts, and epoxy was required to strengthen the contact sites mechanically. Future work should focus on a more robust method of attachment, such as ball bonding.
Improved modeling of resonances	The modified Sader model underpredicted the first mode of the cantilever response because the cantilever geometry did not fit the model conditions that the beams be narrow and long. More accurate CAD modeling is needed to better predict the resonant frequencies for future CIAO designs.
Amplification	As modeled, the CIAO device will require 60-80dB of amplification to produce enough current to evoke an ABR response. This can be achieved by integrating an ASIC amplifier block at the base of the CIAO device, or by integrating small amplifiers along the length of the CIAO device.
Adjustable gain	Commercial CIs adjust electrode site gain to account for non-uniform nerve density and implant placement; this allows for better sound comprehension for the patient. Amplification to the CIAO design should ultimately also have this ability to adjust channel gain.
Miniaturization of cantilevers	In amplified models the cantilevers need to be small to minimize real estate, using significantly thinner AlN layers. The cantilevers also do not need to have the middle electrode connect to animal ground; instead the outer electrodes can connect to animal ground and the middle electrode signal can be amplified and sent to a separate stimulating electrode.
Flexibility	The CIAO device must ultimately be flexible to access lower frequencies. One proposed method for this is to design a mass-spring system that would have a prescribed in-plane flexibility that optimizes how the device curls around the modiolus.
Chronic *in vivo* tests	Long-term guinea pig tests (1 week-1 month) are necessary to ensure that the CIAO device can be implanted without a buildup of fibrotic tissue or signs of other inflammatory response.
Testing in larger animal models	As the CIAO device becomes flexible, larger animal models will be necessary, as the upper turns of the guinea pig cochlea are simply too small (250μm). Animals such as rabbits or cats have larger scala tympanis, and are therefore better candidates for CIAO implants that access more apical locations.

Table 6.2: A list of the necessary future steps for the design of the CIAO implant

to evoke an ABR response; a preliminary prototype of this design is shown in Figure 6.3. Ultimately amplification should be integrated more fully into the device, with amplifiers located either in the middle ear or distributed along the probe in the scala tympani.

- Flexibility. The CIAO device prototype presented in this thesis was built on a straight silicon backbone that was only capable of accessing the basal straight section of the cochlea. In the future, the CIAO device will require flexibility to achieve a greater insertion depth. This is most likely achieved using a mass-spring configuration, where one or more cantilevers are located on a series of silicon blocks, which are connected by electrical cabling and meander springs, as drawn in Figure 6.1.

- Chronic *in vivo* testing. This thesis presents acute measurements of device response, but the device was not fully integrated with the cabling that is necessary for longer term studies. In order to achieve this the fabricated cabling needs to be reliably attached to the CIAO probes. This bonding needs to be mechanically and electrically robust. Additionally, the cabling needs to be insulative and waterproof for *in vivo* testing. However, the CIAO device and cabling are designed for chronic testing, so no major modifications to the CIAO design or fabrication process are necessary for chronic testing.

- Separation of the AlN cantilevers and the stimulation electrodes. Future design of amplified CIAO devices can approach the integration of amplification in two ways: either the sensed signal can be fed from the cantilever to the amplifier and then back to the cantilever in a feedback loop, or a separate array of stimulation electrodes can be used. Both methods have challenges. In the case of a feedback loop the cantilevers will need a large thickness of electrode material, as stimulating electrodes dissolve over time. The required extra metallization will

152
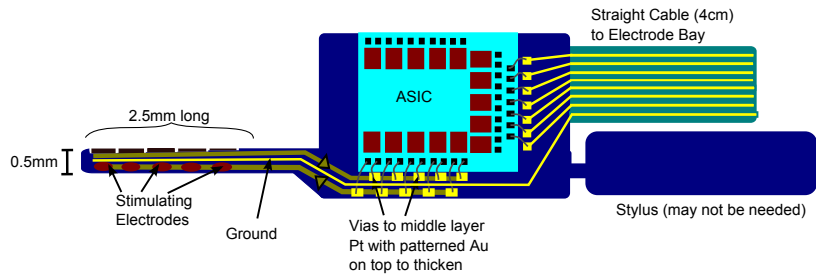
Figure 6.3: A proposed design for a CIAO device incorporating an ASIC amplifier array.

likely reduce the sensitivity of the cantilevers by a significant amount, so the feedback option is not optimal. The use of a separate array of stimulation electrodes avoids the need to apply thick metallization to the sensing cantilevers, but it does require close proximity between the sensing and amplified response traces, potentially producing significant crosstalk. However, crosstalk can be minimized with careful placement of the amplification units.

BIBLIOGRAPHY

BIBLIOGRAPHY

[1] B. Blaus. Anatomy of the ear. Online, 2013.

[2] B.Blaus. Internal ear anatomy. Online, 2013.

[3] Basilar membrane: analysis of sound frequencies. Online, 1997.

[4] Cochlea: cross section. Online, 1997.

[5] Ear: organ of corti. Online, 1997.

[6] B. Blaus. Cochlear implant. Online, 2013.

[7] M Tykocinski, LT Cohen, and RS Cowan. Measurement and analysis of access resistance and polarization impedance in cochlear implant recipients. *Otology & Neurotology*, 26:948–956, 2005.

[8] Georg von Bekesy. *Experiments in Hearing.* McGraw-Hill, 1960.

[9] Georg von Bekesy. Concerning the pleasures of observing, and the mechanics of the inner ear. In *Nobel Lecture*, 1961.

[10] MA Ruggero, NC Rich, A Recio, SS Narayan, and L Robles. Basilar-membrane responses to tones at the base of the chinchilla cochlea. *J. Acoust. Soc. Am*, 101(4):2151–2163, 1997.

[11] L Robles and MA Ruggero. Mechanics of the mammalian cochlea. *Physiol. Rev.*, 81(3):1305–1352, 2001.

[12] WS Rhode. Observations of the vibrations of the basilar membrane in squirrel monkeys using the mossbauer technique. *J. Acoust. Soc. Am*, 48:1218–1231, 1971.

[13] W.F. House and J. Urban. Long term results of electrode implantation and electronic stimulation of the cochlea in man. *Ann Otol Rhinol Laryngol*, 82:504–1973, 1973.

[14] S.B. Brummer and M.J. Turner. Electrical stimulation of the nervous system: The principle of safe charge injection with noble metal electrodes. *Bioelectrochemistry and Bioenergetics*, 2(1):13–25, 1975.

[15] F.G. Zeng, S. Rebscher, W. Harrison, X. Sun, and H. Feng. Cochlear implants: System design, integration, and evaluation. *IEEE Reviews in Biomedical Engineering*, 1:115–142, 2008.

[16] F.G. Zeng. Cochlear implants: Why don't more people use them? *The Hearing Journal*, 60(3):48–49, 2007.

[17] J. Sarant. Cochlear implants in children: A review. *Intech Open*, 2012.

[18] C. Daniel Geisler. *From Sound to Synapse*. Oxford University Press, 1998.

[19] C. Dallos. *The Cochlea, Volume 8 of Springer handbook of auditory research*. Springer,, 1996.

[20] G von Bekesy. *Experiments in Hearing*. McGraw-Hill, 1960.

[21] A. Tubis S Koshigoe. *Mechanics of Hearing*. Delft Univ. Press, 1983.

[22] C Cancelli, S D'Angelo, M Masili, and R Malvano. Experimental results in a physical model of the cochlea. *J. Fluid Mech.*, 153:361–388, 1985.

[23] TP Lechner. A hydromechanical model of the cochlea with nonlinear feedback using pvf2 bending transducers. *Hearing Research*, 66:202–212, 1993.

[24] G Zhou, L Bintz, DZ Anderson, and KE Bright. A life-sized physical model of the human cochlea with optical holographic readout. *J. Acoust. Soc. Am*, 93(3):1516–1523, 1993.

[25] D Haronian and N MacDonald. A microelectromechancis based artificial cochlea (membac). *IEEE Transducers*, pages 708–711, 1995.

[26] S Ando, K Tanaka, and M Abe. Fishbone architecture: An equivalent mechanical model of cochlea and its application to sensors and actuators. *IEEE Transducers*, pages 1027–1030, 1997.

[27] R White and K Grosh. Microengineered hydromechanical cochlear model. *Proc. National Academy of Sciences*, 102(5):1296–1301, 2005.

[28] F Chen, HI Cohen, TG Bifano, J Castle, J Fortin, C Kapusta, DC Mountain, A Zosuls, and AE Hubbard. A hydromechanical biomimetic cochlea: Experiments and models. *J. Acoust. Soc. Am*, 119(1):394–405, 2006.

[29] MJ Wittbrodt, CR Steele, and S Puria. Developing a physical model of the human cochlea using microfabrication methods. *Audiology and Neurotology*, 11:104–112, 2006.

[30] M Bachman, FG Zeng, T Xu, and GP Li. Micromechanical resonator array for an implantable bionic ear. *Audiology and Neurotology*, 11:95–103, 2006.

[31] S Hur, SQ Lee, and HS Choi. Fabrication and characterization of pmn-pt single crystal cantilever array for cochlear-like acoustic sensor. *Jour. Mech. Sci. Tech.*, 24:181–184, 2010.

[32] T Inaoka, H Shintaku, T Nakagawa, S Kawano, H Ogita, T Sakamoto, S Hamanishi, H Wada, and J Ito. Piezoelectric materials mimic the function of the cochlear sensory epithelium. *Proceedings of the National Academy of Sciences*, 108(45):1839018395, 2011.

[33] S. Kim, W.J. Song, J. Jang, J.H. Jang, and H. Choi. Mechanical frequency selectivity of an artificial basilar membrane using a beam array with narrow supports. *J. Micromech. Microeng.*, 23:1–13, 2013.

[34] Deafness and hearing loss: Fact sheet number 300. Online, February 2013.

[35] C. C. Morton and W.E. Nance. Newborn hearing screening - a silent revolution. *New England Journal of Medicine*, 354(20):2151–2164, 2006.

[36] H. L. Rehm, R. E. Williamson, M.A. Kenna, D.P. Corey, and B. R. Korf. *Understanding the Genetics of Deafness: A Guide for Patients and Families.* Harvard Medical School Center for Hereditary Deafness.

[37] S. M. Antonio, A. D. Meyers, and B. Strasnick. Syndromic sensorineural hearing loss. Online, April 2012.

[38] J. Holt, S. Hotto, and K. Cole. Demographic aspects of hearing impairment: Questions and answers. Online, 1994.

[39] R.C. Bilger. Psychoacoustic evaluation of present prostheses. *Ann Otol Rhinol Laryngol Suppl*, 3 Pt 3 Suppl 38:92–104, 1977.

[40] R. Chaikof, M. Chaikof, and E. Rosenzweig. Brand comparison chart - choosing a cochlear implant brand. Online, 2013.

[41] National Institute on Deafness and Other Communication Disorders. Cochlear implants. Website, July 2011.

[42] FDA approves first implantable hearing device for adults with certain kind of hearing loss. Online, 2014.

[43] J. T. Rubinstein. How cochlear implants encode speech. *Otolaryng Head Neck*, 12:444–448, 2004.

[44] D. Riss, J. Hamzavi, A. Selberherr, A. Kaider, M. Blineder, V. Starlinger, W. Gstoettner, and C. Arnoldner. Envelope versus fine structure speech coding strategy: a crossover strategy. *Otol. Neurotol.*, 32:1094–1101, 2011.

[45] C. Fielden, K. Kluk, and C. McKay. Place specificity of monopolar and tripolar stimuli in cochlear implants: the influence of residual masking. *J. Acoust. Soc. Am.*, 133(6):4109–4123, 2013.

[46] R. Saba. *Cochlear implant modeling: stimulation and power consumption.* PhD thesis, University of Southampton, 2012.

[47] T. Francart and H. McDermott. Psychophysics, fitting, and signal processing for combined hearing aid and cochlear implant stimulation. *Ear and Hearing*, 34(6):685–700, 2013.

[48] C. C. Finley and M. W. Skinner. Role of electrode placement as contributor to variability in cochlear implant outcomes. *Otol. Neurotol.*, 29(7):920–928, 2008.

[49] J. L. Pinyon, S. Tadros, K. E. Froud, A. C. Wong, I. T. Tompson, E. N. Crawford, M. Ko, R. Morris, M. Klugmann, and G. D. Housley. Close-field electroporation gene delivery using the cochlear implant electrode array enhances the bionic ear. *Sci Transl Med.*, 6(233):233RA54, 2014.

[50] S. Shibata, S. Cortez, L. Beyer, J. A. Wiler, A. D. Polo, B. E. Pfingst, and Y. Raphael. Transgenic bdnf induces nerve fiber regrowth into the auditory epithelium in deaf cochleae. *Exp. Neurol.*, 223(2):464–472, 2010.

[51] A. Kral and A. Sharma. Developmental neuroplasticity after cochlear implantation. *Trends. Neurosci.*, 35(2):111–122, 2012.

[52] R. Briggs, H. Eder, P. Seligman, R. Cowan, K. Plant, J. Dalton, D. Money, and J. Patrick. Initial clinical experience with a totally implantable cochlear implant research device. *Otology & Neurotology*, 29(2):114–119, 2008.

[53] D. Young, M. A. Zurcher, M. Semaan, C. A. Megerian, and W. H. Ko. MEMS capacitive accelerometer-based middle ear microphone. *IEEE Trans. on Biomed.Eng.*, 59(12):3283–3292, 2012.

[54] M. Yip, R. Jin, H. Nakajima, K. Stankovic, and A. P. Chandrakasan. A fully-implantable cochlear implant SoC with piezoelectric middle-ear sensor and energy-efficient stimulation in 0.18um hvcmos. *Proc. 2014 IEEE Internat. Solid-State Circuits*, page 312, 2014.

[55] S. Kim, W. Song, J. Jang, and H. Choi. Mechanical frequency selectivity of an artificial basilar membrane using a beam array with narrow supports. *J. Micromech. Microeng.*, 23:1–13, 2013.

[56] H Shintaku, T Nakagawa, D Kitagawa, H Tanujaya, S Kawano, and J Ito. Development of a piezoelectric acoustic sensor with frequency selectivity for artificial cochlea. *Sensors Actuators A*, 158:183–192, 2010.

[57] N Mukherjee and R.D. Roseman. Considerations in the development of a piezoelectric transducer cochlear implant. *Mat. Res. Soc. Symp. Proc.*, 604:79–84, 2000.

[58] W. Kim, S. Hur, S. Oh, J. Chung, and Y. Cho.

[59] A.J. Lupin. Cochlear implant., 1994.

[60] J.J. Jacobs. Cochlear implant auditory prosthesis, 1991.

[61] Tracy E. Bell, Kensall D. Wise, and David J. Anderson. A flexible microma-chined electrode array for a cochlear prosthesis. *Sensors and Actuators*, A. 66:63–69, 1998.

[62] K.D. Wise, P.T. Bhatti, J. Wanga, and C.R. Friedrich. High-density cochlear implants with position sensing and control. *Hearing Research*, 242:2230, 2008.

[63] PT Bhatti, BY Arcand, J Want, NV Butala, CR Friedrich, and KD Wise. A high-density electrode array fo a cochlear prosthesis. In *The 12th International Conterence on Solid State Sensors. Actuators and Microsystem*, 2003.

[64] PT Bhatti and KD Wise. A 32-site 4-channel high-density electrode array for a cochlear prosthesis. *IEEE Journ. Solid-State Cir.*, 41:2965–2973, 2006.

[65] B. Y. Arcand, P. T. Bhatti, N. V. Butala, J. Wang, C. R. Friedrich, and K. D. Wise. Active positioning device for a perimodiolar cochlear electrode array. *Microsystem Technologies*, 10:478483, 2004.

[66] J Wang, M. Gulari, P.T. Bhatti, B. Y. Arcand, K. Beach, C.R. Friedrich, and K. D. Wise. A cochlear electrode array with built-in position sensing. In *18th IEEE International Conference on Micro Electro Mechanical Systems*, pages 786–789, 2005.

[67] A. Johnson. *An active thin-film cochlear electrode array with monolithic backing and curl.* PhD thesis, University of Michigan, 2011.

[68] A. Johnson and K. Wise. A self-curling monolithically-backed active high-density cochlear electrode array. *Proc. MEMS Conf.*, pages 914–917, 2012.

[69] D. D. Greenwood. A cochlear frequency-position function for several species - 29 years later. *J. Acoust. Soc. Am.*, 87(6):2592–2605, 1990.

[70] R. Littrell. *High Performance Piezoelectric MEMS Microphones.* PhD thesis, University of Michigan, Ann Arbor, 2010.

[71] R Littrell and K Grosh. Modeling and characterization of cantilever-based MEMS piezoelectric sensors and actuators. *Journal of Microelectromechanical Systems*, 21(2):406–413, 2012.

[72] L. Geddes and R. Roeder. Criteria for the selection of materials for implanted electrodes. *Ann. Biomed. Eng.*, 31:879–890, 2003.

[73] S. F. Cogan. Neural stimulation and recording electrodes. *Annu. Rev. Biomed. Eng.*, 10:275–309, 2008.

[74] K Roach. *Electrochemical Models for Electrode Behavior in Retinal Prostheses.* PhD thesis, Massachusetts Institute of Technology, 2003.

[75] B. A. Murphy. *A biocompatibility study of aluminum nitride packaging for cortical implants.* PhD thesis, Wayne State University, 2008.

[76] W. Franks, I. Schenker, P. Schmutz, and A. Hierlemann. Impedance characterization and modeling of electrodes for biomedical applications. *IEEE Trans. Biomed. Eng.*, 52(7):1295–1302, 2005.

[77] JD Weiland and DJ Anderson. Chronic neural stimulation with thin-film, iridium oxide electrodes. *IEEE Trans. Biomed. Eng.*, 911-918:47, 2000.

[78] M. Dubios and P. Muralt. Stress and piezoelectric properties of aluminum nitride thin films deposited onto metal electrodes by pulsed direct current reactive sputtering. *Jour. Appl. Phys.*, 89(11):6389–6395, 2001.

[79] J. Meyer, T. Stieglitz, O. Scholz, W. Haberer, and J. Beutel. High density interconnects and flexible hybrid assemblies for active biomedical implants. *IEEE Trans. Adv. Packag*, 24(3):366–374, 2001.

[80] F. Wu, L. Tien, F. Chen, D. Kaplan, J. Berke, and E. Yoon. A multi-shank silk-backed parylene neural probe for reliable chronic recording. *Proc. IEEE Solid-State Sens., Actuat., and Microsys.*, 2013.

[81] B. A. Auld. *Acoustic Fields and Waves in Solids.* Wiley, 1973.

[82] M. Krommer and H Irschik. On the influence of the electric field on free transverse vibrations of smart beams. *J. Smart Mater. Struct*, 8:401–410, 1999.

[83] H. Hosaka and K. Itao. Coupled vibration of microcantilever array induced by airflow force. *Transactions of the ASME*, 124:26–32, 2002.

[84] E.O. Tuck. Calculation of unsteady flows due to small motions of cylinders in a viscous fluid. *Jour. Eng. Math.*, 3(1):29–44, 1969.

[85] M. Martin and B. Houston. Frequency response of cylindrical resonators in a viscous fluid. *Jour. Vibration and Acoustics*, 123:031009:1–6, 2011.

[86] JE Sader. Frequency response of cantilever beams immersed in viscous fluids with applications to the atomic force microscope. *J. Appl. Phys.*, 84:64–76, 1998.

[87] T. Naik, EK Longmire, and SC Mantell. Dynamic response of a cantilever in liquid near a solid wall. *Sensors Actuators*, 102A:240–254, 2003.

[88] I. Dufour, E. Lemaire, B. Caillard, H. Debeda, C. Lucat, S. Heinrich, F. Josse, and O. Brand. Effect of hydrodynamic force on microcantilever vibrations: Applications to liquid-phase chemical sensing. *Sensor Actuat. B-Chem,*, 192:664–672, 2014.

160

[89] A.K. Pandey and R. Pratap. Effect of flexural modes on sqeeze film damping in mems cantilever resonators. *J. Micromech. Microeng*, 17:2475–2484, 2007.

[90] S.H. Crandall. The role of damping in vibration theory. *J. Sound Vib.*, 11(1):3–18, 1970.

[91] N.W. Hagood and A. von Flotow. Damping of structural vibrations with piezoelectric materials and passive electrical networks. *Journal of Sound and Vibration*, 146(2):243–268, 1991.

[92] S. Shah, A. Hines, D. Zhou, R. Greenberg, M. Humayun, and J. Weiland. Electrical properties of retinal-electrode interface. *J. Neural. Eng.*, 4:S24–S27, 2007.

[93] S. Voss and C. A. Shera. Simultaneous measurement of middle-ear input impedance and forward/reverse transmission in cat. *J. Acoust. Soc. Am*, 116(4):2187–2198, 2004.

[94] C Vancura, I Dufour, SM Heinrich, F Josse, and A Heirlemann. Analysis of resonanting microcantilevers operating in a viscous liquid environment. *Sensors and Actuators*, A 141:43–51, 2008.

[95] M. Kimber, R. Lonergan, and S. V. Garimella. Experimental study of aerodynamic damping in arrays of vibrating cantilevers. *J. Fluid Struct.*, 25:1334–1347, 2009.

[96] V Thakar, Q Pan, F Ayazi, and M Rais-Zadeh. Acoustically coupled thickness-mode AlN-on-Si bandpass filters, part ii: simulation and analysis. *IEEE Trans. Ultrasonics, Ferroelectrics and Frequency Control*, 59(10):2270–2277, 2012.

[97] G. Piazza, V. Felmetsger, P. Muralt, R. Olsson, and R. Ruby. Piezoelectric aluminum nitride thin films for microelectromechanical systems. *Mater. Res. Bull.*, 37:1051–1061, 2012.

[98] V. V. Felmetsger, P.N. Leptev, and S.M. Tanner. Innovative technique for tailoring intrinsic stress in reactive ly sputtered piezoelectric aluminum nitride films. *Journal of Vacuum Science & Technology, A*, 27(3):417–422, 2009.

[99] F. Martin, P. Muralt, and M. A. Dubois. Process optimization for the sputter deposition of molybdenum thin films as electrode for AlN thin films. *J. Vac. Sci. Technol A*, 24:946–952, 2006.

[100] A. Sanz-Hervas, M. Clement, E. Iborra, L. Vergara, and J. Olivares. Degredation of the piezoelectric response of sputtere c-axis AlN thin films with traces of non-(0002) x-ray diffraction peaks. *Appl. Phys. Let.*, 88:161915, 2006.

[101] A Artieda, C Sandu, and P Muralt. Highly piezoelectric AlN thin films grown on amorphous, insulating substrates. *J. Va. Sci. Technol A*, 28(3):390–393, 2010.

[102] E Iborra, M Clement, J Sangrador, A Sanz-Hervas, AJ Navarro, and M Aguilar. Role of argon ion bombardment in sputtered AlN films for SAW devices. *IEEE Ultrasonics Symposium*, pages 411–414, 2002.

[103] G. F. Iriarte, J. Rodriguez, and F. Calle. Synthesis of c-axis oriented AlN thin films on different substrates: A review. *Mater. Res. Bull.*, 45:1039–1045, 2010.

[104] M Clement, E Iborra, J Sangrador, A Sanz-Hervas, and L Vergara. Influence of sputtering mechanisms on the preferred orientation of aluminum nitride thin films. *Jour. Appl. Phys.*, 94(3), 2003.

[105] E Iborra, J Olivares, M Clement, L Vergara, A Sanz-Hervas, and J Sangrador. Piezoelectric properties and residual stress of sputtered aln thin films for mems applications. *Sens. Actuators, A*, 115:501–507, 2004.

[106] G. L. Huffman, D. E. Fahnline, R. Messier, and L.J. Pilione. Stress dependene of reactively sputtered aluminum nitride thin films on sputtering parameters. *J. Vac. Sci. Technol A*, 7:2252–2255, 1989.

[107] H Loebl, M Klee, C Metzmacher, W Brand, R Milsom, and P Lok. Piezoelectric thin AlN films for bulk acoustic wave (BAW) resonators. *Materials Chemistry and Physics*, 79:143–146, 2003.

[108] S Mishin and M Gutkin. Effect of substrate material and surface material and electrode preparation on stress and piezoelectric properties of aluminum nitride. *2011 Joint Conference of the IEEE International Frequency Control and the European Frequency and Time Forum (FCS)*, pages 1–3, 2011.

[109] R. Deng, P. Muralt, and D. Gall. Biaxial texture development in aluminum nitride layers during off-axis sputter deposition. *J. Vac. Sci. Technol. A*, 30:051501, 2012.

[110] A. Artieda, M. Barbieri, C. Sandu, and P. Mural. Effect of substrate roughness on c-oriented aln thin films. *J. Appl. Phys.*, 105:024504, 2009.

[111] F. Martin, P. Muralt, M. A. Dubois, and A. Pezous. Thickness dependence of the properties of highly c-axis textured AlN thin films. *J. Va. Sci. Technol A*, 22:361–365, 2004.

[112] V. V. Felmetsger, P. N. Laptev, and R. J. Graham. Deposition of ultrathin AlN films for high frequency electroacoustic devices. *J. Vac. Sci. Technol. A*, 29:021014, 2011.

[113] S. Mishin, D.R. Marx, B. Sylvia, L. Lughi, K.L. Turner, and D.R. Clarke. Sputtered aln thin films on si and electrodes for mems resonators: Relationship between surface quality microstructure and film properties. In *2003 IEEE Ultrasonics Symposium*, pages 2028–2032, 2003.

[114] H.Windischmann. Intrinsic stress in sputter-deposited thin films. *Crit Rev in Solid State and Mat. Sciences*, 17(6):547–596, 1992.

[115] K. Kusaka, D. Taniguchi, T. Hanabusa, and K. Tominaga. Effect of the input power on crystal orientation and residual stress in aln film deposited by dc sputtering. *Vacuum*, 59:806–813, 2000.

[116] G.F. Iriarte, F. Engelmark, M. Ottosson, and I.V. Katardijiev. Influence of deposition parameters on the stress magnetron sputter-deposited AlN thin films on Si(100) substrates. *J. Mater. Res.*, 18(2):423–432, 2003.

[117] M Moreira, I Doi, J Souza, and J Diniz. Electrical characterization and morphological properties of AlN films prepared by dc reactive magnetron sputtering. *Microelectronic Engineering*, 88:802–806, 2011.

[118] J. A. Thornton. *Semiconductor Materials and Process Technology Handbook*. Noyes, 1988.

[119] J. Thornton. The microstructure of sputterdeposited coatings. *J. Vac. Sci. Technol. A*, 4:3059–3065, 1986.

[120] G Piazza and A Pisano. Two-port stacked piezoelectric aluminum nitride contour-mode resonant mems. *Sensors Actuators A*, 136:638–645, 2007.

[121] R Mahameed, N Sinha, M Pisani, and G Piazza. Dual-beam actuation of piezoelectric aln rf mems switches monolithically integrated with aln contour-mode resonators. *J Micromech. Microeng.*, 18:1–11, 2008.

[122] H. Kroncke, S. Figge, B.M. Epelbaum, and D. Hommel. Determination of the temberature dependent thermal expansion coefficients of bulk aln by hrxrd. *Acta Physica Polonica A*, 114:1193–1200, 2008.

[123] D. Zhuang and J. H. Edgar. Wet etching of GaN, AlN, and SiC: a review. *Mat. Sci. Eng.*, 48:1–46, 2005.

[124] J. R. Mileham, S. J. Pearton, C. R. Abernathy, J. D.Mackenzie, and R. J. Shul. Wet chemical etching of AlN. *App. Phys. Let.*, 67:1119–1121, 1995.

[125] J. M. Miller, D. H. Chi, L. J. OKeeffe, P. Kruszka, Y. Raphael, and R. A. Altschuler. Neurotropins can enhance spiral ganglion cell survival after inner hair cell loss. *Int. J. Devl. Neuroscience*, 15(4/5):631–643, 1997.

[126] L. Waaijer, S. F. L. Klis, D. Ramekers, M. H. W. V. Deurzen, F. G. J. Hendriksen, and W. Grolman. The peripheral processes of spiral ganglion cells after intracochlear application of brain-derived neurotrophic factor in deafened guinea pigs. *Otol Neurotol*, 00:1–9, 2013.

[127] ES Olson. Intracochlear pressure measurements related to cochlear tuning. *J. Acoust. Soc. Am*, 110(1):349–367, 2001.

[128] A Dancer and R Franke. Intracochlear sound pressure measurements in guinea pigs. *Hearing Research*, 2:191–205, 1980.

[129] S. Hatsushika, R. Shepherd, G. Clark, Y. Tong, and S. Funasaka. Dimensions of the scala tympani in the human and cat with reference to cochlear implants. *Ann Otol Rhinol Laryngol*, 99(11):871–875, 1990.